Physical Layer Techniques for 5G:

Waveform Design and Millimeter Waves

A Thesis

submitted for the degree of

Doctor of Philosophy

by

Raviteja Patchava

Department of Electrical and Computer Systems Engineering

Monash University

Australia

March 2019

Copyright Notice

Abstract

In order to achieve the desired goals of the fifth generation (5G) wireless systems, exploring new efficient physical layer techniques is necessary. Waveform design, millimeter waves (mm-Wave), massive MIMO beamforming, and multiple access techniques are some of the areas that are being investigated in 5G. In this thesis, we work in two areas, namely, *waveform design* and *millimeter waves*.

In the first part, we study a recently proposed waveform design called orthogonal time frequency space (OTFS) modulation. OTFS is shown to exhibit significant advantages over currently deployed orthogonal frequency division multiplexing (OFDM) modulation in multipath delay–Doppler channels. The delay–Doppler domain provides as an alternative representation of a time-varying channel geometry due to moving objects (e.g. transmitters, receivers, or reflectors) in the scene. Leveraging on this representation, OTFS multiplexes each information symbol over a two dimensional orthogonal basis functions, specifically designed to combat the dynamics of time-varying multipath channels. Our contributions on OTFS in this thesis are three-fold. We first derive the explicit input–output relations describing OTFS modulation and demodulation (mod/demod) for the cases of (*i*) ideal pulse-shaping waveforms that satisfy the bi-orthogonality conditions, and (*ii*) rectangular waveforms which do not. We show that while only *inter-Doppler interference* is present in the first case, additional *inter-carrier interference (ICI)* and *inter-symbol interference (ISI)* occur in the second case. We next analyze these interference and develop a novel low-complexity yet efficient message passing (MP) algorithm for joint interference cancellation and symbol detection. Our results indicate that OTFS using practical rectangular waveforms can achieve the performance of OTFS using ideal but *non-realizable* pulse-shaping waveforms. We also derive the input—output relation in OTFS for any arbitrary waveforms using a simple matrix notations. Simulation results demonstrate the superior

error performance gains of the proposed *uncoded* OTFS schemes over OFDM under various channel conditions. Further, we compare the OTFS performance with different pulse-shaping waveforms, and show that the reduction of out-of-band power may introduce nonuniform channel gains for the transmitted symbols, thus impairing the overall error performance.

We then consider the channel estimation problem of OTFS and propose an embedded pilot-aided channel estimation scheme for OTFS. In each OTFS frame, we arrange pilot, guard, and data symbols in the delay–Doppler plane to suitably avoid interference between pilot and data symbols at the receiver. At the receiver, channel estimation is performed based on a threshold method and the estimated channel information is used for data detection via MP algorithm. Owing to our specific embedded symbol arrangements, both channel estimation and data detection are performed within the same OTFS frame with a minimum overhead. We compare by simulations the error performance of OTFS using the proposed channel estimation and OTFS with ideally known channel information and observe only a marginal performance loss.

We finally study the system structure of OTFS in static multipath channels. We show that the OTFS structure is equivalent to the asymmetric orthogonal frequency division multiplexing (A-OFDM) [46], bridging between cyclic prefix single carrier (CPSC) and traditional OFDM. We derive a condition on the parameters of OTFS to guarantee that all the transmitted symbols experience uniform channel gains, as in CPSC. Through simulation results, we show that OTFS with MP detection achieves a significant performance improvement over ZF and MMSE detection originally proposed for A-OFDM.

The second part of this thesis focuses on mm-Wave systems. The availability of large bandwidth at mm-Wave frequencies offers a promising solution to support the increasing data traffic demand of 5G. Transmit and receive beamforming through a large number of antennas is a necessary technology to combat the severe path loss encountered at mm-Wave frequencies. Beamforming can be realized cost-effectively by inserting low resolution discrete phase shifters in the RF chain of each antenna. Higher resolution phase shifters would require very high precision RF components, which may be difficult to realize. The main aim of this research is to design good beamforming weight vectors, controlling the low resolution phase shifters, to achieve the performance of fully digital beamforming systems. We first consider the channel estimation problem in point-to-point mm-Wave analog beamforming system. We propose a local search method that enables generation of a quasi-optimal

weight vectors for uniform linear array. We show that the proposed local search design with low resolution phase shifters has improved performance when compared to the existing schemes with high resolution phase shifters.

Finally, we consider mm-Wave multiuser uplink system with low resolution phase shifters. We propose joint and separate designs of precoder and detector that achieves a better performance and complexity tradeoff with fully digital systems. Through simulations, we show that our precoder and detector designs with low resolution phase shifters outperform the traditional methods using steering vectors as beamforming vectors with high resolution phase shifters.

Declaration

I hereby declare that this thesis contains no material which has been accepted for the award of any other degree or diploma in any university or equivalent institution, and that, to the best of my knowledge and belief, this thesis contains no material previously published or written by another person, except where due reference is made in the text of the thesis.

Raviteja Patchava

07-March-2019

Publications During Enrolment

Journals

1. P. Raviteja, K. T. Phan, Y. Hong, and E. Viterbo, "Interference cancellation and iterative detection for orthogonal time frequency space modulation," *IEEE Trans. Wireless Commun.*, vol. 17, no. 10, pp. 6501-6515, Oct. 2018.

2. P. Raviteja, Y. Hong, E. Viterbo, and E. Biglieri, "Practical pulse-shaping waveforms for reduced-cyclic-prefix OTFS," *IEEE Trans. Veh. Technol.*, vol. 68, no. 1, pp. 957-961, Jan. 2019.

3. P. Raviteja, Y. Hong, and E. Viterbo, "Millimeter wave hybrid beamforming with low resolution phase shifters for multiuser uplink," *IEEE Trans. Veh. Technol.*, vol. 67, no. 4, pp. 3205-3215, April 2018.

4. P. Raviteja, Y. Hong, and E. Viterbo, "Analog beamforming with low resolution phase shifters," *IEEE Wireless Commun. Lett.*, vol. 6, no. 4, pp. 502-505, Aug. 2017.

5. P. Raviteja, Y. Hong, and E. Viterbo, "Spatial modulation in full-duplex relaying," *IEEE Commun. Lett.,* vol. 20, no. 10, pp. 2111-2114, Oct. 2016.

6. P. Raviteja, Y. Hong, and E. Viterbo, "OTFS performance on static multipath channels," *IEEE Wireless Commun. Lett.*, Jan. 2019, doi: 10.1109/LWC.2018.2890643.

7. P. Raviteja, K. T. Phan, and Y. Hong, "Embedded pilot-aided channel estimation for OTFS in delay-Doppler channels," submitted for publication in *IEEE Trans. Veh. Technol.* [first review completed].

Conferences

1. P. Raviteja, K. T. Phan, Y. Hong, and E. Viterbo, "Embedded delay-Doppler channel estimation for orthogonal time frequency space modulation," in *Proc. IEEE 88th Vehicular Technology Conference: VTC2018-Fall*, Chicago, USA, August 2018.

2. P. Raviteja and U. Madhow, "Spatially oversampled demultiplexing in mmWave LoS MIMO", in *Proc. IEEE International Workshop on Signal Processing Advances in Wireless Communications (SPAWC 2018),* Kalamata, Greece, June 2018. [**Best Student Paper Award**]

3. P. Raviteja, K. T. Phan, Q. Jin, Y. Hong, and E. Viterbo, "Low-complexity iterative detection for orthogonal time frequency space modulation," in *Proc. IEEE Wireless Communications and Networking Conference (WCNC),* Barcelona, April 2018.

Acknowledgments

Contents

Abbreviations

4G   Fourth generation

5G   Fifth generation

A-OFDM   Asymmetric orthogonal frequency division multiplexing

AD   Analog to digital

AMLD   Approximate ML detector

AoA   Angle-of-arrival

AoD   Angle-of-departure

BER   Bit error rate

BMW-SS   Beam widening via single RF sub-array

BS   Base station

CFO   Carrier frequency offset

CP   Cyclic prefix

CPSC   Cyclic prefix single carrier

CSI   Channel state information

DA   Digital to analog

DEACT   Deactivation

DTFT	Discrete time Fourier transform
EVA	Extended Vehicular A model
FFT	Fast Fourier transform
HPC	Hybrid precoder and combiner
IC	Interference cancellation
ICI	Inter carrier interference
ICI	Inter symbol interference
IDI	Inter Doppler interference
IFFT	Inverse fast Fourier transform
ISFFT	Inverse symplectic fast Fourier transform
LoS	Line of sight
LSA	Local search algorithm
LTE	Long term evolution
MF	Matched filter
MIMO	Multiple-input multiple-output
ML	Maximum likelihood
mm-Wave	Millimeter waves
MMSE	Minimum mean square estimation
MP	Message passing
NLoS	Non line of sight
OFDM	Orthogonal frequency division multiplexing
OMP	Orthogonal matching pursuit

OTFS	Orthogonal time frequency space
PAPR	Peak-to-average power ratio
PS-OFDM	Pulse-shaped OFDM
PSW	Prolate spheroidal waveform
RF	Radio frequency
SC	single carrier
SCD	Successive cancellation detector
SCD	Successive cancellation detector
SEP	Successive estimation precoder
SFFT	Symplectic fast Fourier transform
SINR	Signal to interference plus noise ratio
SISO	Single-input single-output
SNR	Signal to noise ratio
SVD	Singular value decomposition
ULA	Uniform linear array
ZF	Zero forcing

Notations

a	Scalar
$\mathbf{a}$	Vector
$\mathbf{A}$	Matrix
$a(n)$	n^{th} element of $\mathbf{a}$
$\mathbf{A}(m,n)$	$(m,n)^{th}$ element of $\mathbf{A}$
$\mathbf{A}^{\mathrm{T}}$	Transpose of $\mathbf{A}$
$\mathbf{A}^{\mathrm{H}}$	Hermitian transpose of $\mathbf{A}$
$\mathbf{A}^{-1}$	Inverse of $\mathbf{A}$
$\mathbf{A}^{n}$	n^{th} power of $\mathbf{A}$
$[i]_M$	Mod M operation on integer i
$|a|$	Magnitude of a
$|\mathbf{a}|$	Element-wise absolute value of $\mathbf{a}$
$\|\mathbf{a}\|$	Euclidean norm of $\mathbf{a}$
$\|\mathbf{A}\|_2$	Spectral norm of $\mathbf{A}$
$\det[\mathbf{A}]$	Determinant of $\mathbf{A}$
$\langle \mathbf{a}, \mathbf{b} \rangle$	Dot product between $\mathbf{a}$ and $\mathbf{b}$
$\|\mathbf{a}\|_0$	Number of non-zero elements in $\mathbf{a}$

$\mathbb{C}^{M \times N}$	Set of $M \times N$ dimensional matrices with each entry from the complex plane
$\otimes$	Kronecker product
$\text{diag}[\mathbf{A}_0, \cdots, \mathbf{A}_{N-1}]$	Block diagonal matrix with $\{\mathbf{A}_0, \cdots, \mathbf{A}_{N-1}\}$ as diagonal blocks
$\mathbf{F}_n$	n-point FFT matrix
$\mathbf{F}_n^{\text{H}}$	n-point IFFT matrix
$\mathbf{I}_M$	M-dimensional identity matrix
$\mathcal{CN}(0, \sigma^2)$	Circularly symmetric Gaussian distribution with 0 mean and σ^2 variance.

List of Figures

Chapter 1

Introduction

The fifth generation (5G) wireless systems are expected to support billions of devices with 1000x higher data traffic than today's communication systems (4G) [1]. Besides the increased data rates, 5G systems are also supposed to offer better coverage, ultra reliable communications at high velocity links, low latency, and improved energy efficiency [2, 3]. Some of the future applications may include real-time video streaming, remote health care, online gaming, and connected and autonomous vehicles [4, 5].

The fundamental directions that researchers are endeavouring towards 5G goals can be broadly categorized into two areas: development of new efficient physical layer techniques and deployment of more active nodes (e.g., routers) in a given area [6–12]. Physical layer techniques primarily include spectrum shift towards millimeter waves, utilizing massive multiple-input multiple-output (MIMO) beamforming to support multiple parallel users, and new waveform designs that can provide better channel gains thus reliable wireless links. Whereas dense deployment includes cell shrinking, co-operation between different wireless systems such as WiFi, long term evolution (LTE) unlicensed, device-to-device communications, and cognitive radio. This thesis focuses on the first aspect, efficient physical layer techniques. In particular, we investigate two physical layer techniques, namely, waveform design and millimeter waves, which can address the ultra reliable communication and high data traffic problems of 5G respectively.

Waveform design defines the packing of information symbols in the given time and frequency resources and forms the basic building block of the communication system [27, 28]. While the currently deployed orthogonal frequency division multiplexing (OFDM) modulation in 4G LTE

$$X[m] \rightarrow \boxed{\text{IFFT}} \xrightarrow{s(t)} \boxed{\text{Channel}} \xrightarrow{r(t)} \boxed{\text{FFT}} \xrightarrow{Y[m]}$$

Figure 1.1: OFDM system model

mobile systems can achieve better spectral efficiency, it is not robust to time-varying channels with high Doppler spread (e.g., high-speed railway mobile communications) [29]. A new modulation technique called orthogonal time frequency space (OTFS) modulation was recently proposed in [17], showing significant advantages over OFDM in time-varying channels.

On the other hand, millimeter waves (mm-Wave) offer a wide range of spectrum frequencies which could be able to solve the huge data demands of the future wireless systems [11]. One major issue of mm-Wave communications is the extremely high path loss. This can be typically overcome by implementing transmit and receive beamforming through multiple antennas.

In the next part of this chapter, we run through the basics of OTFS modulation and beamforming in millimeter waves followed by our detailed contributions in these areas.

1.1   OTFS Modulation

Prior to the introduction of OTFS modulation, we provide below a brief overview of OFDM modulation.

1.1.1   Overview of OFDM System

The main idea of OFDM is to place the information symbols in the frequency grid which are later converted to the time domain for transmission using Fourier transform. Fig. 1.1 shows the basic OFDM system model, where the inverse fast Fourier transform (IFFT) is applied at the transmitter and the fast Fourier transform (FFT) is applied at the receiver, to convert from frequency to time domain and vice-versa. Through the Fourier operations, OFDM converts the time-invariant frequency selective channel into multiple parallel frequency flat sub-channels which are known as *subcarriers*. Fig. 1.2 explains the orthogonality across the subcarriers in OFDM, where the main lobe peak of each subcarrier experiences zero interference from all other subcarriers.

Because of the orthogonality of the subcarriers, OFDM signal can be detected by a simple one
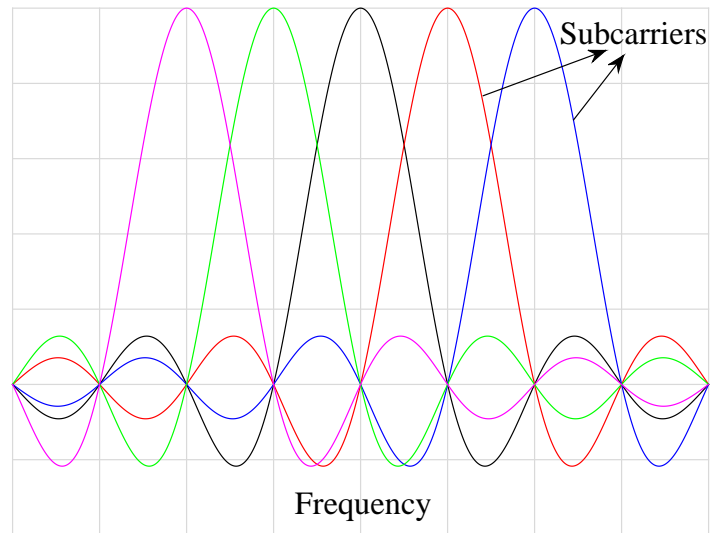
Figure 1.2: Subcarriers in OFDM
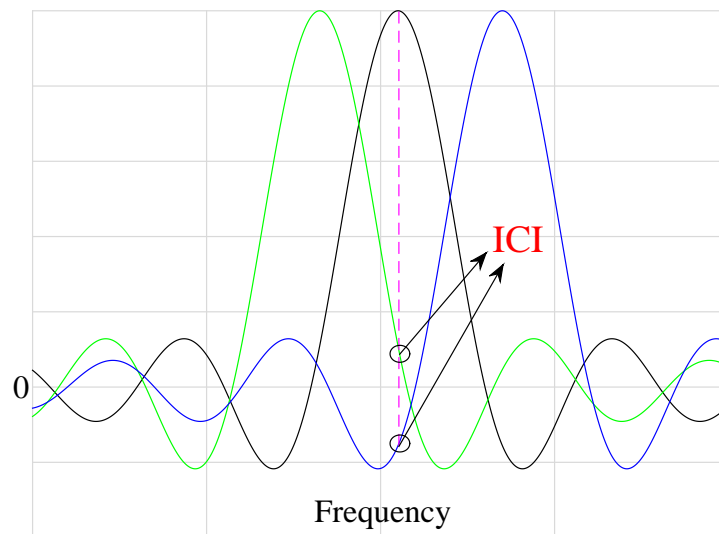
Figure 1.3: ICI across subcarriers in OFDM

tap equalizer. OFDM is also known to achieve high spectral efficiency for time-invariant frequency selective channels as it supports the optimal spacing of the subcarriers.

However, the frequency channel gains across the OFDM subcarriers are not equal and the lowest gain subcarrier decides the overall system performance. Moreover, the one tap equalization of OFDM results in a diversity order of one. Further, for high-mobility environments such as high-speed railway mobile communications, the channels can be typically time-varying with high Doppler spreads. Under such high Doppler conditions, subcarriers in OFDM experience inter carrier interference (ICI) as shown in Fig. 1.3 and OFDM is no longer robust and suffers heavy performance degradations. The effect of ICI becomes even more severe for the channels with multiple Dopplers. To cope with time-varying channels, one existing approach is to shorten the OFDM symbol duration so that the channel variations over each symbol appear inconsequential [13]. However, one major drawback is the reduced spectral efficiency due to cyclic prefix (CP).

Several modifications on OFDM were proposed in the literature to address the low diversity and high ICI sensitivity issues. We broadly classified these approaches into: *i*) design of efficient waveforms that perform close to the ideal bi-orthogonal property in time and frequency dimensions [14,15,29,31,38], and *ii*) precoding techniques over OFDM [49–52]. The first approach tries to apply a near-optimal bi-orthogonal waveform to a series of OFDM symbols across time before transmission. This waveform technique is popularly known as pulse-shaped OFDM (PS-OFDM) [39]. The bi-orthogonality property of the waveform helps in minimizing the interference that occurs between the subcarriers in both frequency and time dimensions, i.e., ICI and inter symbol interference (ISI) respectively. The general block diagram of PS-OFDM is shown in Fig. 1.4, where the *Heisenberg* and *Wigner* transforms can be simplified to IFFT and FFT in a single OFDM case respectively. An example of this technique can be found in [38], where the authors provided a Zak-transform based design to generate near-optimal waveforms. Even though this approach greatly reduces the ICI in low Doppler channels compared to the traditional OFDM, it is not effective for multiple high Doppler channels as the perfect bi-orthogonality is not practically feasible due to Heisenberg's uncertainty principle. Moreover, this approach does not solve the low diversity problem of OFDM.

The second approach applies an efficient precoding matrix on PS-OFDM before transmission. This approach was shown to achieve full diversity from the channel and also efficiently combat the multiple Doppler effects. For example, the authors in [51] proposed a Vandermonde matrix based

Figure 1.4: PS-OFDM system model

(a) Time–frequency channel

(b) Delay–Doppler channel
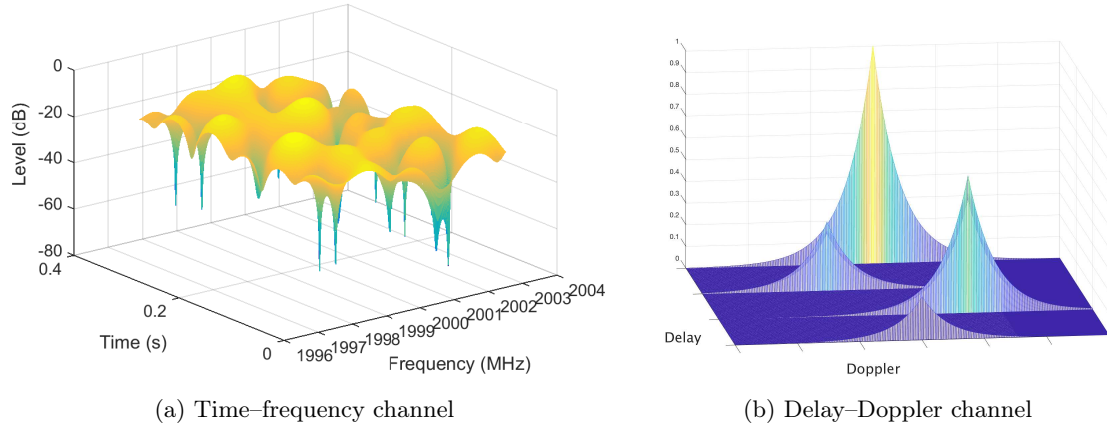
Figure 1.5: Time–frequency and delay–Doppler channels

precoding to achieve full channel diversity. However, unfortunately these methods require a very high complexity receiver. Furthermore, acquiring the full channel state information (CSI) is also complex as the effective channel is non-sparse full entry matrix in most of the cases. Hence, a new modulation scheme that can provide better diversity gains and sensitivity to the high Dopplers as well as simple receiver structure is required.

1.1.2 OTFS System

The key idea of OTFS is to transmit the information symbols in the delay–Doppler plane rather than in the time–frequency plane as with PS-OFDM [17–20]. The delay-Doppler plane captures the delays and Doppler shifts of the physical paths present in the wireless channel, and allows a sparse representation of the channel. Fig. 1.5 shows an examples of the time–frequency ($H(t, f)$) and delay–Doppler ($h(\tau, \nu)$) channels in time-varying multipath scenarios. We can clearly see that while the time–frequency channel is spread throughout the plane, delay–Doppler channel is sparse which eases channel tracking.

Assuming $s(t)$ is the transmitted time domain signal, the received signal, $r(t)$, in the presence

of time-variant multipath channel (also known as doubly dispersive channel) can be written as

$$r(t) = \int_\tau g(t,\tau)s(t-\tau)d\tau \tag{1.1}$$

$$= \int_f H(t,f)S(f)e^{j2\pi ft}df \tag{1.2}$$

$$= \int_\nu \int_\tau h(\tau,\nu)s(t-\tau)e^{j2\pi\nu t}d\tau d\nu \tag{1.3}$$

where $S(f)$ is the Fourier transform of $s(t)$. The three equivalent relations in (1.1)–(1.3) can be interpreted as follows. The channel $g(t,\tau)$ in (1.1) represents the time-varying impulse response and the relation can be seen as a straightforward generalization of the linear time-invariant (LTI) system. The relation in (1.2) describes the time–frequency channel and PS-OFDM system is defined based on this relation. Finally, the relation in (1.3) depicts the sparse delay–Doppler channel and OTFS is defined based on this relation. Now, the relation between the time–frequency ($H(t,f)$) and delay–Doppler ($h(\tau,\nu)$) channels can be given by a pair of two-dimensional symplectic fast Fourier transforms (SFFT) as

$$h(\tau,\nu) = \int \int H(t,f)e^{-j2\pi(\nu t - f\tau)}dtdf \tag{1.4}$$

$$H(t,f) = \int \int h(\tau,\nu)e^{j2\pi(\nu t - f\tau)}d\tau d\nu \tag{1.5}$$

where, (1.4) and (1.5) represent the SFFT and inverse SFFT (ISFFT) operations, respectively. Fig. 1.6 shows the relations between the four equivalent time-variant multipath channels defined in the literature [21, 29], where $\mathcal{F}$ denotes the Fourier operation.

Based on the SFFT relations, OTFS system model is given in Fig. 1.7 [17, 18], where the ISFFT and SFFT are added as the pre and post processing blocks at the transmitter and receiver of PS-OFDM–respectively. In particular, first ISSFT is applied to the information symbols at the transmitter before processing through PS-OFDM modulator and SFFT is applied to the received samples obtained after the PS-OFDM demodulator at the receiver. Since the SFFT operation transforms the time–frequency domain to delay–Doppler domain, the domain where the information symbols and the final received symbols reside is termed as delay–Doppler domain.

In an alternative representation, OTFS can be seen as a Zak-transform [18] applied on the information symbols in delay–Doppler domain, analogous to the Fourier transform in OFDM. In this

time-variant impulse response

$$g(t, \tau)$$

$\mathcal{F}$ $\mathcal{F}$

time-frequency channel (PS-OFDM) $H(t, f)$ SFFT $\rightarrow$ $h(\tau, \nu)$ delay-Doppler channel (OTFS)

$\mathcal{F}$ $\mathcal{F}$

$$B(\nu, f)$$

Doppler-variant transfer response
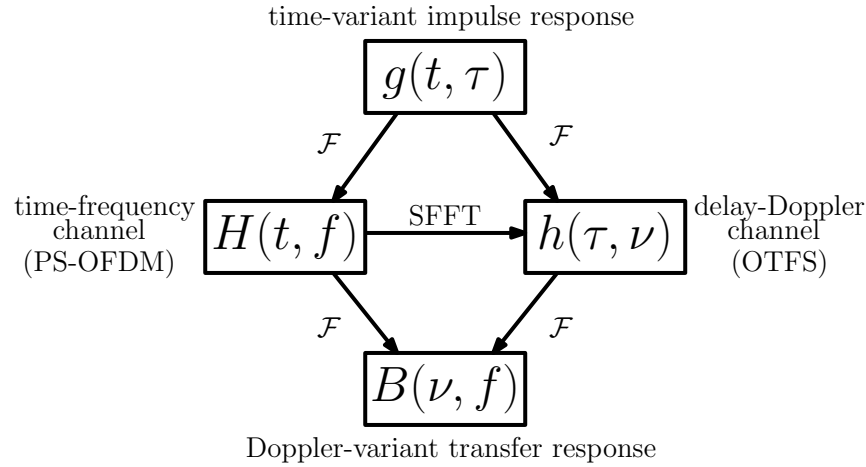
Figure 1.6: Different representations of a time-variant multipath channel
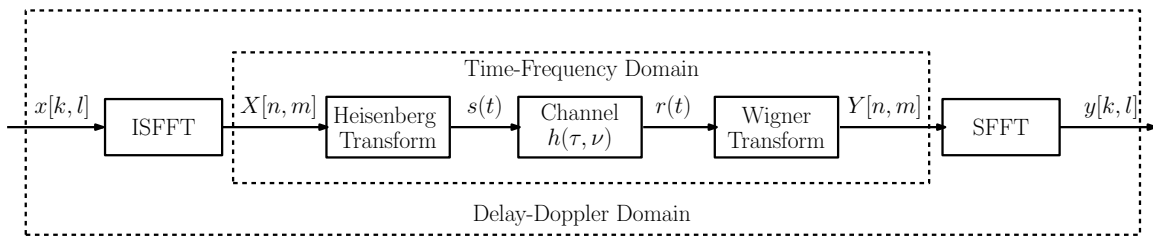
Figure 1.7: OTFS system model

representation, the blocks ISFFT and Heisenberg transform together represents the Zak-transform, which converts the two-dimensional information symbols to time domain transmitted signal. Similarly, the blocks Wigner transform and SFFT together constitutes the inverse Zak-transform, which converts the received time domain signal to two-dimensional received symbols in the delay–Doppler domain.

Due to the delay–Doppler domain operations, the OTFS final output symbol, $y[k, l]$, for ideal bi-

(a) Input symbol   (b) Delay–Doppler channel   (c) Output symbol
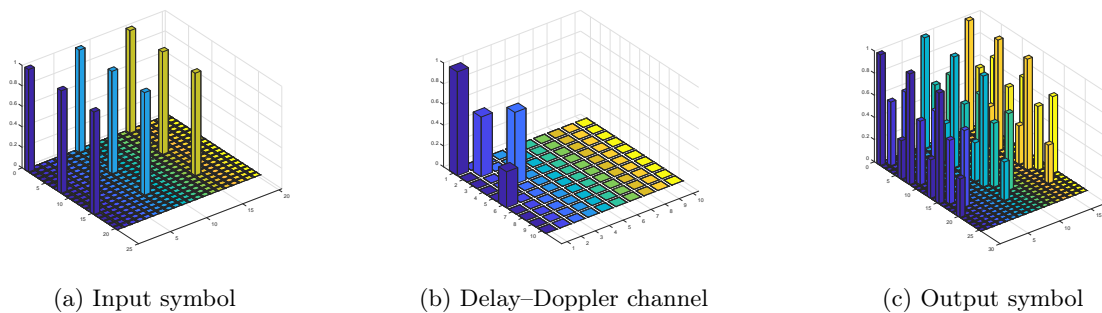
Figure 1.8: Input–output relation in OTFS

orthogonal pulses can be seen as a two-dimensional convolution between the delay–Doppler channel and the input symbol, $x[k, l]$ [19]. Fig. 1.8 depicts the convolutional relation between the input and output symbols in OTFS. As the delay–Doppler channel is sparse and underspread in typical wireless communications [29], we can observe the channel in Fig. 1.8b has few non-zero taps packed within a small area of the entire grid. The convolution relation and the sparse channel structure provide many advantages to OTFS over other waveform designs which are described as below.

1. *Uniform channel gains*: In contrast to the unequal channel gains across subcarriers in OFDM, all the transmitted symbols in OTFS experience the same channel gains, because of the convolution relation.

2. *Channel diversity*: As every information symbol is received through multiple independent channel paths, OTFS may be able to achieve full channel diversity with appropriate precoding. Moreover, through OTFS, we can resolve the paths that differ in at least one of the delay or Doppler values. This property helps in achieving better diversity gains compared to the conventional single carrier (SC) systems, where only distinct delay paths can be resolved.

3. *Low Doppler sensitivity*: Since the delay–Doppler channel can be easily tracked by using a few channel coefficients, even the high Doppler channels can be easily equalized at the receiver. In theory, OTFS is able to correct the Doppler shifts upto the subcarrier spacing, whereas OFDM can correct the Doppler shifts only upto 10% of the subcarrier spacing.

4. *Low detection complexity*: Since every output symbol is dependent only on the few surrounding input symbols, simple low-complexity algorithms such as message passing can be implemented for detection.

Since the seminal paper on OTFS in [17], a number of improvements were proposed in [22–24, 36, 37, 42, 43, 48]. In [23], an efficient implementation for OTFS was presented by simplifying the ISFFT and Heisenberg transforms to one IFFT at the transmitter and SFFT and Wigner transform to one FFT at the receiver. An ergodic capacity analysis for OFDM-based OTFS was conducted in [24]. In [22, 36, 37, 42, 43], several low-complexity detection techniques for OTFS such as decision feedback equalizer, minimum mean square estimation (MMSE) with ISI cancellation, and Markov Chain Monte Carlo algorithms were proposed. In [42, 43], various pilot-aided channel estimation

methods for OTFS were proposed. In [19, 43], extension of OTFS to MIMO and multiuser systems were studied. In [48], a relation between OTFS and generalized frequency division multiplexing (GFDM) was established.

However, all the above work assumes either i) ideal pulse-shaping waveforms that satisfy orthogonality conditions in both time and frequency, which is not practically feasible due to Heisenberg's uncertainty principle, or ii) OFDM-based OTFS system, where non-ideal rectangular pulse-shaping waveforms and CP for every OFDM symbol in OTFS frame are considered, which considerably reduces the overall spectral efficiency. In contrast to these assumptions, in this work, we consider OTFS system with practically realizable waveforms and only one CP for the entire frame. The detailed contributions of our work on OTFS are described in the next section.

1.1.3   Contributions

In this thesis, we study several aspects of OTFS system such as OTFS with practical waveforms, channel estimation for OTFS, and OTFS for static channels. In the following, we summarize our contributions on OTFS modulation.

In Chapter 2, we analyze the input–output relation describing OTFS mod/demod for delay–Doppler channels using rectangular pulse-shaping waveforms. The relation reveals the effects of the ISFFT and SFFT operations interpreted as pre and post processing blocks applied to a time–frequency signaling scheme. We then analyze the cases of (i) ideal pulse-shaping waveforms that satisfy the bi-orthogonality conditions, and (ii) practical rectangular waveforms which do not. Unlike previous works [22], [23], [24], we assume *no* CP in the second case. We then present a simple relation characterizing the interference. Specifically, we show that, while only *inter-Doppler interference* (IDI) is present in the ideal waveform case due to unavoidable fractional Doppler effects, additional *ICI* and *ISI* occur in the rectangular waveform case due to imperfect *bi-orthogonality* in time–frequency domain of the rectangular waveforms. Our analysis of these interferences enables the development of an efficient algorithm for OTFS detection, which is the next contribution of this chapter.

The delay–Doppler channel model with a small number of paths, with varying delay and Doppler values, provides a sparse representation of the communication channel. We then propose a low-complexity yet efficient message passing (MP) algorithm for a joint interference cancellation (IC)

and detection, which takes advantage of the inherent delay–Doppler channel sparsity. The MP algorithm is based on a sparse factor graph and uses Gaussian approximation of the interference terms to further reduce the complexity. The approach is similar to [25], where it was applied to massive MIMO without the advantage of channel sparsity. The complexity and convergence of the MP algorithm are analyzed. In the MP algorithm, while the ICI and ISI can be eliminated by suitable phase shifting, the IDI can be mitigated by adapting the MP algorithm to account for only the largest interference terms. Consequently, the proposed MP algorithm can effectively compensate for a wide range of channel Doppler spreads. Further, our results show that OTFS using practical rectangular waveforms can achieve the performance of OTFS using ideal but non-realizable pulse-shaping waveforms. Simulations results illustrate the superior performance gains of the proposed *uncoded* OTFS schemes over OFDM under various channel conditions. The performance results of uncoded systems demonstrate the performance gains of OTFS over OFDM due to specific OTFS mod/demod architecture (i.e., ISFFT and SFFT operations as pre- and post-processing blocks) and the effect of the proposed MP algorithm.

Inspired by a simple matrix representation of OFDM systems using circulant-matrix decomposition, in Chapter 3, we first express the OTFS effective channel transfer matrix using two matrix decompositions, one for delay and another for Doppler components. Next, we simplify the OTFS effective channel by applying some properties of block circulant matrices, and show that the effective channel transfer matrix has a simple sparse structure, with sparsity depending on the number of paths in the channel. Because of the sparse matrix structure, a low-complexity detection algorithm can be used at the receiver. Moreover, we show how our approach can be easily extended to arbitrary practical pulse-shaping waveforms that are applied to the time domain signal. Further, we compare the OTFS performance of rectangular and prolate spheroidal waveforms, and illustrate a tradeoff between out-of-band radiation and bit error rate (BER) performance.

In Chapter 4, we propose an embedded OTFS channel estimation scheme for point-to-point single-input single-output (SISO) system with ideal and rectangular pulse-shaping waveforms, respectively. Specifically, for each OTFS frame, we arrange a single pilot symbol, guard symbols, and data symbols in the delay–Doppler grid to suitably avoid the interference between pilot and data symbols. At the receiver, channel estimation is performed based on a threshold method and the estimated channel information is used for data detection via a MP algorithm proposed in Chapter

2. Depending on the channel and symbol arrangement, the threshold is chosen to optimize the estimation accuracy. Owing to our specific embedded symbol arrangements, both channel estimation and data detection are performed within the same OTFS frame with a minimum overhead (1% for integer Doppler case and 8% for fractional Doppler case).

We compare by simulations the performance of OTFS using the proposed channel estimation schemes and OTFS with perfectly known channel information and observe only a marginal performance degradation. Further, we show that OTFS with our channel estimation significantly outperforms OFDM, with ideal channel information.

In Chapter 5, we study OTFS over static multipath channels and reveal that the system structure of OTFS is equivalent to the asymmetric orthogonal frequency division multiplexing (A-OFDM), a scheme proposed in [46] that generalizes OFDM and cyclic prefix single carrier (CPSC) by exploiting a layered FFT structure. Next, we derive a necessary and sufficient condition on the number of subcarriers in OTFS to guarantee that all the transmitted symbols experience uniform channel gains, as in CPSC (a special case of OTFS/A-OFDM). We also show that OTFS offers a tradeoff between spectral efficiency and maximum peak-to-average power ratio (PAPR), for a given performance target and detection complexity. Finally, we apply a MP algorithm to OTFS/A-OFDM and show that it outperforms OFDM as well as A-OFDM with zero forcing (ZF) and MMSE detectors in [46, 47].

1.2 Millimeter Wave Communications

Mm-Wave communications focus on operating at the 10-100GHz frequency ranges where the massive amounts of bandwidth is available. In particular, while the overall spectrum available in today's communication systems is less than 1 GHz, mm-Wave below 100 GHz offers more than 20 GHz spectrum and hundreds of GHz spectrum could be made available at frequencies higher than 100 GHz [11, 53]. However, the high propagation loss in these frequency ranges is the main challenge for operating at mm-Wave. Owing to the higher frequencies, the wavelengths are in the millimeter range, hence more antennas can be packed in a small area-compared to the microwave frequencies. Transmit and receive beamforming through a large number of antennas is the preferred solution to combat path loss [11, 53–62].

In general, beamforming is obtained by applying different weights to the signals at each transmitting or receiving antenna. In *digital beamforming*, this process is performed in the digital domain and both amplitude and phase can be easily adjusted to obtain an optimal beam. This requires a number of transmit or receive RF chains (including AD/DA converters up/down converters and power amplifiers) equal to the number of antennas. Apart from the additional cost of the hardware replicated for each antenna, the large number of AD/DA converters operating at high rates consumes a large amount of power.

To overcome this problem, *analog beamforming* was proposed [63–65,67,68,70]. In analog beamforming, only one RF chain is used for all the antennas in the array and the weights only modify the phases by operating on the analog domain signals. Phase shifters [75,79,80] are used to change the phase of incoming signal. In general these phase shifters can only realize a small number of distinct phase shifts (e.g., 4-16). Higher number of phase shifts would require very high precision components, which may be difficult to realize. In general, optimum beamforming weight vectors need to be quantized to such discrete phase shifts resulting in degraded performance. As a compromise between digital and analog, *hybrid beamforming* was proposed in the literature [66,71,78,85]. A limited number of RF chains (e.g., 3-4) are used to transmit different streams in different beams. Two different architectures for hybrid beamforming are possible: *(i)* the antennas with the respective phase shifter are grouped and each RF chain is allocated to one group (sub-connected structure); *(ii)* all antennas are connected to all RF chains through different phase shifters (fully connected structure).

Figs. 1.9, 1.10, and 1.11 show the implementation of analog, digital, and hybrid (fully connected K RF chains) beamforming systems at an N antenna node, respectively.
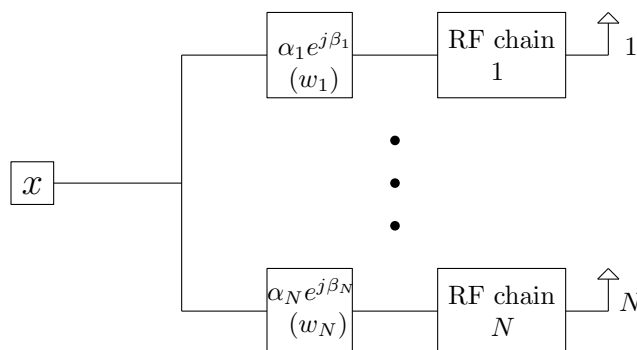
Figure 1.9: Digital beamforming system
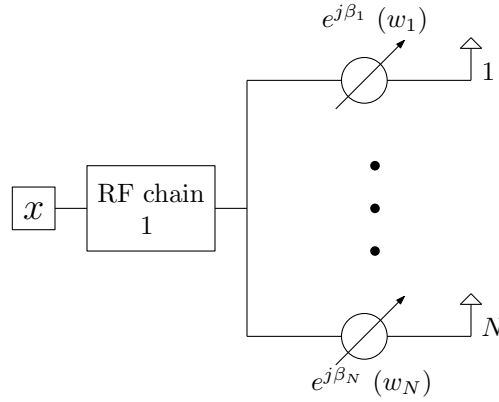
Figure 1.10: Analog beamforming system
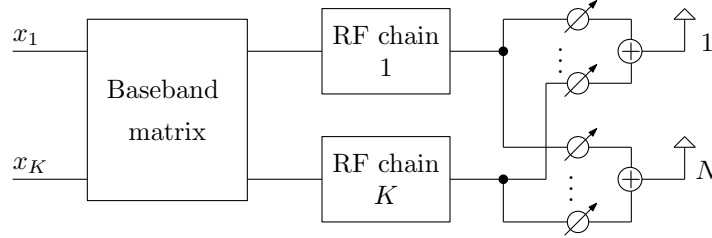
Figure 1.11: Fully connected hybrid beamforming system

In all the beamforming structures, finding the best beamforming weights requires full channel state information at both transmitter and receiver. The channel estimation problem in mm-Wave is challenged by the fact that pilot signals need to be beamformed to receiver to overcome the stark path loss of omni-directional transmission [63, 73, 74]. Fortunately, mm-Wave channels have very small number of paths due to high absorption. Owing to this sparsity, channel estimation is equivalent to finding the steering angles and path-loss coefficients for each of the different paths. In the special case of uniform linear array (ULA) antenna structure at transmitter and receiver, the channel is fully described by the angle-of-departure (AoD) and angle-of-arrival (AoA) of each path. For example, Fig. 1.12 shows the ULA antenna structure with $\lambda/2$ spacing at the receiver. The channel response vector at the receiver for N-antenna ULA antenna structure with $\lambda/2$ spacing can be written as

$$\mathbf{a}(\theta, N) \triangleq [1, e^{j2\pi f \frac{\lambda \cos(\theta)}{2c}}, \ldots, e^{j2\pi f \frac{\lambda(N-1)\cos(\theta)}{2c}}]^T$$
$$= [1, e^{j\pi \cos(\theta)}, \ldots, e^{j\pi(N-1)\cos(\theta)}]^T$$
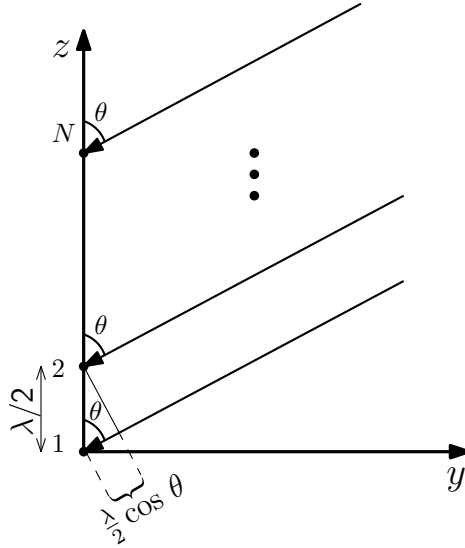
Figure 1.12: ULA antenna structure at the receiver

where f is the operating frequency, λ is the wavelength, c is the velocity of light, and θ is AoA.

In this thesis, we consider the problems of finding the best beamforming weight vectors for the analog and hybrid beamforming structures as mentioned below.

1.2.1 Analog Beamforming Structure

In analog beamforming structure, the optimal beamform weights for a given channel is equivalent to beamforming along the strongest path of the channel. In [72, 73], a simple method was proposed to find the beamform vectors corresponding to the strongest path: transmitter and receiver scan all possible beamforming vectors from a *codebook* and select the best beamform vector pair, which yields the maximum received power. Even though this method is effective to find the best weights, it requires a long training time to test all beamforming vector pairs. To overcome this problem, a hierarchical beam search was proposed in [63, 67, 69, 70], where the authors divided the search into several levels, with each level having an increasingly narrower beam-width. The final stage corresponds to the highest angular resolution achievable by the antenna array. Table 1.1 shows the hierarchical codebook structure with m levels, where $M = 2^m$ denote the total number of angular positions to be scanned and $\mathbf{w}(0, 1)$ in level 0 is the omni-directional mode.

In [71], a hierarchical beam search for hybrid beamforming was proposed based on an orthogonal matching pursuit (OMP) algorithm, and this was extended to a beam search for multiple paths to

Table 1.1: The hierarchical codebook structure

0	$\mathbf{w}(0,1)$						
1	$\mathbf{w}(1,1)$				$\mathbf{w}(1,2)$		
2	$\mathbf{w}(2,1)$		$\mathbf{w}(2,2)$		$\mathbf{w}(2,3)$		$\mathbf{w}(2,4)$
3	$\mathbf{w}(3,1)$	$\mathbf{w}(3,2)$	$\mathbf{w}(3,3)$	$\mathbf{w}(3,4)$	$\mathbf{w}(3,5)$	$\mathbf{w}(3,6)$	$\mathbf{w}(3,7)$	$\mathbf{w}(3,8)$
$\vdots$	$\vdots$						
$m = \log_2(M)$	$\mathbf{w}(m,1)$			$\cdots$			$\mathbf{w}(m,M)$

support multi-stream transmission. The performance of hierarchical search completely depends on the resolution of the beamforming vectors in the codebook used at different levels. In [63], a three-level hierarchical codebook was proposed, which has a limited beamforming gain since the antenna array gain is not fully exploited. In [67], a hierarchical codebook was proposed, where the weights of the beamform vectors in the initial levels were adapted in both amplitude and phase. However, realizing the amplitude changes is an additional challenge to the implementation of analog phase shifters. In [71], high quality beams were generated by using large number of RF chains, which significantly increases the system cost. To reduce it, in [69], a hierarchical codebook was designed based on deactivation of some of the antennas in the array.

Further, in [70], a complete binary-tree structured hierarchical codebook design was proposed by jointly using beam widening via single RF sub-array (BMW-SS) and deactivation techniques (DEACT). These showed a performance improvement over the schemes in [69, 71]. However, all these codebook designs are based on the assumption of high resolution phase shifters (7, 8 bits) or switching off some of the antennas. The use of high resolution phase shifters increases the device cost and switching off some antennas increases the power load on other antennas.

1.2.2   Hybrid Beamforming Structure

Analog beamforming in its basic form supports only one RF stream in a point-to-point communication system and uses only one RF chain at the transmitter and receiver. In contrast, the hybrid beamforming structure [71, 78, 85] allows us to support multiple streams and multiuser communication.

For hybrid beamforming, designing multiple beamforming vectors requires the knowledge of

multiple propagation paths in the RF channel, in contrast to analog beamforming which requires only the knowledge of the strongest path. Typically, at mm-Wave frequencies, a few dominant paths are sufficient to construct an accurate channel matrix model due to the sparsity of propagation paths. An efficient hierarchical codebook design for channel estimation in hybrid beamforming system was proposed using generalized detection probability in [77]. In [86], the transmit and receive beamforming vectors were designed by decomposing the non-convex matrix decomposition problem into a series of convex sub-problems. The authors in [87] proposed a design of transmit and receive beamforming vectors for a finite alphabet rather than Gaussian input alphabet using an iterative gradient ascent algorithm.

On the other hand, several works have focused on the mm-Wave multiuser downlink system [90, 92–94]. For example, in [90], the authors proposed a beam selection method using compressed sensing with low-cost analog beamformers. In [93], the authors proposed a two-stage multi user hybrid beamforming algorithm, where the first stage implemented an analog only beamforming design and second stage implemented a digital only beamforming disign.

In contrast, much less work has focused on the design of beamforming vectors, in particular, transmit beamforming vectors, for mm-Wave multiuser uplink systems, where multiple users transmit simultaneously to the base station (BS). In [95], receive beamforming vectors were designed based on successive cancellation for low complexity detection at the BS. In [96], a detector that designs receive beamforming vectors at the BS using a low complexity Gram-Schmidt method was proposed. Note that, in [95, 96], only receive beamforming vectors were designed, and high resolution phase shifters were required to guarantee good performance. Recently, the authors of [98] have proposed an iterative algorithm for the design of transmit and receive beamforming vectors, assuming high resolution phase shifters and only the structure of $\mathbf{a}(\theta, N)$ for transmit and receive beamforming vectors.

1.2.3   Contributions

In this thesis, we study the design of best beamforming weight vectors using practically feasible low resolution phase shifters for analog beamforming in the case of point-to-point system and the hybrid beamforming structure for the multiuser uplink system. In the following, we summarize our contributions on mm-Wave communications.

In Chapter 6, we consider channel estimation problem in point-to-point analog beamforming system and propose a hierarchical codebook design for channel estimation in analog beamforming with low resolution phase shifters. The beamforming vectors in our codebook are grouped into multiple levels. At each level, the preferred beamforming vector is constructed to approach the corresponding amplitude beamforming gain mask using a low complexity local search algorithm. Through simulations, we show that our codebooks with low resolution phase shifters outperform an existing scheme with high resolution phase shifters. Our design method can also be extended to a variety of antenna arrangements, such as uniform planar arrays.

In Chapter 7, we design transmit and receive beamforming vectors for multiuser uplink system using low resolution phase shifters only, each with q phase shifts ($q = 4, 8, 16$). We assume CSI is available at both the users and the BS, i.e., the BS feedbacks the transmit beamforming vector information to the users. The contributions on the multiuser uplink system are summarized below.

1. We propose a joint precoder and detector design based on the low-complexity local search algorithm for the system using low resolution phase shifters ($q = 4, 8, 16$), where both transmit and receive beamforming vectors are iteratively determined to maximize the sum-rate of the uplink system. We show by simulations that the joint design achieves similar sum-rate to the fully digital system, and better error performance than the existing scheme with high resolution phase shifters ($q = 128$) [98].

2. Although the joint design achieves excellent performance, the computation complexity of searching good beamforming vectors is high. We then propose separate designs of precoder and detector that provide good complexity-and-performance tradeoffs. In precoder designs, the transmit beamforming vectors are selected to maximize either the signal to noise ratio (SNR) or the signal to interference plus noise ratio (SINR) of each user. In detector designs, the receive beamforming vectors are chosen by using either an approximate maximum likelihood detector or a successive cancellation detector.

3. Through simulations, we show that our designs with low resolution phase shifters outperform the traditional methods which uses the steering vectors as beamforming vectors with high resolution phase shifters [95, 96].

1.3   Organization

The rest of the thesis is organized as follows. Chapters 2, 3, and 4 correspond to OTFS modulation and constitutes Part 1 of the thesis. Chapters 6 and 7 correspond to millimeter wave communication and constitutes Part 2 of the thesis.

In Chapter 2, we derive the input–output relation in OTFS for practical rectangular waveforms. Chapter 3 presents the OTFS input–output relation for arbitrary waveforms using simple matrix notations. In Chapter 4, we propose an embedded pilot based channel detection algorithm for OTFS. Chapter 5 studies the OTFS system for static multipath channels. In Chapter 6, we present the local search based analog beamforming algorithm for channel estimation in point-to-point mm-Wave system. Chapter 7 presents the joint and individual precoder and detector designs for mm-Wave multiuser uplink system. Finally, in Chapter 8, we summarize the contributions and discuss some possible future directions.

Part 1: Orthogonal Time Frequency Space (OTFS) Modulation

Chapter 2

OTFS With Practical Rectangular Waveforms

In this chapter, we elaborate on the recently proposed OTFS modulation technique, which provides significant advantages over OFDM in delay–Doppler channels. We first derive the input-output relation of OTFS with ideal waveforms for delay-Doppler channels with arbitrary number of paths, with given delay and Doppler values. We show that the fractional Doppler paths (i.e., not exactly aligned with the Doppler taps) produce IDI that results in increasing the number of total effective channel paths. We then extend the input–output relation to the *practically realizable rectangular waveforms* that do not satisfy the bi-orthogonality condition. We show that the non-orthogonality results in ICI and ISI, which can be easily mitigated by applying phase shifts in the detection algorithm. Finally, we propose a low-complexity MP detection algorithm which is suitable for large-scale OTFS taking advantage of the inherent channel sparsity. Simulations results illustrate the superior performance gains of OTFS over OFDM under various channel conditions.

The rest of the chapter is organized as follows. Section 2.1 recalls the OTFS mod/demod and derives the corresponding input–output relation. In Section 2.2, we analyze the time–frequency domain and delay–Doppler domain relations for the ideal waveform case. Section 2.3 is dedicated to the case of OTFS using rectangular waveforms. Section 2.4 proposes the MP algorithm for the joint IC and detection. Finally, the simulation results are presented in Section 2.5.

2.1   System Model

In this section, we first recall the basic concepts in OTFS and then present the explicit analysis of OTFS mod/demod. More importantly, we derive the input–output relation of OTFS mod/demod for delay–Doppler channels.

2.1.1   Basic OTFS Concepts/Notations

We follow the notations in [17, 18] summarized below

– The *time–frequency signal plane* is discretized to a grid by sampling time and frequency axes at intervals T (seconds) and Δf (Hz), respectively, i.e.,

$$\Lambda = \big\{(nT, m\Delta f),\ n = 0, \ldots, N-1, m = 0, \ldots, M-1\big\}$$

for some integers $N, M > 0$.

– Modulated *time–frequency samples* $X[n, m]$, $n = 0, \ldots, N-1$, $m = 0, \ldots, M-1$ are transmitted over an OTFS frame with duration $T_f = NT$ and occupy a bandwidth $B = M\Delta f$.

– Transmit and receive pulses (or waveforms) are denoted by $g_{\mathrm{tx}}(t)$ and $g_{\mathrm{rx}}(t)$. Let $A_{g_{\mathrm{rx}}, g_{\mathrm{tx}}}(t, f)$ denote the *cross-ambiguity function* between $g_{\mathrm{tx}}(t)$ and $g_{\mathrm{rx}}(t)$, i.e.,

$$A_{g_{\mathrm{rx}}, g_{\mathrm{tx}}}(t, f) \triangleq \int g_{\mathrm{rx}}^*(t' - t) g_{\mathrm{tx}}(t') e^{-j2\pi f(t' - t)} dt'. \tag{2.1}$$

– The delay–Doppler plane is discretized to an information grid

$$\Gamma = \Big\{\Big(\frac{k}{NT}, \frac{l}{M\Delta f}\Big),\ k = 0, \ldots, N-1, l = 0, \ldots, M-1\Big\},$$

where $1/M\Delta f$ and $1/NT$ represent the quantization steps of the delay and Doppler frequency, respectively[1].

Remark 2.1. (Choice of parameters in OTFS systems) – *Given a communications system with total bandwidth $B = M\Delta f$ and latency $T_f = NT$ constraints, we may choose N, M, T (since $\Delta f = 1/T$) to support communications over a time-varying channel with maximum delay $\tau_{\max}$*

---

[1]Note that the first and second indexes, k and l, in Γ represent the Doppler and delay axis, respectively.
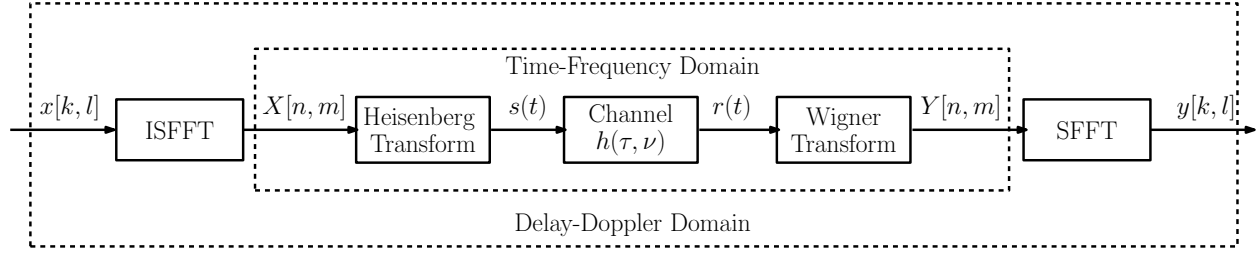
Figure 2.1: OTFS mod/demod

and maximum Doppler $\nu_{\max}$, among all channel paths. We can see that T and Δf determine the maximum supportable Doppler (i.e., $1/T$) and delay (i.e., $1/\Delta f$). Hence, it is required that $\nu_{\max} < 1/T$ and $\tau_{\max} < 1/\Delta f$ so that N and M are determined. To support a fixed data rate of NM symbols per frame, depending on the channel conditions, we can choose a larger T and smaller Δf, which results in a smaller N and larger M, respectively, or vice versa.

2.1.2 General OTFS Mod/Demod Block Diagram

The OTFS system diagram is given in Fig. 2.1. OTFS modulation is produced by a cascade of a pair of 2D transforms at both transmitter and receiver. The modulator first maps the information symbols $x[k, l]$ in the delay–Doppler domain to samples $X[n, m]$ in the time–frequency domain using the ISFFT. Next, the *Heisenberg transform* is applied to $X[n, m]$ to create the time domain signal $s(t)$ transmitted over the wireless channel. At the receiver, the time-domain signal $r(t)$ is mapped to the time–frequency domain through the *Wigner transform* (the inverse of the Heisenberg transform), and then to the delay–Doppler domain using SFFT for symbol demodulation.

2.1.3 OTFS Modulation

Consider a set of NM information symbols $\{x[k,l], k = 0, \ldots, N-1, l = 0, \ldots, M-1\}$ from a modulation alphabet of size Q $\mathbb{A} = \{a_1, \cdots, a_Q\}$ (e.g. QAM symbols), which are arranged on the delay–Doppler grid Γ.

The OTFS transmitter first maps symbols $x[k, l]$ to NM samples $X[n, m]$ on the time–frequency grid Λ using the ISFFT as follows

$$X[n, m] = \frac{1}{\sqrt{NM}} \sum_{k=0}^{N-1} \sum_{l=0}^{M-1} x[k, l] e^{j2\pi\left(\frac{nk}{N} - \frac{ml}{M}\right)} \tag{2.2}$$

for $n = 0, \ldots, N-1, m = 0, \ldots, M-1$.

Next, a time–frequency modulator converts the samples $X[n, m]$ to a continuous time waveform $s(t)$ using a transmit waveform $g_{\text{tx}}(t)$ as

$$s(t) = \sum_{n=0}^{N-1} \sum_{m=0}^{M-1} X[n, m] g_{\text{tx}}(t - nT) e^{j2\pi m \Delta f(t-nT)}. \tag{2.3}$$

As noted in [17], (2.3) is also referred to in the mathematical literature as the (discrete) Heisenberg transform [26], parametrized by $g_{\text{tx}}(t)$.

2.1.4 Wireless Transmission and Reception

The signal $s(t)$ is transmitted over a time-varying channel with complex baseband channel impulse response $h(\tau, \nu)$, which characterizes the channel response to an impulse with delay τ and Doppler ν [21]. The received signal $r(t)$ is given by (disregarding the noise to simplify notation)

$$r(t) = \int \int h(\tau, \nu) s(t - \tau) e^{j2\pi\nu(t-\tau)} d\tau d\nu. \tag{2.4}$$

Equation (2.4) represents a continuous Heisenberg transform parametrized by $s(t)$ [17]. Since typically there are only a small number of reflectors in the channel with associated delays and Dopplers, very few parameters are needed to model the channel in the delay–Doppler domain. The sparse representation of the channel $h(\tau, \nu)$ is given as

$$h(\tau, \nu) = \sum_{i=1}^{P} h_i \delta(\tau - \tau_i) \delta(\nu - \nu_i) \tag{2.5}$$

where P is the number of propagation paths; h_i, τ_i, and ν_i represent the path gain, delay, and Doppler shift (or frequency) associated with i-th path, respectively, and $\delta(\cdot)$ denotes the Dirac delta function. We denote the delay and Doppler taps for i-th path as follows

$$\tau_i = \frac{l_{\tau_i}}{M\Delta f}, \quad \nu_i = \frac{k_{\nu_i} + \kappa_{\nu_i}}{NT} \tag{2.6}$$

for integers l_{τ_i}, k_{ν_i} and real $-\frac{1}{2} < \kappa_{\nu_i} \leq \frac{1}{2}$. Specifically, l_{τ_i} and k_{ν_i} represent the indexes of the delay tap and Doppler tap corresponding to (continuous) delay τ_i and Doppler frequency ν_i, respectively.

We will refer to κ_{ν_i} as the *fractional* Doppler since it represents the fractional shift from the nearest Doppler tap k_{ν_i}. We do not need to consider fractional delays since the resolution of the sampling time $\frac{1}{M\Delta f}$ is sufficient to approximate the path delays to the nearest sampling points in typical wide-band systems [27].

2.1.5 OTFS Demodulation

At the receiver, a matched filter computes the cross-ambiguity function $A_{g_{\mathrm{rx}},r}(t,f)$ as follows

$$Y(t,f) = A_{g_{\mathrm{rx}},r}(t,f) \triangleq \int g_{\mathrm{rx}}^*(t'-t)r(t')e^{-j2\pi f(t'-t)}dt'. \tag{2.7}$$

The matched filter output is obtained by sampling $Y(t,f)$ as

$$Y[n,m] = Y(t,f)|_{t=nT,f=m\Delta f} \tag{2.8}$$

for $n = 0, \ldots, N-1$ and $m = 0, \ldots, M-1$. Operations (2.7) and (2.8) are referred as the *Wigner transform*. In the following theorem, we characterize the relationship between time–frequency output samples $Y[n,m]$ and input samples $X[n,m]$.

Theorem 2.1. *OTFS time–frequency domain analysis. The following input–output relation of OTFS in time–frequency domain is given by*

$$Y[n,m] = \sum_{n'=0}^{N-1}\sum_{m'=0}^{M-1} H_{n,m}[n',m']X[n',m'], \tag{2.9}$$

where

$$H_{n,m}[n',m'] =$$
$$\int\int h(\tau,\nu)A_{g_{\mathrm{rx}},g_{\mathrm{tx}}}((n-n')T-\tau,(m-m')\Delta f-\nu)e^{j2\pi(\nu+m'\Delta f)((n-n')T-\tau)}e^{j2\pi\nu n'T}d\tau d\nu. \tag{2.10}$$

Proof: The proof is given in Appendix A.1. ∎

We can see that the terms $H_{n,m}[n',m']$ include the combined effects of the transmit pulse, channel

response, and receive pulse. Note that similar results have been presented for the case of PS-OFDM [30,31].

Next, the SFFT is applied on the samples $Y[n, m]$ to obtain symbols $y[k, l]$ in the delay–Doppler domain

$$y[k,l] = \frac{1}{\sqrt{NM}} \sum_{n=0}^{N-1} \sum_{m=0}^{M-1} Y[n,m] e^{-j2\pi\left(\frac{nk}{N} - \frac{ml}{M}\right)}. \tag{2.11}$$

Theorem 2.1 provides the basis of the study of OTFS in two special cases, namely using *ideal waveforms* (Section 2.2) and more practical *rectangular waveforms* (Section 2.3). We will obtain explicit input-output relations using the delay–Doppler channel model (2.5) for both cases.

2.2 OTFS With Ideal Waveforms

The $g_{\mathrm{rx}}(t)$ and $g_{\mathrm{tx}}(t)$ pulses are said to be ideal if they satisfy the *bi-orthogonal property* [17]

$$A_{g_{\mathrm{rx}},g_{\mathrm{tx}}}(t,f)|_{t=nT+(-\tau_{\max},\tau_{\max}),f=m\Delta f+(-\nu_{\max},\nu_{\max})} = \delta[n]\delta[m]q_{\tau_{\max}}(t)q_{\nu_{\max}}(f) \tag{2.12}$$

where $q_a(x) = 1$ for $x \in (-a, a)$ and zero otherwise. Equivalently, the cross-ambiguity function $A_{g_{\mathrm{rx}},g_{\mathrm{tx}}}(t,f) = 0$ for $t \in (nT - \tau_{\max}, nT + \tau_{\max})$ and $f \in (m\Delta f - \nu_{\max}, m\Delta f + \nu_{\max}), \forall n, m$ except for $n = 0, m = 0$, where $A_{g_{\mathrm{rx}},g_{\mathrm{tx}}}(t,f) = 1$ for $t \in (-\tau_{\max}, \tau_{\max})$ and $f \in (-\nu_{\max}, \nu_{\max})$.

Unfortunately, ideal pulses cannot be realized in practice but can be approximated by waveforms with a support concentrated as much as possible in time and in frequency, given the constraint imposed by the uncertainty principle. Nevertheless, it is important to study the error performance of OTFS with ideal waveforms since it serves as a lower bound on the performance of OTFS with practically realizable waveforms such as rectangular waveforms, etc.

2.2.1 Time–Frequency Domain Analysis

For ideal waveforms, the time–frequency relation can be obtained as a special case of Theorem 2.1 [18].

Proposition 2.1. *For ideal pulses, the following result can be obtained*

$$Y[n, m] = H_{n,m}[n, m]X[n, m] \tag{2.13}$$

where

$$H_{n,m}[n, m] = \int \int h(\tau, \nu)e^{j2\pi\nu nT}e^{-j2\pi(\nu + m\Delta f)\tau}d\tau d\nu.$$

Proof: From (2.10), we observe that the value of $H_{n,m}[n', m']$ is non-zero only at $n' = n$ and $m' = m$ for the ideal pulses satisfying the bi-orthogonal property (2.12). Hence, the result in (2.13) follows from (2.9) by considering only the term with $n' = n$, $m' = m$ in the summations. ∎

2.2.2 Delay–Doppler Domain Analysis

Input–output relationship

We now apply SFFT on $Y[n, m]$ in (2.13) to obtain the symbols $y[k, l]$ in the delay–Doppler domain. The following proposition describes the input–output relation in delay–Doppler domain [18].

Proposition 2.2. *For ideal pulses, the following input-output relation holds*

$$y[k, l] = \frac{1}{NM}\sum_{k'=0}^{N-1}\sum_{l'=0}^{M-1} x[k', l']h_w[k - k', l - l'], \tag{2.14}$$

where $h_w[\cdot, \cdot]$ is a sampled version of the impulse response function

$$h_w[k - k', l - l'] = h_w(\nu, \tau)\big|_{\nu = \frac{k-k'}{NT}, \tau = \frac{l-l'}{M\Delta f}}$$

for $h_w(\nu, \tau)$ being the circular convolution of the channel response with the SFFT of a rectangular windowing function in the time-frequency domain

$$h_w(\nu, \tau) = \int \int h(\tau', \nu')w(\nu - \nu', \tau - \tau')e^{-j2\pi\nu\tau}d\tau' d\nu', \tag{2.15}$$

$$w(\nu, \tau) = \sum_{n=0}^{N-1}\sum_{m=0}^{M-1} 1 \cdot e^{-j2\pi(\nu nT - \tau m\Delta f)}. \tag{2.16}$$

Proof: The proof is relegated to the Appendix A.2. ∎

Inter-Doppler interference (IDI) analysis

From (2.14), we can see that a received signal $y[k,l]$ is a linear combination of all the transmitted signals $x[k',l']$, $k' = 0, \ldots, N-1, l' = 0, \ldots, M-1$. Consequently, the input-output relation (2.14) can be represented as a linear system with NM variables $x[k',l']$. Since N and M tend to be very large for practical OTFS systems, the detection complexity can be prohibitive. In the following, by using (2.5) as the sparse representation of the delay–Doppler channel, (2.14) reduces to a sparse linear system, where each received signal can be approximately expressed as a linear combination of only a few transmitted signals. Such sparsity will then be exploited in Section 2.4 to devise a low-complexity yet efficient iterative detection algorithm based on message passing on the factor graph representation.

By substituting (2.5) and (2.16) into (2.15), we obtain

$$
\begin{aligned}
h_w(\nu, \tau) &= \sum_{i=1}^{P} h_i e^{-j2\pi\nu_i\tau_i} \, w(\nu - \nu_i, \tau - \tau_i) \\
&= \sum_{i=1}^{P} h_i e^{-j2\pi\nu_i\tau_i} \, \mathcal{G}(\nu, \nu_i) \, \mathcal{F}(\tau, \tau_i),
\end{aligned}
$$

where we have denoted

$$
\begin{aligned}
\mathcal{F}(\tau, \tau_i) &\triangleq \sum_{m'=0}^{M-1} e^{j2\pi(\tau-\tau_i)m'\Delta f}, \\
\mathcal{G}(\nu, \nu_i) &\triangleq \sum_{n'=0}^{N-1} e^{-j2\pi(\nu-\nu_i)n'T}.
\end{aligned}
$$

Let us first evaluate $\mathcal{F}(\tau, \tau_i)$ at $\tau = \frac{l-l'}{M\Delta f}$ as

$$
\mathcal{F}\left(\frac{l-l'}{M\Delta f}, \tau_i\right) = \sum_{m'=0}^{M-1} e^{j\frac{2\pi}{M}(l-l'-l_{\tau_i})m'} = \frac{e^{j2\pi(l-l'-l_{\tau_i})} - 1}{e^{j\frac{2\pi}{M}(l-l'-l_{\tau_i})} - 1} \tag{2.17}
$$

recalling that l_{τ_i} is the delay tap of i-th path with a delay τ_i defined in (2.6). From (2.17), we see

that

$$\mathcal{F}\left(\frac{l-l'}{M\Delta f},\tau_i\right) = \begin{cases} M, & [l-l'-l_{\tau_i}]_M = 0, \\ \\ 0, & \text{otherwise,} \end{cases}$$

where $[\cdot]_M$ represents mod M operation, i.e., $\mathcal{F}\left(\frac{l-l'}{M\Delta f},\tau_i\right)$ equals to M for $l' = [l-l_{\tau_i}]_M$ and is zero otherwise.

Similarly, we can evaluate

$$\mathcal{G}\left(\frac{k-k'}{NT},\nu_i\right) = \frac{e^{-j2\pi(k-k'-k_{\nu_i}-\kappa_{\nu_i})} - 1}{e^{-j\frac{2\pi}{N}(k-k'-k_{\nu_i}-\kappa_{\nu_i})} - 1}. \tag{2.18}$$

Due to the fractional κ_{ν_i}, we can see that for a given k, $\mathcal{G}\left(\frac{k-k'}{NT},\nu_i\right) \neq 0$, for all k'.

We will show that the magnitude of $\frac{1}{N}\mathcal{G}\left(\frac{k-k'}{NT},\nu_i\right)$ has a peak at $k' = k - k_{\nu_i}$ and decreases as k' moves away from $k - k_{\nu_i}$. From (2.18), after some manipulations, we have

$$\left|\frac{1}{N}\mathcal{G}\left(\frac{k-k'}{NT},\nu_i\right)\right| = \left|\frac{\sin(N\theta)}{N\sin(\theta)}\right|$$

where we set $\theta \triangleq -\frac{\pi}{N}(k-k'-k_{\nu_i}-\kappa_{\nu_i})$. It can be easily shown that

$$\left|\frac{\sin(N\theta)}{N\sin(\theta)}\right| = \left|\frac{\sin((N-1)\theta)\cos(\theta) + \sin(\theta)\cos((N-1)\theta)}{N\sin(\theta)}\right|$$
$$\leq \frac{N-1}{N}|\cos(\theta)| + \frac{1}{N}. \tag{2.19}$$

Here, we used the inequality, $|\sin(N\theta)| \leq N|\sin(\theta)|$, which can be proven by induction. The upper bound (2.19) is tight for small values of θ (when both sides are close to 1) and it has a peak at the smallest value of θ when $k' = k - k_{\nu_i}$. As $|\theta|$ increases (due to k' moving away from $k - k_{\nu_i}$), the upper bound decreases with (approximate) slope of $\frac{\pi}{N}(k-k'-k_{\nu_i}-\kappa_{\nu_i})$. Since N is quite large in OTFS, the function decreases rapidly.

From the above analysis, we need to consider only a small number $2N_i + 1$, for some $N_i > 0$, of significant values of $\mathcal{G}\left(\frac{k-k'}{NT},\nu_i\right)$ in (2.18) around the peak $k - k_{\nu_i}$, i.e., $[k - k_{\nu_i} - N_i]_N \leq k' \leq [k - k_{\nu_i} + N_i]_N$, where $N_i \ll N$. Using this approximation, we can now express the receive signal

$y[k,l]$ in (2.14) as

$$
\begin{aligned}
y[k,l] &\approx \sum_{i=1}^{P} \sum_{k'=[k-k_{\nu_i}-N_i]_N}^{[k-k_{\nu_i}+N_i]_N} \left(\frac{e^{-j2\pi(k-k_{\nu_i}-k'-\kappa_{\nu_i})}-1}{Ne^{-j\frac{2\pi}{N}(k-k_{\nu_i}-k'-\kappa_{\nu_i})}-N} \right) h_i e^{-j2\pi\nu_i\tau_i} x\left[k',[l-l_{\tau_i}]_M\right] \\
&\approx \sum_{i=1}^{P} \sum_{q=-N_i}^{N_i} \left(\frac{e^{-j2\pi(-q-\kappa_{\nu_i})}-1}{Ne^{-j\frac{2\pi}{N}(-q-\kappa_{\nu_i})}-N} \right) h_i e^{-j2\pi\nu_i\tau_i} x\left[[k-k_{\nu_i}+q]_N,[l-l_{\tau_i}]_M\right]. \quad (2.20)
\end{aligned}
$$

In the simulation result section, we will demonstrate that for $N = 128$, by choosing $N_i = 10$, negligible performance loss is incurred. From (2.20), we can see that the received signal $y[k,l]$ is a linear combination of $S = \sum_{i=1}^{P} 2N_i + 1$ transmitted signals. Out of $2N_i + 1$ transmitted signals in i-th path, the signal corresponding to $q = 0$, $x\left[[k-k_{\nu_i}]_N,[l-l_{\tau_i}]_M\right]$, contributes the most and all the other $2N_i$ signals can be seen as interference. Such interference is due to the transmitted signals that are neighboring $x\left[[k-k_{\nu_i}]_N,[l-l_{\tau_i}]_M\right]$ in the Doppler domain and we refer to this interference as *inter Doppler interference (IDI)*. Further, the number of transmitted signals S affecting the received signal $y[k,l]$ in (2.20) is much smaller than NM in (2.14). Hence, the graph (or linear system) describing (2.20) is sparsely-connected.

Special channel model cases

The above input-output expression simplifies for the following special cases.

i) Ideal channel: Assuming $h(\tau,\nu) = \delta(\tau)\delta(\nu)$, the received signal becomes

$$
y[k,l] = x[k,l]
$$

and behaves as an AWGN channel as expected.

ii) No fractional Doppler (i.e., $\kappa_{\nu_i} = 0, \forall i$): Assuming that Doppler frequencies exactly coincide with Doppler taps, the received signal can be obtained by replacing $N_i = 0$ in (2.20), i.e.,

$$
y[k,l] = \sum_{i=1}^{P} h_i e^{-j2\pi\nu_i\tau_i} x[[k-k_{\nu_i}]_N,[l-l_{\tau_i}]_M].
$$

For each path, the transmitted signal is circularly shifted by the delay and Doppler taps and scaled by the associated channel gain.

2.3 OTFS With Rectangular Waveforms

Since the ideal pulses cannot be realized in practice, we now analyze the OTFS with the rectangular pulses at both the transmitter and receiver. These pulses do not satisfy the bi-orthogonality conditions and generate some interference which degrades the system performance. Here, we analyze the effect of such interference and show that it can be compensated to achieve the ideal pulses performance.

We assume the rectangular pulse has amplitude $1/\sqrt{T}$ for $t \in [0, T]$ and 0 at all other values, to have unit energy.

2.3.1 Time–Frequency Domain Analysis

For the rectangular pulses, we can see that the cross-ambiguity term in the time–frequency relation of Theorem 2.1, $A_{g_{\mathrm{rx}}, g_{\mathrm{tx}}}((n - n')T - \tau, (m - m')\Delta f - \nu)$ is non-zero for $|\tau| < \tau_{\max}$ $|\nu| < \nu_{\max}$ only when $n' = n$ and $n' = n - 1$, since $g_{\mathrm{tx}}(t)$ and $g_{\mathrm{rx}}(t)$ are pulses of duration T and $\tau_{\max} \ll T$. Hence, the time–frequency relation (2.9) becomes

$$
\begin{aligned}
Y[n, m] &= \sum_{n'=n-1}^{n} \sum_{m'=0}^{M-1} H_{n,m}[n', m'] X[n', m'] \\
&= H_{n,m}[n, m] X[n, m] + \sum_{m'=0, m' \neq m}^{M-1} H_{n,m}[n, m'] X[n, m'] + \sum_{m'=0}^{M-1} H_{n,m}[n-1, m'] X[n-1, m'].
\end{aligned}
$$

(2.21)

The second term in (2.21) can be seen as the total interference from the samples $X[n, m']$ at different frequencies $m' \neq m$, but in the same time slot n as the current sample $X[n, m]$. On the other hand, the third term in (2.21) accumulates the interference from the samples $X[n-1, m']$ in the previous time slot $n - 1$. Hence, we call the second and third terms as the *inter carrier interference (ICI)* and *inter symbol interference (ISI)*, respectively. The interference depends on the delay τ and Doppler ν of the channel. In particular, they are affected by the value of the cross-ambiguity function $A_{g_{\mathrm{rx}}, g_{\mathrm{tx}}}((n - n')T - \tau, (m - m')\Delta f - \nu)$ in $H_{n,m}[n', m']$. In the following, we focus on the cross-ambiguity function for ICI and ISI.

ICI analysis

Fix n, m. We note that the cross-ambiguity function in the $H_{n,m}[n, m'], m' \neq m$ term of ICI, $A_{g_{\text{rx}}, g_{\text{tx}}}(-\tau, (m - m')\Delta f - \nu)$, is independent of n, and is computed for the i-th channel path with delay τ_i and Doppler ν_i (i.e., see (2.5)) as

$$A_{\text{ici}} \triangleq \int g_{\text{rx}}^*(t' + \tau_i)g_{\text{tx}}(t')e^{-j2\pi((m-m')\Delta f - \nu_i))(t'+\tau_i)}dt'.$$

We discard the dependency of A_{ici} on (m, m', τ_i, ν_i) for simplicity. Since the received signal $r(t)$ is sampled at intervals of T/M (or $1/(M\Delta f)$), we can compute A_{ici} as

$$A_{\text{ici}} = \frac{1}{M} \sum_{p=0}^{M-1-l_{\tau_i}} e^{-j2\pi((m-m')\Delta f - \nu_i)\left(\frac{p}{M\Delta f} + \tau_i\right)}. \tag{2.22}$$

Recall that the pulses $g_{\text{tx}}(t)$ and $g_{\text{rx}}(t)$ have duration T, and l_{τ_i} is the delay tap defined in (2.6). The amplitude of A_{ici} is

$$\begin{aligned}
|A_{\text{ici}}| &= \frac{1}{M} \left| \sum_{p=0}^{M-1-l_{\tau_i}} e^{-j2\pi((m-m')\Delta f - \nu_i)\frac{p}{M\Delta f}} \right| \\
&= \frac{\left| e^{-j2\pi\left(m-m' - \frac{k_{\nu_i} + \kappa_{\nu_i}}{N}\right)\frac{M-l_{\tau_i}}{M}} - 1 \right|}{\left| Me^{-j2\pi\left(m-m' - \frac{k_{\nu_i} + \kappa_{\nu_i}}{N}\right)\frac{1}{M}} - M \right|}.
\end{aligned}$$

Similar to the analysis of (2.18), we can observe that $|A_{\text{ici}}|$ decreases as m' moves away from m. It implies that the ICI becomes less as the interfering subcarriers are further away from the interfered subcarrier. We can also see that an increase in Doppler (i.e., $k_{\nu_i} + \kappa_{\nu_i}$) increases the number of neighboring subcarriers that interfere with the present subcarrier. This is similar to the fractional Doppler effect studied for (2.18).

ISI analysis

Similar to the ICI analysis, the cross-ambiguity function in the $H_{n,m}[n-1, m']$ term of ISI, $A_{\text{isi}} \triangleq A_{g_{\text{rx}}, g_{\text{tx}}}(T - \tau, (m - m')\Delta f - \nu)$, is computed for the i-th channel path as

$$A_{\text{isi}} = \frac{1}{M} \sum_{p=M-l_{\tau_i}}^{M-1} e^{-j2\pi((m-m')\Delta f - \nu_i)\left(\frac{p}{M\Delta f} + \tau_i - T\right)}. \tag{2.23}$$

The amplitude $|A_{\text{isi}}|$ also has similar properties of $|A_{\text{ici}}|$, where it reduces as m' moves away from m implying that the ISI is smaller for interfering symbols further away (in the frequency axis) from the interfered symbol.

Note that the terms that affect the ICI and ISI in the summations (2.22) and (2.23) are mutually exclusive, i.e., $p = 0$ to $M - 1 - l_{\tau_i}$ contributes to ICI whereas $p = M - l_{\tau_i}$ to $M - 1$ contributes to ISI. This property helps in differentiating the ICI and ISI effects in delay–Doppler domain, which will be studied below.

2.3.2 Delay–Doppler Domain Analysis

We now characterize the input–output relation in delay–Doppler domain for OTFS with rectangular pulses.

Theorem 2.2. *The received signal $y[k, l]$ in delay–Doppler domain with the rectangular pulses can be written as*

$$y[k, l] \approx \sum_{i=1}^{P} \sum_{q=-N_i}^{N_i} h_i e^{j2\pi\left(\frac{l-l_{\tau_i}}{M}\right)\left(\frac{k_{\nu_i} + \kappa_{\nu_i}}{N}\right)} \alpha_i(k, l, q) x\left[[k - k_{\nu_i} + q]_N, [l - l_{\tau_i}]_M\right] \tag{2.24}$$

where we have

$$\alpha_i(k, l, q) = \begin{cases} \frac{1}{N} \beta_i(q) & l_{\tau_i} \leq l < M \\ \frac{1}{N} \left(\beta_i(q) - 1\right) e^{-j2\pi \frac{[k - k_{\nu_i} + q]_N}{N}} & 0 \leq l < l_{\tau_i} \end{cases}$$

$$\beta_i(q) = \frac{e^{-j2\pi(-q - \kappa_{\nu_i})} - 1}{e^{-j\frac{2\pi}{N}(-q - \kappa_{\nu_i})} - 1}. \tag{2.25}$$

Proof: The proof is relegated to the Appendix A.3. ∎

Note that the approximation error in (2.24) is very small and it reduces by increasing N (see (A.25) in Appendix A.3). Theorem 2.2 implies that the ICI and ISI in time–frequency domain are converted to simple phase shifts in the delay–Doppler domain. Moreover, from (2.20) and (2.24), we can observe that the number of transmitted signals that affects a received signal is the same for both ideal and rectangular pulse cases. The only difference is that the channel is shifted by an additional phase that depends on the location of the transmitted signal in the delay–Doppler plane (i.e., k and l).

Special channel model cases: Let us consider the above input-output expression (2.24) for the special cases mentioned in Section 2.2.

i) Ideal channel: The received signal becomes

$$y[k,l] = x[k,l],$$

which is the same as the ideal pulses case since the rectangular pulses satisfy the bi-orthogonal property in (2.12) when the channel is ideal (i.e., $\tau_{\max} = 0$ and $\nu_{\max} = 0$). This can be seen easily by observing (2.1) at $t = nT$ and $f = m\Delta f$.

ii) No fractional Doppler (i.e., $\kappa_{\nu_i} = 0, \forall i$): Equation (2.24) simplifies to

$$y[k,l] \approx \sum_{i=1}^{P} h_i e^{j2\pi\left(\frac{l-l_{\tau_i}}{M}\right)\frac{k_{\nu_i}}{N}} \alpha_i(k,l) x[[k - k_{\nu_i}]_N, [l - l_{\tau_i}]_M],$$

where

$$\alpha_i(k,l) = \begin{cases} 1 & l_{\tau_i} \leq l < M \\ \frac{N-1}{N} e^{-j2\pi\left(\frac{[k-k_{\nu_i}]_N}{N}\right)} & 0 \leq l < l_{\tau_i}. \end{cases}$$

In this case, IDI does not appear as in the case of ideal pulses.

2.4 Message Passing Algorithm for Joint Interference Cancellation and Detection

We now propose a message passing (MP) algorithm for OTFS using the input-output relation in (2.20) (or (2.24)).

2.4.1 Low-Complexity MP Detection Algorithm

The received signal in vectorized form can be written as

$$\mathbf{y} = \mathbf{H}\,\mathbf{x} + \mathbf{z} \tag{2.26}$$

where $\mathbf{y}$ and $\mathbf{z}$ are complex vectors of dimension $NM \times 1$ with elements denoted by $y[d]$ and $z[d], 1 \leq d \leq NM$, respectively; $\mathbf{H}$ is a $NM \times NM$ complex matrix with elements $H[d,c], 1 \leq d, c \leq NM$; $\mathbf{x}$ is the information vector of dimension $NM \times 1$ with elements $x[c] \in \mathbb{A}, 1 \leq c \leq NM$. [2] The elements of $\mathbf{y}, \mathbf{x}$, and $\mathbf{H}$ are determined from (2.20) (or (2.24)) and $\mathbf{z}$ is the noise vector. Due to mod N and mod M operations in (2.20), we observe that only $S = \sum_{i=1}^{P}(2N_i + 1)$ elements out of NM are non-zero in each row and column of $\mathbf{H}$. Recall that P is the number of propagation paths. We can see that since S is much smaller than NM, $\mathbf{H}$ is a sparse matrix. Let $\mathcal{I}(d)$ and $\mathcal{J}(c)$ denote the sets of indexes with non-zero elements in the d-th row and c-th column, respectively, then $|\mathcal{I}(d)| = |\mathcal{J}(c)| = S$ for all rows and columns. Note that although (2.26) applies to both ideal pulses case in (2.20) and rectangular pulses case in (2.24), with different matrices $\mathbf{H}$, the number of non-zero elements S in each row and column of $\mathbf{H}$ remains the same for both cases. This condition helps in compensating ICI and ISI of rectangular pulses with the same complexity detection algorithm of ideal pulses.

Based on (2.26), we model the system as a sparsely-connected factor graph with NM variable nodes corresponding to $\mathbf{x}$ and NM observation nodes corresponding to $\mathbf{y}$. In this factor graph, each observation node $y[d]$ is connected to the set of S variable nodes $\{x[c], c \in \mathcal{I}(d)\}$. Similarly, each variable node $x[c]$ is connected to the set of S observation nodes $\{y[d], d \in \mathcal{J}(c)\}$.

From (2.26), the joint maximum a posterior probability (MAP) detection rule for estimating the

---

[2]The proposed algorithm can also be applied for the corresponding real valued systems which is beneficial for higher order QAM modulation. Here, for the general case, we consider a complex valued system.
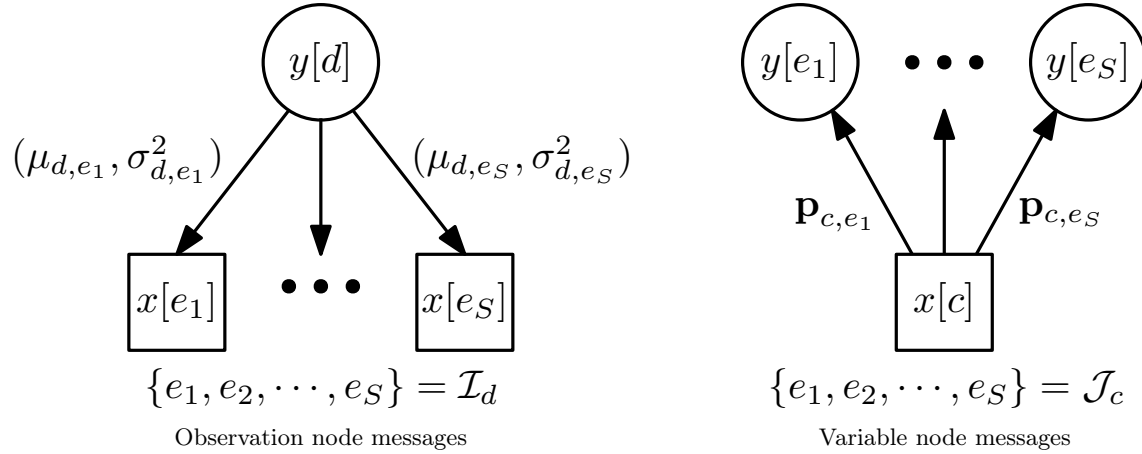
Figure 2.2: Messages in factor graph

transmitted signals is given by

$$\widehat{\mathbf{x}} = \underset{\mathbf{x} \in \mathbb{A}^{NM \times 1}}{\arg \max} \ \Pr\left(\mathbf{x} \mid \mathbf{y}, \mathbf{H}\right),$$

which has a complexity exponential in NM. Since the joint MAP detection can be intractable for practical values of N and M, we consider the symbol-by-symbol MAP detection rule for $c = 1, \ldots, NM$

$$\widehat{x}[c] = \underset{a_j \in \mathbb{A}}{\arg \max} \ \Pr\left(x[c] = a_j \mid \mathbf{y}, \mathbf{H}\right)$$

$$= \underset{a_j \in \mathbb{A}}{\arg \max} \ \frac{1}{Q} \Pr\left(\mathbf{y} \mid x[c] = a_j, \mathbf{H}\right) \tag{2.27}$$

$$\approx \underset{a_j \in \mathbb{A}}{\arg \max} \ \prod_{d \in \mathcal{J}_c} \Pr\left(y[d] \mid x[c] = a_j, \mathbf{H}\right). \tag{2.28}$$

In (2.27), we assume all the transmitted symbols $a_j \in \mathbb{A}$ are equally likely and in (2.28) we assume the components of $\mathbf{y}$ are approximately independent for a given $x[c]$, due to the sparsity of $\mathbf{H}$. That is, we assume the interference terms $\zeta_{d,c}^{(i)}$ defined in (2.29) are independent for a given c. In order to solve the approximate symbol-by-symbol MAP detection in (2.28), we propose a MP detector which has a linear complexity in NM. Similarly to [25], for each $y[d]$, a variable $x[c]$ is isolated from the other interference terms, which are then approximated as Gaussian noise with an easily computable mean and variance.

In the MP algorithm, the mean and variance of the interference terms are used as messages from observation nodes to variable nodes. On the other hand, the message passed from a variable

node $x[c]$ to the observation nodes $y[d], d \in \mathcal{J}(c)$, is the probability mass function (pmf) of the alphabet $\mathbf{p}_{c,d} = \{p_{c,d}(a_j) | a_j \in \mathbb{A}\}$. Fig. 2.2 shows the connections and the messages passed between the observation and variable nodes. The MP algorithm is described in **Algorithm 2.1**.

Algorithm 2.1 MP algorithm for OTFS symbol detection

1: **Input**: Received signal $\mathbf{y}$, channel matrix $\mathbf{H}$.
2: **Initialize**: pmf $\mathbf{p}_{c,d}^{(0)} = 1/Q, c = 1, \cdots, NM, d \in \mathcal{J}(c)$, iteration count $i = 1$.
3: **repeat**
4:     Observation nodes $y[d]$ compute the means $\mu_{d,c}^{(i)}$ and variances $(\sigma_{d,c}^{(i)})^2$ of Gaussian random variables $\zeta_{d,c}^{(i)}$ using $\mathbf{p}_{c,d}^{(i-1)}$ and pass them to variables nodes $x[c], c \in \mathcal{I}(d)$.
5:     Variable nodes $x[c]$ update $\mathbf{p}_{c,d}^{(i)}$ using $\mu_{d,c}^{(i)}$, $(\sigma_{d,c}^{(i)})^2$, and $\mathbf{p}_{c,d}^{(i-1)}$ and pass them to observation nodes $y[d], d \in \mathcal{J}(c)$.
6:     Compute convergence indicator $\eta^{(i)}$.
7:     Update the decision on the transmitted symbols $\widehat{x}[c], c = 1, \ldots, NM$ if needed.
8:     $i \leftarrow i + 1$
9: **until** Stopping criteria
10: **Output**: The decision on transmitted symbols $\widehat{x}[c]$.

The details of the steps in iteration i in the MP algorithm are detailed below.

Message passings from observation nodes $y[d]$ to variable nodes $x[c], c \in \mathcal{I}(d)$: The mean $\mu_{d,c}^{(i)}$ and variance $(\sigma_{d,c}^{(i)})^2$ of the interference, approximately modeled as a Gaussian random variable $\zeta_{d,c}^{(i)}$ defined as

$$y[d] = x[c]H[d,c] + \underbrace{\sum_{e \in \mathcal{I}(d), e \neq c} x[e]H[d,e] + z[d]}_{\zeta_{d,c}^{(i)}}, \tag{2.29}$$

can be computed as

$$\mu_{d,c}^{(i)} = \sum_{e \in \mathcal{I}(d), e \neq c} \sum_{j=1}^{Q} p_{e,d}^{(i-1)}(a_j) a_j H[d,e], \tag{2.30}$$

and

$$(\sigma_{d,c}^{(i)})^2 = \sum_{e \in \mathcal{I}(d), e \neq c} \left(\sum_{j=1}^{Q} p_{e,d}^{(i-1)}(a_j) |a_j|^2 |H[d,e]|^2 - \left| \sum_{j=1}^{Q} p_{e,d}^{(i-1)}(a_j) a_j H[d,e] \right|^2 \right) + \sigma^2. \tag{2.31}$$

Message passings from variable nodes $x[c]$ to observation nodes $y[d], d \in \mathcal{J}(c)$: The pmf vector $\mathbf{p}_{c,d}^{(i)}$ can be updated as

$$p_{c,d}^{(i)}(a_j) = \Delta \cdot \tilde{p}_{c,d}^{(i)}(a_j) + (1 - \Delta) \cdot p_{c,d}^{(i-1)}(a_j), a_j \in \mathbb{A} \tag{2.32}$$

where $\Delta \in (0, 1]$ is the *damping factor* used to improve the performance by controlling the convergence speed [32], and

$$\tilde{p}_{c,d}^{(i)}(a_j) \propto \prod_{e \in \mathcal{J}(c), e \neq d} \Pr\left(y[e] \Big| x[c] = a_j, \mathbf{H}\right)$$

$$= \prod_{e \in \mathcal{J}(c), e \neq d} \frac{\xi^{(i)}(e, c, j)}{\sum_{k=1}^{Q} \xi^{(i)}(e, c, k)} , \tag{2.33}$$

where $\xi^{(i)}(e, c, k) = \exp\left(\dfrac{-\left|y[e] - \mu_{e,c}^{(i)} - H_{e,c}a_k\right|^2}{(\sigma_{e,c}^{(i)})^2}\right)$.

Convergence indicator: Compute the convergence indicator $\eta^{(i)}$ as

$$\eta^{(i)} = \frac{1}{NM} \sum_{c=1}^{NM} \mathbb{I}\left(\max_{a_j \in \mathbb{A}} p_c^{(i)}(a_j) \geq 1 - \gamma\right), \tag{2.34}$$

for some small $\gamma > 0$ and where

$$p_c^{(i)}(a_j) = \prod_{e \in \mathcal{J}(c)} \frac{\xi^{(i)}(e, c, j)}{\sum_{k=1}^{Q} \xi^{(i)}(e, c, k)} \tag{2.35}$$

and $\mathbb{I}(\cdot)$ is an indicator function which gives a value of 1, if the expression in the argument is true, and 0 otherwise.

Update decision: If $\eta^{(i)} > \eta^{(i-1)}$, then we update the decision of the transmitted symbol as

$$\hat{x}[c] = \arg\max_{a_j \in \mathbb{A}} p_c^{(i)}(a_j), \quad c = 1, \cdots, NM. \tag{2.36}$$

We update the decision on the transmitted symbols only when the current iteration can provide better estimates than the previous iteration.

Stopping criteria. The MP algorithm stops when at least one of the following conditions is satisfied.

1. $\eta^{(i)} = 1$.

2. $\eta^{(i)} < \eta^{(i^*)} - \epsilon$, where i^* is the iteration index from $\{1, \cdots, (i-1)\}$ for which $\eta^{(i^*)}$ is maximum.

3. Maximum number n_{iter} of iterations is reached.

We select $\epsilon = 0.2$ to disregard small fluctuations of η. Here, the first condition occurs in the best case, where all the symbols have converged. The second condition is useful to stop the algorithm if the current iteration provides a worse decision than the one in previous iterations.

Remark 2.2. Complexity of the proposed MP algorithm. *The complexity of one iteration involves the computation of (2.30), (2.31), (2.32), (2.34), and (2.36). More specifically, each of (2.30), (2.31), and (2.32)* [3]*, has a complexity order $\mathcal{O}(NMSQ)$. Furthermore, (2.34) and (2.36) can be computed with a complexity order $\mathcal{O}(NMQ)$* [4]*. Therefore, the overall complexity order is $\mathcal{O}(n_{\text{iter}} NMSQ)$. In simulations, we observed that the algorithm converges typically within 20 iterations (i.e., see Figure 2.4 in the illustrative result section for more references). We conclude that the IDI analysis, which includes the smart approximation of IDI, to exploit the sparsity of the delay-Doppler channel representation is a key factor in reducing the complexity of the detector (due to relatively small S). The memory requirement is dominated by the storage of $2NMSQ$ real values for $\mathbf{p}_{c,d}^{(i)}$ and $\mathbf{p}_{c,d}^{(i-1)}$. In addition, we have the messages $(\mu_{d,c}^{(i)}, (\sigma_{d,c}^{(i)})^2)$, requiring NMS complex values and NMS real values, respectively.*

2.4.2   Application of MP Detection Algorithm for OFDM Over Delay–Doppler Channels

In the simulation result section, we will compare the performance of OTFS and OFDM over delay–Doppler channels. In this section, we demonstrate that it is also possible to utilize the above MP algorithm to compensate the Doppler effects in OFDM systems.

Consider OFDM system with OFDM symbol of duration T and M subcarriers. Hence, the received signal and noise are sampled at T/M. Then, the frequency-domain signal after FFT

---

[3]In computing (2.33), first we find the $p_c^{(i)}(a_j)$ in (2.35) which requires $\mathcal{O}(NMQ)$ complexity and then we obtain (2.33) by dividing (2.35) with the term related to $e = d$ for all d, which requires $\mathcal{O}(S)$ complexity for each c. Hence, the over all complexity of (2.33) becomes $\mathcal{O}(NMSQ)$.

[4]The computation of (2.34) and (2.36) require to find the maximum element out of Q elements for each c. As (2.35) is already computed for (2.33), finding the maximum element requires $\mathcal{O}(Q)$ complexity for each c, which leads to an overall complexity of $\mathcal{O}(NMQ)$ to compute (2.34) and (2.36).

operation is given by

$$\mathbf{y} = \mathbf{W}\mathbf{H}_t\mathbf{W}^H\mathbf{x} + \mathbf{z} \tag{2.37}$$

where $\mathbf{W}$ is M-point FFT matrix, and $\mathbf{x} \in \mathbb{A}^{M \times 1}$ is the transmitted OFDM symbol. The elements $H_t[p, q]$ of time-domain channel matrix $\mathbf{H}_t$ are given in [33] as

$$H_t[p, q] = \sum_{i=1}^{P} h_i \delta \left[\left[p - q - \frac{\tau_i M}{T} \right]_M \right] e^{j\frac{2\pi(q-1)\nu_i}{M}}, p, q = 1, \ldots, M.$$

Using the $M \times M$ frequency-domain channel matrix $\mathbf{H}_{\text{ofdm}} = \mathbf{W}\mathbf{H}_t\mathbf{W}^H$, we can re-write (2.37) as

$$\mathbf{y} = \mathbf{H}_{\text{ofdm}}\mathbf{x} + \mathbf{z}. \tag{2.38}$$

Since (2.38) has the form similar to (2.26), the MP previously developed for OTFS can also be applied for OFDM symbol detection. We note that $\mathbf{H}_{\text{ofdm}}$ is *diagonally dominant* and the values of off-diagonal elements in each row decay as we move away from the diagonal entry as explained in [33]. Hence, the $\mathbf{H}_{\text{ofdm}}$ matrix is also sparse enabling the use of the proposed low-complexity MP detection algorithm.

2.5   Illustrative Results and Discussions

In this section, we simulate the error performance of uncoded OTFS and OFDM systems over delay-Doppler channels. In particular, we first study BER performance of OTFS for ideal pulses with the number of IDI interference terms N_i and MP parameter Δ. We next study the BER performance of OTFS with ideal pulses and rectangular pulses, and its comparison with OFDM.

All relevant simulation parameters are given in Table 2.1. First, ideal channel estimation is assumed, i.e., the channel impulse function $h(\tau, \nu)$ is perfectly known at the receiver. Then, we consider the effect of imperfect channel estimation on OTFS performance. For both OTFS and OFDM systems, Extended Vehicular A model (EVA) [35] is adopted as the channel model for the path delays (or delay taps) and each delay tap has a single Doppler shift generated using Jakes'

Parameter	Value
Carrier frequency	4 GHz
No. of subcarriers (M)	512
No. of OTFS symbols (N)	128
Subcarrier spacing	15 KHz
Cyclic prefix of OFDM	2.6 μs
Modulation alphabet	4-QAM, 16-QAM
UE speed (Kmph)	30, 120, 500
Channel estimation	Ideal

Table 2.1: Simulation Parameters

formula

$$\nu_i = \nu_{\max} \cos(\theta_i)$$

where $\nu_{\max}$ is the maximum Doppler shift determined by the UE speed and θ_i is uniformly distributed over $[-\pi, \pi]$. In general, the channel can have multiple paths with the same delay but different Doppler shifts. In our simulations, we consider channels with only one path for given delay. However, it is straightforward to consider multiple paths with different Doppler shifts for a given delay, and our main theoretical result in Theorem 2.2 is still valid. In order to obtain BER values, we consider 7×10^4 different channel realizations in the Monte-Carlo simulations.

We first demonstrate the effects of IDI in OTFS. Fig. 2.3 shows the BER performance of OTFS system with ideal pulses using the proposed MP detector for different number of IDI interference terms N_i with 4-QAM signaling over the delay–Doppler channel with different Doppler frequencies (i.e., UE speeds of $120, 500$ Kmph) and SNRs. Note that ICI and ISI are not present for the ideal pulses case. We consider the same N_i for all paths. We can see that there is a significant BER improvement when N_i increases from 0 to 10 and saturation thereafter. Note that $N_i = 0$ corresponds to the case when IDI is not taken into account. The results imply that fewer neighboring interference terms are sufficient to consider in the MP algorithm (e.g. $N_i = 10$) without incurring performance loss. We also observe that if IDI is not taken into account at all or an insufficient number of IDI terms is considered (i.e., $N_i \leq 5$), the error performance worsens significantly. These observations demonstrate the importance of our previous IDI analysis for suitable interference cancellation algorithm development. Also, it can be observed that for given SNR (e.g., SNR $=$
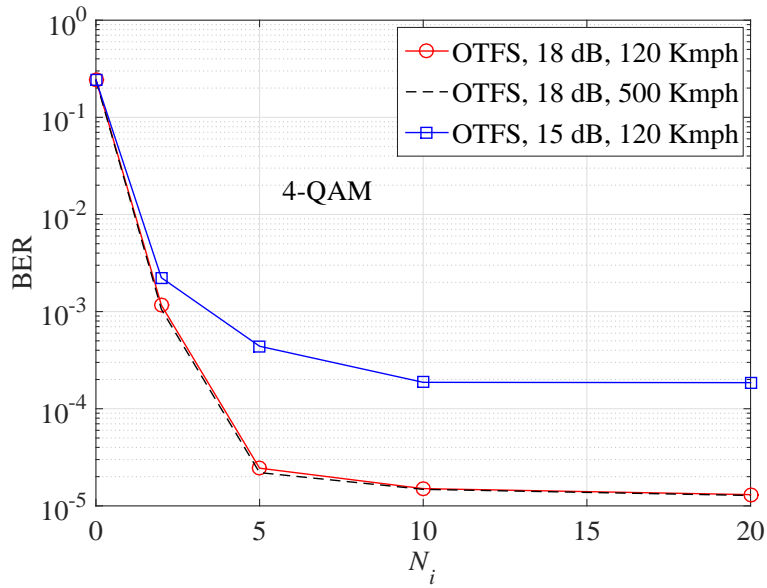
Figure 2.3: The BER performance of OTFS for different number of interference terms N_i with 4-QAM.
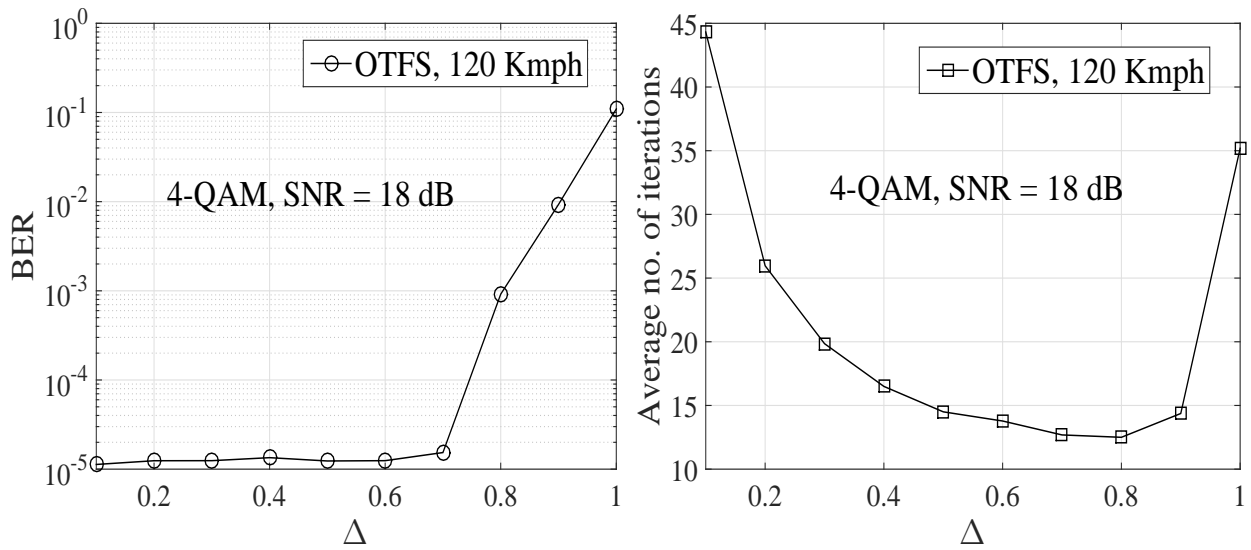
Figure 2.4: The variation of BER and average no. of iterations with Δ.

18 dB), the error performances of OTFS with different Doppler frequencies are similar since the proposed MP algorithm can effectively compensate for a wide range of channel Doppler variations as demonstrated further in the following.

In Fig. 2.4, we illustrate the BER performance and average number of iterations with ideal pulses using the MP algorithm. We fix $N_i = 10$ and vary the damping factor Δ. We consider 4-QAM signaling, SNR = 18 dB, and UE speed of 120 Kmph. We observe that, when $\Delta \leq 0.7$, the BER remains almost the same, but deteriorates thereafter. Further, when $\Delta = 0.7$, the MP algorithm converges with the least number of iterations. Hence, we choose $\Delta = 0.7$ as the optimum damping factor in terms of performance and complexity.

In Fig. 2.5, we compare the BER performance of OTFS with ideal pulses and OFDM using 4-QAM signaling over the delay-Doppler channels of different Doppler frequencies (i.e., UE speeds of $30, 120, 500$ Kmph). Note that the MP algorithm proposed in Section 2.4.2 is used for OFDM detection. We observe that OTFS outperforms OFDM by approximately 15 dB at BER of 10^{-4} thanks to the constant channel gain over all transmitted symbols in OTFS, whereas in OFDM, the overall error performance is limited by the subcarrier(s) experiencing the worse channel conditions. Moreover, OTFS exhibits the same performance at different Doppler frequencies thanks to the IDI cancellation provided by the MP detector. Similar behavior applies to OFDM, since the ICI can be removed by the MP detector. We can conclude that the performance of OTFS under the proposed MP algorithm is robust to Doppler variations and is much better than that of OFDM.

Fig. 2.6 shows the BER performance of OTFS with rectangular pulses using 4-QAM signaling for two scenarios: one with ICI and ISI cancellations (WC) and the other without (WO). In the second scenario, we observe that OTFS with rectangular pulses has an error floor incurred by the ICI and ISI. The performance degradation becomes more severe at high Doppler (e.g., 500 Kmph) due to large ICI and ISI. On the other hand, the BER performance of OTFS with rectangular pulses approaches that of OTFS with ideal pulses, when ISI and ICI are mitigated. Moreover, we can see that the proposed MP algorithm can effectively mitigate ISI and ICI and thus OTFS performance remains almost constant regardless of the Doppler frequencies. These results show that it is possible to achieve the performance of OTFS with ideal waveforms even with the more practical rectangular waveforms by using our MP algorithm together with appropriate IDI, ICI and ISI cancellation.

In Fig. 2.7, we compare the BER performance of OTFS and OFDM at a Doppler of 120 Kmph
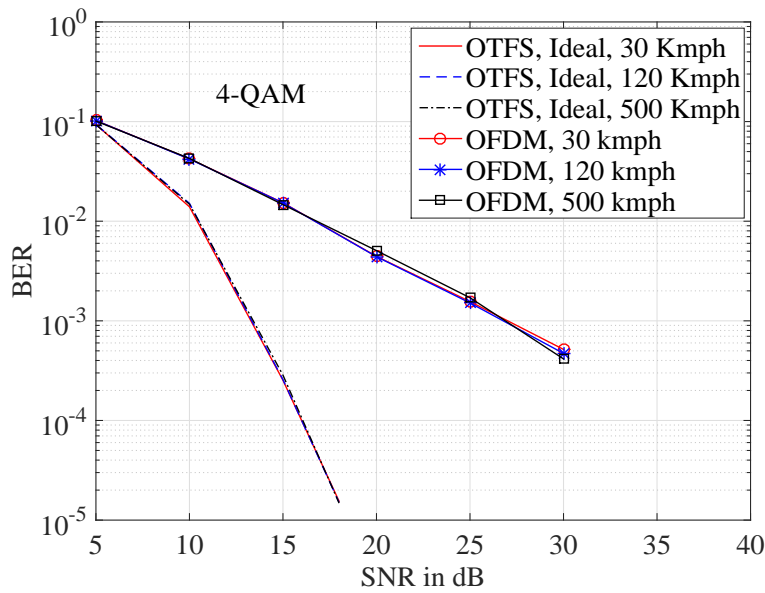
Figure 2.5: The BER performance comparison between OTFS with ideal pulses and OFDM systems at different Doppler frequencies.
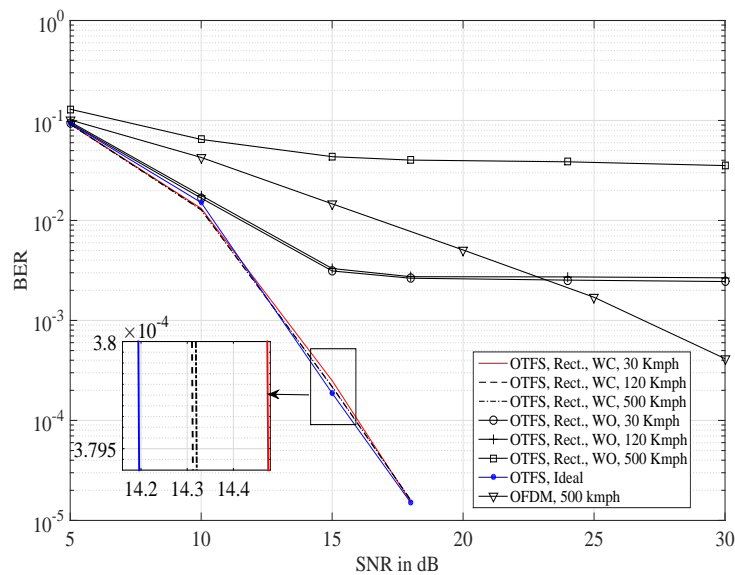
Figure 2.6: The BER performance of OTFS with rectangular and ideal pulses at different Doppler frequencies for 4-QAM.
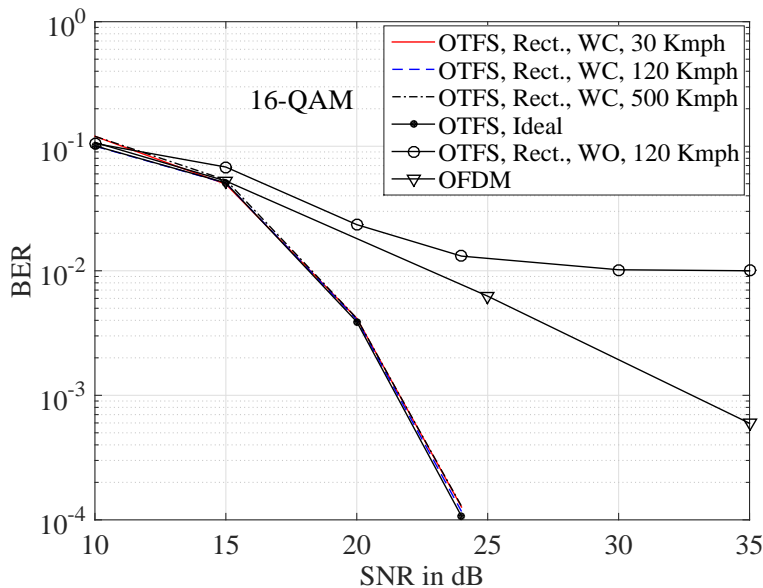
Figure 2.7: The BER performance of OTFS with rectangular and ideal pulses for 16-QAM.

using 16-QAM signaling. We observe that OTFS with ICI and ISI cancellation outperforms OFDM by 11 dB at BER $= 10^{-3}$. We also simulate OTFS at different Doppler frequencies of 30 and 500 Kmph and we observe the BER performances are similar to that of 120 Kmph.

In the next experiments, we study the performance of OTFS under different practical constraints, namely low-latency and non-ideal channel estimation.

Fig. 2.8 shows the OTFS performance under low-latency constraint where $N = 16$, $M = 128$, and 16-QAM. In this experiment, the frame duration is $T_f = NT \approx 1.1$ ms, which is much smaller than the previous case with $N = 128$ and $T_f \approx 8.8$ ms. We can observe that the OTFS performance is the same for different Dopplers. Further, the performance of OTFS degrades with low-latency because the delay–Doppler grid has lower resolution on the Doppler axis, and hence, the receiver resolves a smaller number of paths in the channel. This leads to the diversity loss over the high-latency case. When compared to OFDM, we observe that OTFS outperforms OFDM below BER $= 2 \times 10^{-3}$ with a significant diversity gain.

Fig. 2.9 shows the effect of imperfect channel estimation on the performance of OTFS with $N = 128, M = 512$, 16-QAM, and a Doppler of 120 Kmph. Here, we introduce the error in the
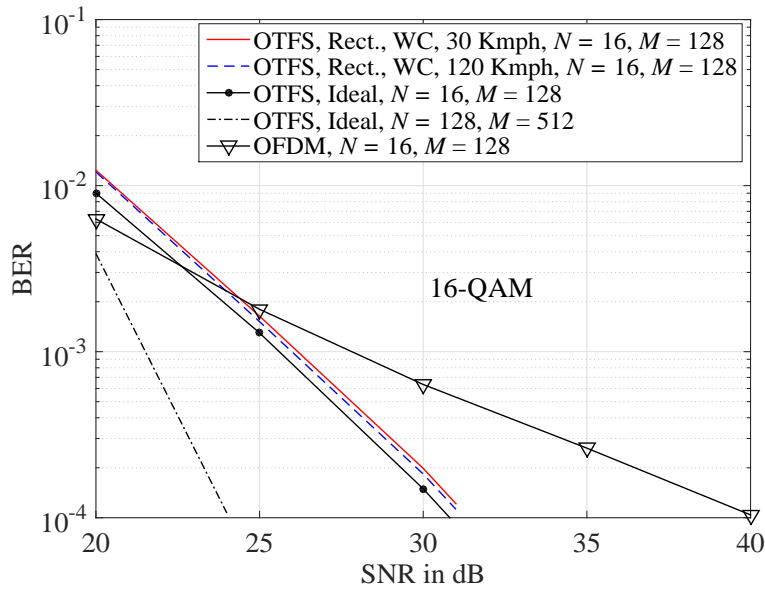
Figure 2.8: The BER performance of OTFS with rectangular pulses and low latency ($N = 16, T_f \approx 1.1$).
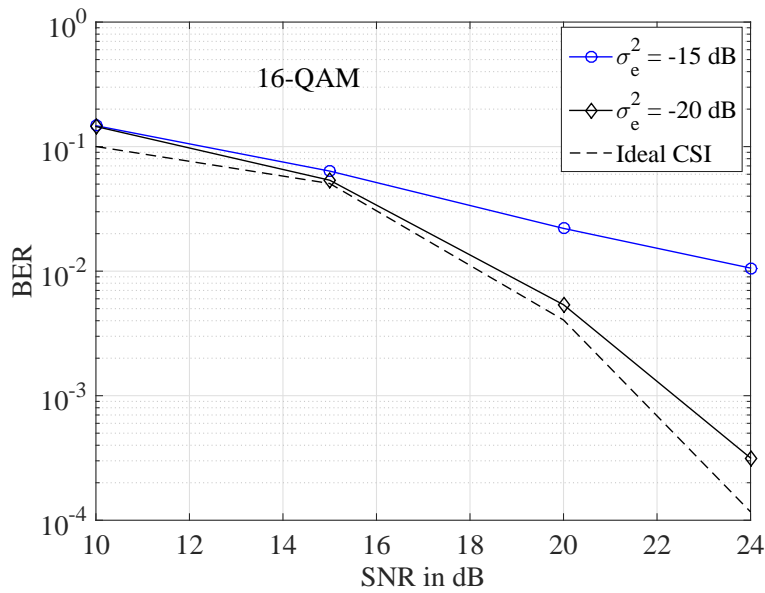
Figure 2.9: The BER performance of OTFS with channel estimation errors.

channel estimation using the model [34]

$$h'_i = h_i + n_e, 1 \leq i \leq P$$

where $n_e \sim \mathcal{CN}(0, \sigma_e^2)$ and we assume the delay and Doppler taps are perfectly estimated. From Fig. 2.9, we see that as the noise variance reduces, performance of OTFS is approaching the ideal system, particularly for a noise variance of -20 dB it is very close to the ideal system. A comprehensive study on the performance of OTFS under non-ideal channel estimation is presented in Chapter 4.

Chapter 3

OTFS With Arbitrary Pulse-Shaping Waveforms Using Simplified Matrix Notations

In this chapter, we first present an alternative proof for the OTFS input–output relation with the rectangular pulse-shaping waveforms derived in the previous chapter and generalize it to arbitrary waveforms. The proof is based on the properties of block circulant matrices which is inspired by the circulant matrix decomposition in OFDM. Next, we compare OTFS performance with different pulse-shaping waveforms, and show that the reduction of out-of-band power may introduce non-uniform channel gains for the transmitted symbols, thus impairing the overall error performance.

The rest of the chapter is organized as follows. Section 3.1 describes the OTFS system model in matrix notations. In Section 3.2, we derive the input–output relation in OTFS for arbitrary waveforms using the block circulant matrices properties.

3.1 System Model

In this section, we describe the OTFS system using matrix notations. We assume that the total duration of the transmitted signal frame is NT and the sampling interval is T/M. Moreover, we let $g_{\text{tx}}(t)$ and $g_{\text{rx}}(t)$ denote a pulse of duration $[0, T]$ repeated N times in the frame.

3.1.1 Transmitter

Let $\mathbf{X} \in \mathbb{C}^{M \times N}$ denote the two-dimensional information symbols transmitted in the delay–Doppler plane. To convert these symbols to time–frequency signals, ISFFT precoding is applied (this amounts to an M-point FFT of the columns and an N-point IFFT of the rows of $\mathbf{X}$). The "Heisenberg transform modulator" generates the time domain signal using an M-point IFFT along with the pulse-shaping waveform $g_{\mathrm{tx}}(t)$. The transmitted signal can be written as [22]

$$\mathbf{S} = \mathbf{G}_{\mathrm{tx}}\mathbf{F}_M^{\mathrm{H}}(\mathbf{F}_M\mathbf{X}\mathbf{F}_N^{\mathrm{H}}) = \mathbf{G}_{\mathrm{tx}}\mathbf{X}\mathbf{F}_N^{\mathrm{H}} \tag{3.1}$$

where the diagonal matrix $\mathbf{G}_{\mathrm{tx}}$ has the samples of $g_{\mathrm{tx}}(t)$ as its entries:

$$\mathbf{G}_{\mathrm{tx}} = \mathrm{diag}[g_{\mathrm{tx}}(0), g_{\mathrm{tx}}(T/M), \cdots, g_{\mathrm{tx}}((M-1)T/M)] \in \mathbb{C}^{M \times M}$$

(for rectangular waveforms, $\mathbf{G}_{\mathrm{tx}}$ reduces to the identity matrix $\mathbf{I}_M$). Column-wise vectorization of the $M \times N$ matrix $\mathbf{S}$ in (3.1) yields the $MN \times 1$ vector

$$\mathbf{s} = \mathrm{vec}(\mathbf{S}) = (\mathbf{F}_N^{\mathrm{H}} \otimes \mathbf{G}_{\mathrm{tx}})\mathbf{x} \tag{3.2}$$

where $\mathbf{x} = \mathrm{vec}(\mathbf{X})$ and denoting by $\otimes$ the Kronecker product. We assume that a CP of length $L-1$ (see after (3.5)) is appended to $\mathbf{s}$ before transmission.

Note that we assume only one CP for the entire OTFS frame, whereas the other works [22–24, 36, 37] considered N CP's for one OTFS frame. This design assumption considerably increases the spectral efficiency of the overall system, particularly for the cases where the value of N is large, (e.g., $64, 128$) or the CP overhead is large (e.g., 802.11ac requires 25% CP).

3.1.2 Channel

After parallel-to-serial and digital-to-analog conversion, denoting by $s(t)$ the transmitted signal, the received signal $r(t)$ can be expressed in the form [17, 18]

$$r(t) = \int \int h(\tau, \nu)s(t - \tau)e^{j2\pi\nu(t-\tau)}d\tau d\nu + w(t). \tag{3.3}$$

Since typically there is only a small number of reflectors in the channel with associated delays and Doppler shifts, very few parameters are often needed to model the channel in the delay–Doppler domain. Given the sparsity of the channel representation, it is convenient to express the response $h(\tau, \nu)$ in the form

$$h(\tau, \nu) = \sum_{i=1}^{P} h_i \delta(\tau - \tau_i) \delta(\nu - \nu_i) \tag{3.4}$$

where $\delta(\cdot)$ is the Dirac delta function, P is the number of propagation paths, and h_i, τ_i, and ν_i denote the complex path gain, delay, and Doppler shift (or frequency) associated with the i-th path, respectively. The delay and Doppler-shift taps for i-th path are given by

$$\tau_i = \frac{l_i}{M\Delta f}, \quad \nu_i = \frac{k_i}{NT} \tag{3.5}$$

For ease of derivations, we assume the delay and Doppler shifts as integer multiples of $\frac{1}{M\Delta f}$ and $\frac{1}{NT}$, respectively, i.e., we assume l_i, k_i are integers. However, fractional delay and Doppler shifts can also be handled using the techniques discussed in [16] by adding virtual integer taps in the delay–Doppler channel. Hence, the results derived in this work can be straightforwardly extend to the fractional delay and Doppler shifts.

Here, NT and $M\Delta f$ denote the total duration and bandwidth of the transmitted signal frame, respectively. Throughout the chapter, we have considered $T\Delta f = 1$, i.e., OTFS is critically sampled for all pulse-shaping waveforms. We assume that the maximum delay of the channel is $\tau_{\max} = (L-1)T/M$, i.e., $\max(l_i) = L - 1$. Moreover, $l_i < M$ and $k_i < N$ (i.e., the channel is underspread: for example, typical values of l_i and k_i in LTE channels are less than 10% of M and N, respectively). The received signal $y(t)$ is sampled at a rate $f_s = M\Delta f = M/T$ and, after discarding the CP, a vector $\mathbf{r} = \{r(n)\}_{n=0}^{MN-1}$ is formed, whose entries, from (3.3) and (3.4), are the samples

$$r(n) = \sum_{i=1}^{P} h_i e^{j2\pi \frac{k_i(n-l_i)}{MN}} s([n - l_i]_{MN}) + w(n) \tag{3.6}$$

where $[\cdot]_n$ denotes mod-n operation. We write (3.6) in vector form as

$$\mathbf{r} = \mathbf{H}\mathbf{s} + \mathbf{w}, \tag{3.7}$$

where $\mathbf{H}$ is the $MN \times MN$ matrix

$$\mathbf{H} = \sum_{i=1}^{P} h_i \mathbf{\Pi}^{l_i} \mathbf{\Delta}^{k_i}, \tag{3.8}$$

with $\mathbf{\Pi}$ the permutation matrix (forward cyclic shift),

$$\mathbf{\Pi} = \begin{bmatrix} 0 & \cdots & 0 & 1 \\ 1 & \ddots & 0 & 0 \\ \vdots & \ddots & \ddots & \vdots \\ 0 & \cdots & 1 & 0 \end{bmatrix}_{MN \times MN} \tag{3.9}$$

and $\mathbf{\Delta}$ is the $MN \times MN$ diagonal matrix

$$\mathbf{\Delta} = \mathrm{diag}\left[z^0, z^1, \cdots, z^{MN-1}\right] \tag{3.10}$$

with $z = e^{\frac{j2\pi}{MN}}$. Here, the matrices $\mathbf{\Pi}$ and $\mathbf{\Delta}$ model the delays and the Doppler shifts in (3.3), respectively. Each path introduces an l_i-step cyclic shift of the transmitted signal vector $\mathbf{s}$, modeled by $\mathbf{\Pi}^{l_i}$, and modulates it with a carrier at frequency k_i, modeled by $\mathbf{\Delta}^{k_i}$.

3.1.3 Receiver

At the receiver, we invert the transmitter operations to transform the received signal samples $\mathbf{r}$ into the time–frequency domain symbols $\mathbf{R} = \mathrm{vec}^{-1}(\mathbf{r})$ (the vector elements are folded back into a matrix), next into the delay–Doppler domain symbols $\mathbf{Y} = \mathbf{F}_M^{\mathrm{H}}(\mathbf{F}_M \mathbf{G}_{\mathrm{rx}} \mathbf{R})\mathbf{F}_N$. To do this, we apply an M-point FFT followed by an SFFT. Here, $\mathbf{G}_{\mathrm{rx}} \in \mathbb{C}^{M \times M}$ represents the filter operating at the receiver and using the pulse-shaping waveform $g_{\mathrm{rx}}(t)$. We can write $\mathbf{G}_{\mathrm{rx}} = \mathrm{diag}[g_{\mathrm{rx}}(0), g_{\mathrm{rx}}(T/M), \cdots, g_{\mathrm{rx}}((M-1)T/M)]$.

In vectorized form the received signal in the delay–Doppler domain can be written, after substituting (3.2) in (3.7), as

$$\mathbf{y} = (\mathbf{F}_N \otimes \mathbf{G}_{\mathrm{rx}})\mathbf{r}$$

$$= (\mathbf{F}_N \otimes \mathbf{G}_{\mathrm{rx}})\mathbf{H}(\mathbf{F}_N^{\mathrm{H}} \otimes \mathbf{G}_{\mathrm{tx}})\mathbf{x} + (\mathbf{F}_N \otimes \mathbf{G}_{\mathrm{rx}})\mathbf{w}$$

$$= \mathbf{H}_{\mathrm{eff}}\mathbf{x} + \widetilde{\mathbf{w}} \tag{3.11}$$

where $\mathbf{H}_{\mathrm{eff}} = (\mathbf{F}_N \otimes \mathbf{G}_{\mathrm{rx}})\mathbf{H}(\mathbf{F}_N^{\mathrm{H}} \otimes \mathbf{G}_{\mathrm{tx}})$ denotes the effective channel matrix, and $\widetilde{\mathbf{w}} = (\mathbf{F}_N \otimes \mathbf{G}_{\mathrm{rx}})\mathbf{w}$ the noise vector. It can be easily seen that in general $\widetilde{\mathbf{w}}$ has a diagonal covariance matrix, which becomes a scalar matrix (indicating iid noise samples) in the case of rectangular waveforms, i.e., $\mathbf{G}_{\mathrm{rx}} = \mathbf{I}_M$.

In the next section, we will simplify $\mathbf{H}_{\mathrm{eff}}$ to obtain a simple relation between the input and output symbols in delay–Doppler domain.

3.2 Input–Output Relation

In this section, we first derive the simplified form of $\mathbf{H}_{\mathrm{eff}}$ for the rectangular waveforms and then extend that relation to the arbitrary waveforms at the transmitter and receiver. For the rectangular waveforms, both $\mathbf{G}_{\mathrm{tx}}$ and $\mathbf{G}_{\mathrm{rx}}$ are equal to $\mathbf{I}_M$, and hence

$$\mathbf{H}_{\mathrm{eff}}^{\mathrm{rect}} = (\mathbf{F}_N \otimes \mathbf{I}_M)\mathbf{H}(\mathbf{F}_N^{\mathrm{H}} \otimes \mathbf{I}_M). \tag{3.12}$$

Let us first recall the following lemma on circulant matrices decomposition [40].

Lemma 3.1. *Let* $\mathbf{A} = circ[\mathbf{A}_0, \dots, \mathbf{A}_{N-1}]$ *denote the* $MN \times MN$ *block-circulant matrix*

$$\mathbf{A} = \begin{bmatrix} \mathbf{A}_0 & \mathbf{A}_{N-1} & \cdots & \mathbf{A}_1 \\ \mathbf{A}_1 & \mathbf{A}_0 & \cdots & \mathbf{A}_2 \\ \vdots & \ddots & \ddots & \vdots \\ \mathbf{A}_{N-1} & \mathbf{A}_{N-2} & \cdots & \mathbf{A}_0 \end{bmatrix} \tag{3.13}$$

where $\mathbf{A}_0, \cdots, \mathbf{A}_{N-1}$ *are square matrices of order* M. *Then* $\mathbf{A}$ *can be block-diagonalized in the following forms:*

$$\mathbf{A} = (\mathbf{F}_N^{\mathrm{H}} \otimes \mathbf{I}_M)\mathbf{D}(\mathbf{F}_N \otimes \mathbf{I}_M) \tag{3.14}$$

$$= (\mathbf{F}_N \otimes \mathbf{I}_M)\widetilde{\mathbf{D}}(\mathbf{F}_N^{\mathrm{H}} \otimes \mathbf{I}_M) \tag{3.15}$$

where $\mathbf{D}$ and $\widetilde{\mathbf{D}}$ are the block diagonal matrices

$$\mathbf{D} = diag\,[\mathbf{D}_0, \mathbf{D}_1, \cdots, \mathbf{D}_{N-1}] \tag{3.16}$$

$$\widetilde{\mathbf{D}} = diag\left[\widetilde{\mathbf{D}}_0, \widetilde{\mathbf{D}}_1, \cdots, \widetilde{\mathbf{D}}_{N-1}\right]$$

with block submatrices $\mathbf{D}_0, \cdots, \mathbf{D}_{N-1}, \widetilde{\mathbf{D}}_0, \cdots, \widetilde{\mathbf{D}}_{N-1} \in \mathbb{C}^{M \times M}$. The (i,j)-th entry $(0 \le i \le M-1,$ $0 \le j \le M-1)$ of $\mathbf{D}_n$ $(0 \le n \le N-1)$ can be computed as the nth element of the DFT of the vector $\mathbf{a}^{(i,j)} = [\mathbf{A}_0(i,j), \cdots, \mathbf{A}_{N-1}(i,j)]^T$, i.e.,

$$[\mathbf{D}_0(i,j), \cdots, \mathbf{D}_{N-1}(i,j)]^T = \sqrt{N}\mathbf{F}_N\mathbf{a}^{(i,j)} \tag{3.17}$$

Similar to $\mathbf{D}$, $\widetilde{\mathbf{D}}$ is related to $\mathbf{a}^{(i,j)}$ by

$$\left[\widetilde{\mathbf{D}}_0(i,j), \cdots, \widetilde{\mathbf{D}}_{N-1}(i,j)\right]^T = \sqrt{N}\mathbf{F}_N^{\mathrm{H}}\mathbf{a}^{(i,j)}.$$

The above can also be expressed in the form

$$\mathbf{a}^{(i,j)} = \frac{1}{\sqrt{N}}\mathbf{F}_N\left[\widetilde{\mathbf{D}}_0(i,j), \cdots, \widetilde{\mathbf{D}}_{N-1}(i,j)\right]^T \tag{3.18}$$

Proof: See [40] for the details. The proof of (3.17) is based on the fact that the $N \times N$ submatrices of $\mathbf{A}$ obtained by taking a row and a column every M are circulant. There are M^2 distinct such circulant submatrices. ∎

The following theorem yields a simplified form of $\mathbf{H}_{\mathrm{eff}}$.

Theorem 3.1. *The effective channel matrix $\mathbf{H}_{\mathrm{eff}}$ for rectangular waveforms can be written as*

$$\mathbf{H}_{\mathrm{eff}}^{rect} = \sum_{i=1}^{P} h_i \mathbf{T}^{(i)}, \tag{3.19}$$

where the entry (p, q), $0 \leq p \leq MN - 1, 0 \leq q \leq MN - 1$, *of* $\mathbf{T}^{(i)}$ *is*

$$\mathbf{T}^{(i)}(p, q) = \begin{cases} e^{-j2\pi \frac{n}{N}} z^{k_i([m-l_i]_M)}, & \text{if } q = [m - l_i]_M + M[n - k_i]_N \text{ and } m < l_i \\ z^{k_i([m-l_i]_M)}, & \text{if } q = [m - l_i]_M + M[n - k_i]_N \text{ and } m \geq l_i \\ 0, & \text{otherwise.} \end{cases} \quad (3.20)$$

In (3.20), the values of n *and* m *can be computed from* $p = (m, n)$ *using* $n = \lfloor \frac{p}{M} \rfloor$ *and* $m = p - nM$. *Notice that* $\mathbf{H}_{\text{eff}}^{rect}$ *has only* P *nonzero entries in each row and column. The row and column entries describe the effect of information symbols on a particular received signal.*

Proof: The proof is relegated to the Appendix B.1. ∎

Example: Let us consider $M = 2, N = 2$, and examine $\mathbf{T}^{(i)}$ in the following four channel cases.
1. $k_1 = 0, l_1 = 0$: In this case, $\mathbf{P}^{(1)}$ and $\mathbf{Q}^{(1)}$ becomes $\mathbf{I}_4$ that leads $\mathbf{T}^{(1)}$ to $\mathbf{I}_4$. That is, the channel with zero delay and Doppler corresponds to a narrowband channel in OTFS.
2. $k_2 = 0, l_2 = 1$: In this case, $\mathbf{Q}^{(2)}$ becomes $\mathbf{I}_4$ and

$$\mathbf{P}^{(2)} = \mathbf{T}^{(2)} = \begin{bmatrix} 0 & 1 & 0 & 0 \\ 1 & 0 & 0 & 0 \\ 0 & 0 & 0 & e^{-j2\pi\frac{1}{2}} \\ 0 & 0 & 1 & 0 \end{bmatrix}$$

That is, channel with one delay circularly shifts the elements in each column (delay dimension) of $\mathbf{s}$ with extra phase shifts.
3. $k_3 = 1, l_3 = 0$: In this case, $\mathbf{P}^{(3)}$ becomes $\mathbf{I}_4$ and

$$\mathbf{Q}^{(3)} = \mathbf{T}^{(3)} = \begin{bmatrix} 0 & 0 & 1 & 0 \\ 0 & 0 & 0 & e^{j2\pi\frac{1}{4}} \\ 1 & 0 & 0 & 0 \\ 0 & e^{j2\pi\frac{1}{4}} & 0 & 0 \end{bmatrix}$$

That is, channel with one Doppler circularly shifts the columns (Doppler dimension) of $\mathbf{s}$ with extra phase shifts.

4. $k_4 = 1, l_4 = 1$: In this case,

$$
\mathbf{T}^{(4)} =
\begin{bmatrix}
0 & 0 & 0 & e^{j2\pi\frac{1}{4}} \\
0 & 0 & 1 & 0 \\
0 & e^{-j2\pi\frac{1}{4}} & 0 & 0 \\
1 & 0 & 0 & 0
\end{bmatrix}
$$

That is, channel with both delay and Doppler circularly shifts the columns and elements in each column of $\mathbf{s}$.

Remark 3.1. *From Chapter 2, the input–output relation for the ideal waveforms case can be written as a 2D convolution in the form [17, 18]*

$$
\mathbf{Y}(m,n) = \sum_{i=1}^{P} h_i \mathbf{X}([m - l_i]_M, [n - k_i]_N) \tag{3.21}
$$

Therefore, the effective channel matrix in Theorem 1 can be obtained from (3.21) by replacing h_i with $h_i \alpha_i(m,n)$, where the correction factor is given by

$$
\alpha_i(m,n) =
\begin{cases}
e^{-j2\pi\frac{n}{N}} z^{k_i([m-l_i]_M)}, & \text{if } m < l_i \\
z^{k_i([m-l_i]_M)}, & \text{if } m \geq l_i \\
0, & \text{otherwise.}
\end{cases}
$$

The extra phase shifts, $\alpha_i(m,n)$, are caused by imperfect bi-orthogonality of the non-ideal waveforms. Note that sparsity of OTFS is not affected by the $\alpha_i(m,n)$'s, hence the complexity of any detection algorithm does not change, when practical waveforms are used.

Based on Theorem 1, we can provide a simplified input–output relation when the waveforms at the transmitter and receiver are arbitrary.
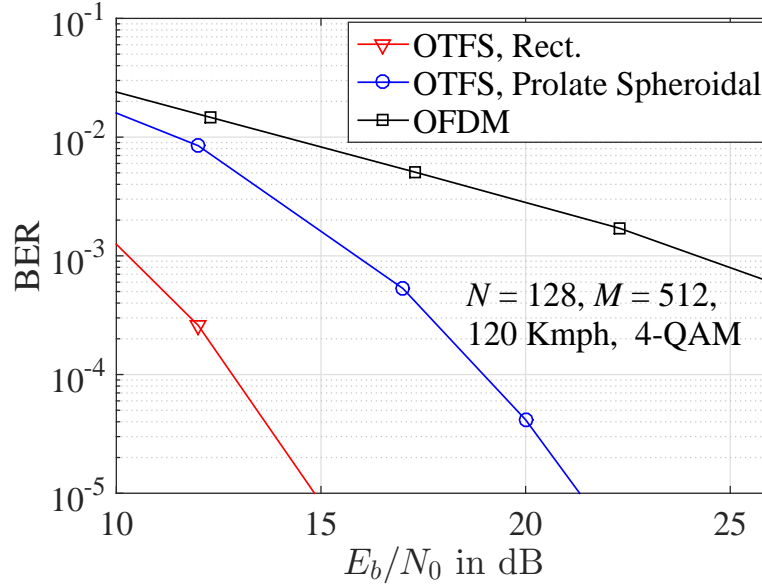
Figure 3.1: BER performance of OTFS system with rectangle and prolate spheroidal pulse shaping waveforms.

Theorem 3.2. *The effective channel matrix,* $\mathbf{H}_{\mathrm{eff}}$ *for the arbitrary waveforms can be written as*

$$\mathbf{H}_{\mathrm{eff}} = \sum_{i=1}^{P} h_i \left[(\mathbf{I}_N \otimes \mathbf{G}_{\mathrm{rx}}) \mathbf{T}^{(i)} (\mathbf{I}_N \otimes \mathbf{G}_{\mathrm{tx}}) \right], \tag{3.22}$$

Proof: The result can be obtained by writing $\mathbf{H}_{\mathrm{eff}}$ in (3.11) as

$$\mathbf{H}_{\mathrm{eff}} = (\mathbf{I}_N \otimes \mathbf{G}_{\mathrm{rx}})(\mathbf{F}_N \otimes \mathbf{I}_M)\mathbf{H}(\mathbf{F}_N^{\mathrm{H}} \otimes \mathbf{I}_M)(\mathbf{I}_N \otimes \mathbf{G}_{\mathrm{tx}})$$

$$= (\mathbf{I}_N \otimes \mathbf{G}_{\mathrm{rx}})\mathbf{H}_{\mathrm{eff}}^{\mathrm{rect}}(\mathbf{I}_N \otimes \mathbf{G}_{\mathrm{tx}})$$

$$= (\mathbf{I}_N \otimes \mathbf{G}_{\mathrm{rx}}) \left[\sum_{i=1}^{P} h_i \mathbf{T}^{(i)} \right] (\mathbf{I}_N \otimes \mathbf{G}_{\mathrm{tx}}) \tag{3.23}$$

Moreover, $\mathbf{H}_{\mathrm{eff}}$ has also exactly P nonzero elements in each row as $(\mathbf{I}_N \otimes \mathbf{G}_{\mathrm{rx}})$ and $(\mathbf{I}_N \otimes \mathbf{G}_{\mathrm{tx}})$ are diagonal matrices. ∎

3.2.1   A Special Case: Prolate Spheroidal Waveforms

Assume $g_{\mathrm{tx}}(t)$ to be a prolate spheroidal waveform (PSW) [41]: this has a much lower out-of-band power than the rectangular waveform, which reduces the out-of-band interference of OFDM systems. It can be easily shown that an arbitrary $g_{\mathrm{rx}}(t)$ does not affect the performance of maximum

likelihood (ML) detection, since both signal and noise components are equally scaled. Therefore, we have selected a rectangular $g_{\mathrm{rx}}(t)$.

Fig. 3.1 shows BER of OTFS vs. E_b/N_0 with rectangular and PSW. This figure also compares OTFS with CP-OFDM as a function of E_b/N_0, where E_b/N_0 takes into account the rate loss of CP-OFDM due to the use of CP overhead. The plot corresponds to the following parameters: carrier frequency = 4 GHz, subcarrier spacing = 15 KHz, $M = 512$, $N = 128$, maximum speed = 120 Kmph, and 4-QAM modulation. We use EVA model [35] for the channel delay, and each delay tap has a single Doppler shift generated using Jakes' formula $\nu_i = \nu_{\max} \cos(\theta_i)$, where $\nu_{\max}$ is the maximum Doppler shift determined by the UE speed and θ_i is uniformly distributed over $[-\pi, \pi]$. For the detection of transmit symbols, we use the message-passing detector proposed in the Chapter 2. Note that both waveforms have similar detection complexity, as the sparsity of the effective channel matrix is same.

We can see from the figure that rectangular waveforms outperform by about 5 dB the PSW. This is due to the structure of the latter: here, some of the symbols (edge symbols, see (3.23)) experience lower channel gains, which degrades the overall performance, while with rectangular waveforms all symbols experience uniform channel gains. Hence, we see a trade-off between out-of-band power and error performance of the OTFS system. Moreover, OTFS with PSW can still be able to outperform OFDM in terms of diversity gain (the BER curve slope).

Chapter 4

Embedded Pilot-Aided Channel Estimation for OTFS

In order to implement the OTFS detection methods proposed in the earlier chapters, the delay–Doppler channel impulse response needs to be known at the receiver. In this chapter, we propose embedded pilot-aided channel estimation schemes for OTFS. In each OTFS frame, we arrange pilot, guard, and data symbols in the delay–Doppler plane to suitably avoid interference between pilot and data symbols at the receiver. We develop such symbol arrangements for OTFS over multipath channels with integer and fractional Doppler shifts respectively. At the receiver, channel estimation is performed based on a threshold method and the estimated channel information is used for data detection via a MP algorithm. As a result of our specific embedded symbol arrangements, both channel estimation and data detection are performed within the same OTFS frame with a minimum overhead. We compare by simulations the error performance of OTFS using the proposed channel estimation algorithm and OTFS with ideally known channel information and observe only a marginal performance loss. We also demonstrate that the proposed channel estimation in OTFS significantly outperforms OFDM with ideal channel information.

The rest of the chapter is organized as follows. Section 4.1 reviews the basic OTFS results derived in Chapter 2, which lay the foundations for the development of OTFS-specific channel estimation schemes in Section 4.2 and 4.3. Numerical results are presented in Section 4.4.

Part of the content of this chapter appears as, P. Raviteja, K. T. Phan, Y. Hong, and E. Viterbo, "Embedded delay-Doppler channel estimation for orthogonal time frequency space modulation," in *Proc. IEEE 88th Vehicular Technology Conference: VTC2018-Fall*, Chicago, USA, August 2018.

4.1 OTFS Overview

In this section, we recollect the OTFS input–output relations derived in the Chapter 2 for the ideal waveforms.

4.1.1 Integer Doppler Shifts (i.e., $\kappa_{\nu_i} = 0$, for all i)

The relation between $y[k,l]$ and $x[k,l]$ with the ideal waveforms for integer Doppler case can be written as

$$y[k,l] = \sum_{k_i=-k_\nu}^{k_\nu} \sum_{l_i=0}^{l_\tau} b[k_i,l_i]\hat{h}[k_i,l_i]x[[k-k_i]_N,[l-l_i]_M] + v[k,l] \tag{4.1}$$

where $\hat{h}[k_i,l_i] = h_i e^{-j2\pi \frac{k_i}{NT}\frac{l_i}{M\Delta f}}$; $b[k_i,l_i] \in \{0,1\}$ is path indicator: $b[k_i,l_i] = 1$ means that there is a path with Doppler tap k_i and delay tap l_i with corresponding (modified) path magnitude $\hat{h}[k_i,l_i]$, otherwise, there is no such path, i.e., $b[k_i,l_i] = \hat{h}[k_i,l_i] = 0$; $v[k,l] \sim \mathcal{CN}(0,\sigma^2)$ is additive white noise with variance σ^2, $[\cdot]_N$ and $[\cdot]_M$ denote modulo N and M operations, respectively. We have the total number of paths:

$$\sum_{k_i=-k_\nu}^{k_\nu} \sum_{l_i=0}^{l_\tau} b[k_i,l_i] = P.$$

Each path circularly shifts the transmitted signal by the delay and Doppler taps and scales it by the associated path gain.

4.1.2 Fractional Doppler Shifts

Similarly, the input–output relation for the fractional Doppler case can be written as

$$y[k,l] = \sum_{k_i=-k_\nu}^{k_\nu} \sum_{l_i=0}^{l_\tau} b[k_i,l_i] \sum_{q=-N/2}^{N/2-1} \bar{h}(k_i,l_i,\kappa_i,q)x\left[[k-k_i+q]_N,[l-l_i]_M\right] + v[k,l] \tag{4.2}$$

where $\bar{h}(k_i,l_i,\kappa_i,q) = \left(\frac{e^{j2\pi(-q-\kappa_i)}-1}{Ne^{j\frac{2\pi}{N}(-q-\kappa_i)}-N} \right) h_i e^{-j2\pi \frac{k_i+\kappa_i}{NT}\frac{l_i}{M\Delta f}}$. It can be seen that with fractional Doppler shifts, each received symbol is affected by more neighboring symbols than in the case of integer Doppler.

(a) Tx symbol arrangement ($\square$: pilot; $\circ$: guard symbols; $\times$: data symbols)

(b) Rx symbol pattern ($\triangledown$: data detection, $\boxplus$: channel estimation)
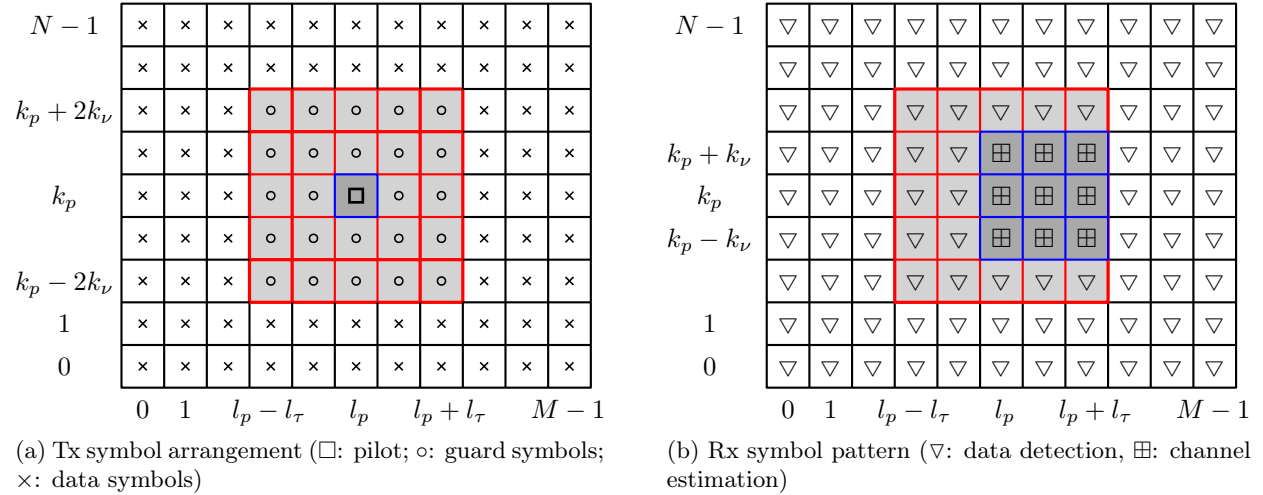
Figure 4.1: Tx pilot, guard, and data symbols and Rx received symbols

4.1.3 OTFS Data Detection via Message Passing (MP)

From the received symbols $y[k, l]$, if the channel parameters h_i, τ_i, and ν_i (and hence, the corresponding taps l_{τ_i}, k_{ν_i}, and κ_{ν_i}) are known, we can employ the MP algorithm to detect the data symbols $x[k, l]$ using the set of MN linear equations (4.1) or (4.2).

We first assume OTFS with ideal waveforms for multipath channel with integer and fractional Doppler cases. Then we consider the extension to OTFS with practical rectangular waveforms.

4.2 Embedded Channel Estimation: The Integer Doppler Case

Let x_p denote the pilot symbol with pilot SNR of $\mathrm{SNR}_p = |x_p|^2/\sigma^2$, $x_d[k, l]$ denote the data symbols with data SNR of $\mathrm{SNR}_d = \mathbb{E}(|x_d|^2)/\sigma^2$, located at location $[k, l]$ in the delay–Doppler information grid, and 0 denotes the guard symbol.

Motivated by [44], we place one pilot symbol x_p, N_n of the guard symbols, and $MN - N_n - 1$ information symbols in the delay–Doppler grid Γ for each OTFS frame transmission. The symbols are located in such a way so that at the receiver, we can separate two distinct groups of received symbols: the first group that involves pilot and guard symbols is used for channel estimation, and the second group for data detection. Moreover, the guard symbols guarantee that the received symbols for channel estimation and data detection are not interfered with each other. This helps to provide a more accurate channel estimation to be used for data detection within the same frame.

For a pilot, we first choose arbitrary grid location $[k_p, l_p]$ such that $0 \leq k_p \leq N - 1$, and $0 \leq l_p \leq M - 1$. For ease of representation, we choose $0 \leq l_p - l_\tau \leq l_p \leq l_p + l_\tau \leq M - 1$, and $0 \leq k_p - 2k_\nu \leq k_p \leq k_p + 2k_\nu \leq N - 1$. Recall that l_τ and k_ν denote the taps corresponding to the maximum delay and Doppler values.

We arrange the pilot, guard, and data symbols in the delay–Doppler grid for an OTFS frame transmission as in Fig. 4.1a:

$$
x[k, l] = \begin{cases} x_p & k = k_p, l = l_p, \\ 0 & k_p - 2k_\nu \leq k \leq k_p + 2k_\nu, l_p - l_\tau \leq l \leq l_p + l_\tau, \\ x_d[k, l] & \text{otherwise.} \end{cases} \tag{4.3}
$$

In this case, we have $N_n = (2l_\tau + 1)(4k_\nu + 1) - 1$ guard symbols. For example, in LTE channels, the overhead for pilot and guard symbols is less than 1% of the data frame [45].

At the receiver, we use the received symbols $y[k, l]$, $k_p - k_\nu \leq k \leq k_p + k_\nu, l_p \leq l \leq l_p + l_\tau$ for channel estimation. Then the remaining received symbols $y[k, l]$ on the grid are used for data detection, as shown in Fig. 4.1b.

Due to the transmit symbol arrangement in (4.3), using (4.1), we can express the received symbols for channel estimation as

$$
y[k, l] = b[k - k_p, l - l_p]\hat{h}[k - k_p, l - l_p]x_p + v[k, l]. \tag{4.4}
$$

for $k \in [k_p - k_\nu, k_p + k_\nu], l \in [l_p, l_p + l_\tau]$. We can see that if there is a path with Doppler tap $k - k_p$ and delay tap $l - l_p$, i.e., $b[k - k_p, l - l_p] = 1$, we have $y[k, l] = \hat{h}[k - k_p, l - l_p]x_p + v[k, l]$. Otherwise, $y[k, l] = v[k, l]$.

Similarly, we can express the received symbols for data detection as in (4.1), demonstrating no interference between the received symbols for channel estimation and data detection.

We propose a simple channel estimation algorithm as follows. For $k \in [k_p - k_\nu, k_p + k_\nu], l \in [l_p, l_p + l_\tau]$, if the magnitude $|y[k, l]| \geq \mathcal{T}$, where $\mathcal{T}$ is some positive detection threshold, then we estimate $b[k - k_p, l - l_p] = 1$ and $\hat{h}[k - k_p, l - l_p] = y[k, l]/x_p$. Otherwise, we set $b[k - k_p, l - l_p] = \hat{h}[k - k_p, l - l_p] = 0$. The proposed threshold-based scheme relies on the fact that if a path exists, the

received symbol is the scaled pilot signal with additive white Gaussian noise (see (4.4)). Otherwise, it is only noise.

By varying the threshold $\mathcal{T}$, we can alter the miss detection or false alarm probabilities on path detection. As a result, the error performance of data detection is affected by $\mathcal{T}$, as will be shown in Section 4.4.

We then use the estimated information for data detection, i.e., the received symbols $y[k,l]$ for data detection are

$$y[k,l] = \sum_{k'=-k_\nu}^{k_\nu} \sum_{l'=0}^{l_\tau} b[k',l']\hat{h}[k',l']x_d[[k-k']_N,[l-l']_M] + v[k,l] \tag{4.5}$$

for $k \notin [k_p - k_\nu, k_p + k_\nu]$ or $l \notin [l_p, l_p + l_\tau]$. Note that we have a total of $MN - (2k_\nu + 1)(l_\tau + 1)$ received symbols to detect a smaller number of $MN - (2l_\tau + 1)(4k_\nu + 1)$ data symbols via the MP algorithm.

4.3   Embedded Channel Estimation: The Fractional Doppler Case

We consider two cases using full guard symbols and reduced guard symbols, respectively. The former case offers better channel estimation at the expense of the lower spectral efficiency by using more guard symbols and less data symbols, in contrast to the latter case.

4.3.1   The Case With Full Guard Symbols

We arrange the pilot, guard, and data symbols in the delay–Doppler grid, as depicted in Fig. 4.2a:

$$x[k,l] = \begin{cases} x_p, & k = k_p, l = l_p \\ 0, & 0 \le k \le N-1, l_p - l_\tau \le l \le l_p + l_\tau \\ x_d[k,l], & \text{otherwise.} \end{cases} \tag{4.6}$$

For simplicity of notation, we choose $0 \le l_p - l_\tau \le l_p \le l_p + l_\tau \le M - 1$. We have the number of guard symbols $N_n = (2l_\tau + 1)N - 1$, and the overhead for pilot and guard symbols is about 8% in LTE channels [45].

At the receiver, we use the received symbols $y[k,l], 0 \le k \le N - 1, l_p \le l \le l_p + l_\tau$ for channel

(a) Tx symbol arrangement ($\square$: pilot; $\circ$: guard symbols; $\times$: data symbols)

(b) Rx symbol pattern ($\triangledown$: data detection, $\boxplus$: channel estimation)
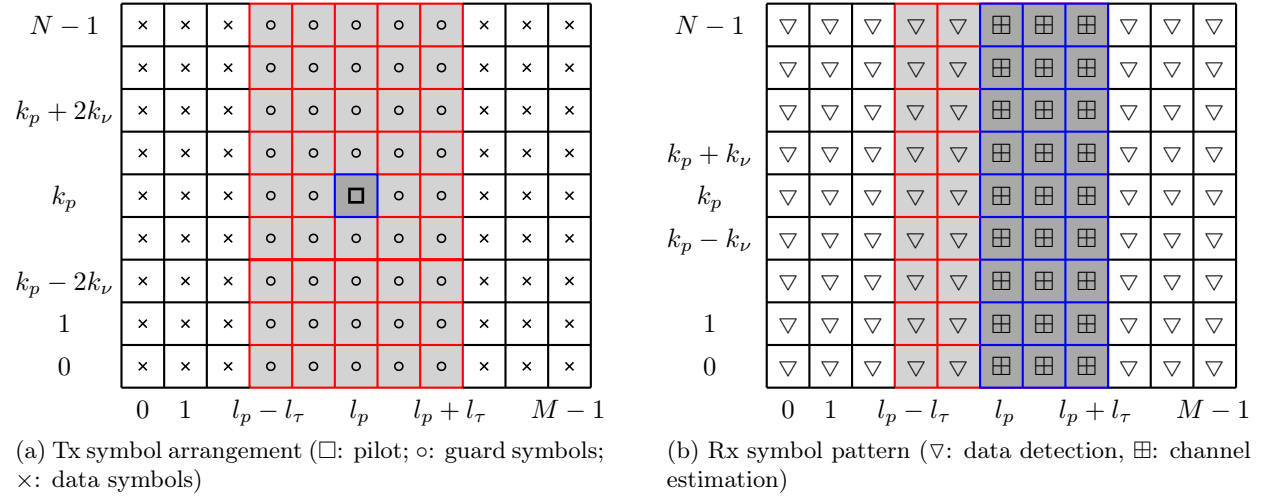
Figure 4.2: The fractional Doppler case: Full guard symbols

estimation, and the remaining received symbols $y[k,l]$ for data detection (see Fig. 4.2b).

Using (4.2), the received symbols $y[k,l]$ for channel estimation are

$$y[k,l] = \sum_{k'=-k_\nu}^{k_\nu} b[k',l-l_p]\bar{h}[k',l-l_p,\kappa',[k_p+k'-k]_N]x_p + v[k,l] \tag{4.7}$$

for $k \in [0, N-1], l \in [l_p, l_p + l_\tau]$. We can rewrite $y[k,l]$ as

$$y[k,l] = \tilde{b}[l-l_p]\tilde{h}[[k-k_p]_N, l-l_p]x_p + v[k,l] \tag{4.8}$$

where

$$\tilde{b}[l-l_p] = \begin{cases} 1, & \sum_{k'=-k_\nu}^{k_\nu} b[k',l-l_p] \geq 1 \\ 0, & \text{otherwise} \end{cases}$$

is the path indicator, and

$$\tilde{h}[[k-k_p]_N, l-l_p] = \sum_{k'=-k_\nu}^{k_\nu} b[k',l-l_p]\bar{h}[k',l-l_p,\kappa',[k_p+k'-k]_N]$$

is the effective path gain from the pilot symbol x_p at location $[k_p, l_p]$ to the received symbol $y[k,l]$. Then $\tilde{b}[l-l_p] = 1$ indicates that there is at least one path with delay tap $l-l_p$, otherwise, $\tilde{b}[l-l_p] = 0$.

(a) Tx symbol arrangement ($\square$: pilot; $\circ$: guard symbols; $\times$: data symbols)

(b) Rx symbol pattern ($\triangledown$: data detection, $\boxplus$: channel estimation)
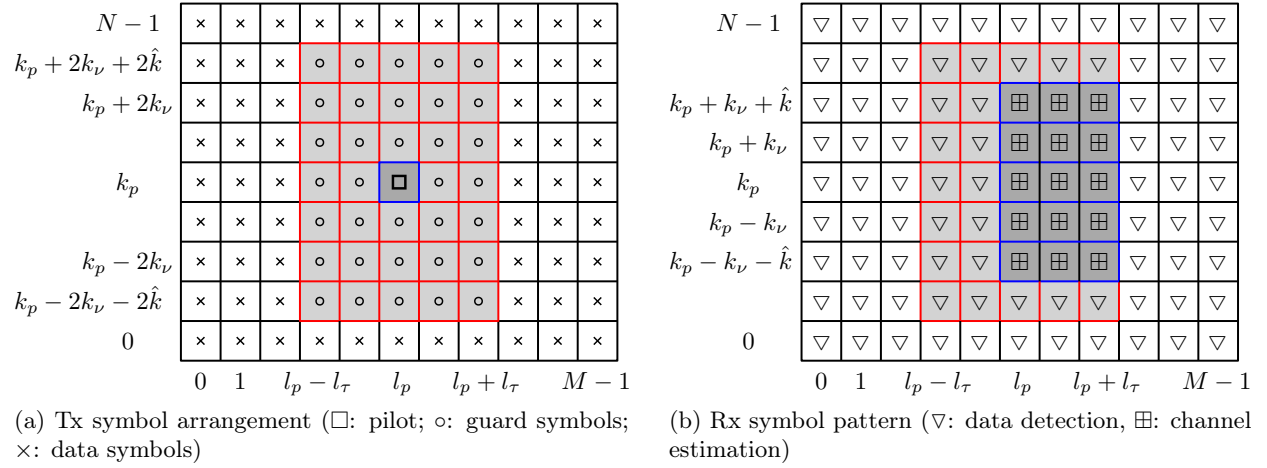
Figure 4.3: The fractional Doppler case: Reduced guard symbols

Based on (4.8), we propose the following threshold-based channel estimation algorithm.

For $k \in [0, N-1], l \in [l_p, l_p+l_\tau]$, if $|y[k,l]| \geq \mathcal{T}$, then we have $\tilde{b}[l-l_p] = 1$, and $\tilde{h}[[k-k_p]_N, l-l_p] = y[k,l]/x_p$. Otherwise, we set $\tilde{b}[l-l_p] = \tilde{h}[[k-k_p]_N, l-l_p] = 0$. Unlike the integer Doppler case, where we estimate whether an individual path with given delay and Doppler taps exists, in this case, we estimate whether there exists *at least* one path with a given delay tap.

For data detection, similar to (4.8), we rewrite (4.2) as

$$y[k,l] = \sum_{l'=0}^{l_\tau} \tilde{b}[l'] \sum_{k'=0}^{N-1} \tilde{h}[k',l']x_d[[k-k_{i'}]_N, [l-l']_M] + v[k,l] \tag{4.9}$$

for $k \in [0, N-1]$ and $l \notin [l_p, l_p + l_\tau]$. Now we can adapt the MP algorithm for data detection in (4.9).

Note that, to guarantee no interference between the received symbols for channel estimation and data detection, the guard symbols need to expand over a wider range over the Doppler axis, when compared to the integer Doppler case.

4.3.2 The Case of Reduced Guard Symbols

Employing full guard symbols to avoid interference provide more accurate channel estimation but with reduced spectral efficiency. To improve the spectral efficiency, we can reduce the number of guard symbols and thus increase the number of data symbols, as discussed below.

We arrange the symbols as in Fig. 4.3a

$$
x[k,l] = \begin{cases} x_p & k = k_p, l = l_p, \\ 0 & k_p - 2k_\nu - 2\hat{k} \le k \le k_p + 2k_\nu + 2\hat{k}, l_p - l_\tau \le l \le l_p + l_\tau, \\ x_d[k,l] & \text{otherwise} \end{cases}
$$

for some integer $\hat{k}$. We can see that as the value of $\hat{k}$ reduces, the required number of guard symbols reduces, resulting in an increased spectral efficiency.

The received symbols $y[k,l]$, $k_p - k_\nu - \hat{k} \le k \le k_p + k_\nu + \hat{k}, l_p \le l \le l_p + l_\tau$ are used for channel estimation, while the remaining $y[k,l]$ are used for data detection (see Fig. 4.3b)

From (4.2), for channel estimation, we have

$$
y[k,l] = \tilde{b}[l - l_p]\tilde{h}[[k - k_p]_N, l - l_p]x_p + \mathcal{I}[k,l] + v[k,l] \tag{4.10}
$$

for $k_p - k_\nu - \hat{k} \le k \le k_p + k_\nu + \hat{k}, l_p \le l \le l_p + l_\tau$. The second term $\mathcal{I}[k,l]$ is the interference from all neighboring data symbols $x_d[k,l]$, i.e.,

$$
\mathcal{I}[k,l] = \sum_{k'=-k_\nu}^{k_\nu} \sum_{l'=0}^{l_\tau} b[k',l'] \sum_{q \notin [k_p - 2k_\nu - 2\hat{k}, k_p + 2k_\nu + 2\hat{k}]} \bar{h}[k',l',\kappa',q]x_d\left[[k - k' + q]_N, [l - l']_M\right] \tag{4.11}
$$

We observe that the interference $\mathcal{I}[k,l]$ gets larger for smaller $\hat{k}$, and similarly for the interference from pilot symbols to the received symbols for data detection.

Similar to the case of full guard symbols, we develop a threshold-based algorithm to estimate $\tilde{b}[l - l_p]$ and $\tilde{h}[[k - k_p]_N, l - l_p]$ based on (4.10) by treating $\mathcal{I}[k,l]$ as additive noise. Based on the simulation results (see next section), we demonstrate that the performance gap of the full guard symbols case (8% overhead) and reduced guard symbols case (2% overhead) is indeed marginal.

4.3.3 OTFS With Rectangular Waveforms

So far, we have assumed ideal transmit $g_{\text{tx}}(t)$ and receive $g_{\text{rx}}(t)$ pulses. Since the ideal pulses cannot be realized in practice, we now investigate OTFS with the more practical rectangular pulses at both transmitter and receiver. Although these pulses do not satisfy the bi-orthogonality conditions, we

show that the proposed embedded channel estimation schemes can also be employed for this case.

Consider the integer Doppler case for simplicity. With rectangular pulses, the input-output symbol relationship can be rewritten from Chapters 2 and 3 as

$$y[k,l] = \sum_{k'=-k_\nu}^{k_\nu} \sum_{l'=0}^{l_\tau} b[k',l'] \hat{h}[k',l'] \beta[k,l] x[[k-k']_N, [l-l']_M] + v[k,l]$$

where

$$\beta[k,l] = \begin{cases} e^{j2\pi\left(\frac{l-l'}{M}\right)\frac{k'}{N}} & l' \le l < M \\ \frac{N-1}{N} e^{j2\pi\left(\frac{l-l'}{M}\right)\frac{k'}{N}} e^{-j2\pi\left(\frac{[k-k']_N}{N}\right)} & 0 \le l < l'. \end{cases}$$

Hence, the threshold-based channel estimation technique can be straightforwardly employed by introducing a known phase $\beta[k,l]$ in the detection process. The thresholds for the rectangular waveforms remain the same as the ideal waveforms, since the channel differs only by a phase.

4.4 Numerical Results

We illustrate the performance in terms of BER of the uncoded OTFS using the proposed channel estimation schemes for integer and fractional Doppler cases. We adopt the following system parameters: Carrier frequency of 4 GHz, sub-carrier spacing of 15 KHz, $M = 512$, $N = 128$, and $4-$QAM signaling. We denote $\text{SNR}_p = |x_p|^2/\sigma^2$ and $\text{SNR}_d = \mathbb{E}(|x_d|^2)/\sigma^2$ to represent the average pilot and data SNRs, respectively. We use $\sigma_p^2 = 1/\text{SNR}_p$ to denote the effective noise power of the pilot signal. For simplicity, we assume $\sigma^2 = 1$ in all the simulations. For both OTFS and OFDM systems, EVA model [35] is used, and each delay tap has a single Doppler shift generated by using Jakes' formula, i.e., $\nu_i = \nu_{\max} \cos(\theta_i)$, where $\nu_{\max}$ is the maximum Doppler shift determined by the UE speed and θ_i is uniformly distributed over $[-\pi, \pi]$.

4.4.1 The Integer Doppler Case

Fig. 4.4 compares BER versus data SNRs (SNR_d) for OTFS with known channel information (ideal case) and OTFS using the proposed channel estimation for the integer Doppler case with $\text{SNR}_p = 30$, 35, and 40 dB and $\mathcal{T} = 3\sigma_p$. We assume a delay–Doppler channel with maximum delay
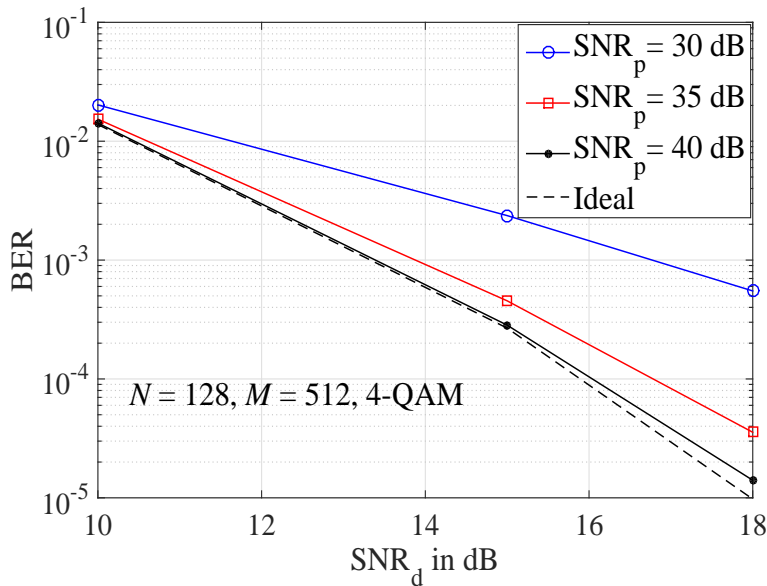
Figure 4.4: BER versus SNR_d: Integer Doppler case.

tap $l_\tau = 20$ and Doppler tap $k_\nu = 4$, which corresponds to maximum Doppler speed of 120 Kmph. The overhead for pilot and guard symbols is approximately 1% of an OTFS frame. We observe that the BER reduces as SNR_p increases, providing more accurate channel estimation and better data detection. Moreover, the performance of OTFS with channel estimation is very close to the ideal case, when $\text{SNR}_p = 40$ dB (at least 20dB higher than the data SNR_d). Note that a large pilot power does not affect the peak transmit power as OTFS spreads each delay–Doppler symbol in the entire time–frequency plane thanks to the ISFFT operation.

In Fig. 4.5, we perform comparisons of BER versus SNR_d for different Doppler frequencies with $\text{SNR}_p = 40$ dB, $l_\tau = 20$, $\mathcal{T} = 3\sigma_p$, and 4-QAM. Consider UE speeds of 30, 120, and 500 Kmph corresponding to maximum Doppler tap $k_\nu = 1, 4$, and 16, respectively. From the Fig. 4.5, we observe that the proposed estimation scheme exhibits highly similar performance under different Doppler frequencies except a slight performance improvement under higher Doppler frequencies (i.e., $k_\nu = 16$). This is due to the fact that more guard symbols and less data symbols are transmitted at high Doppler frequencies, leading to better data detection capability at higher SNR_d. Since OTFS performs similarly at different frequencies, in the following, we consider only the UE speed of 120 kmph.

We next investigate the effect of the channel estimation threshold $\mathcal{T}$ on the system performance.
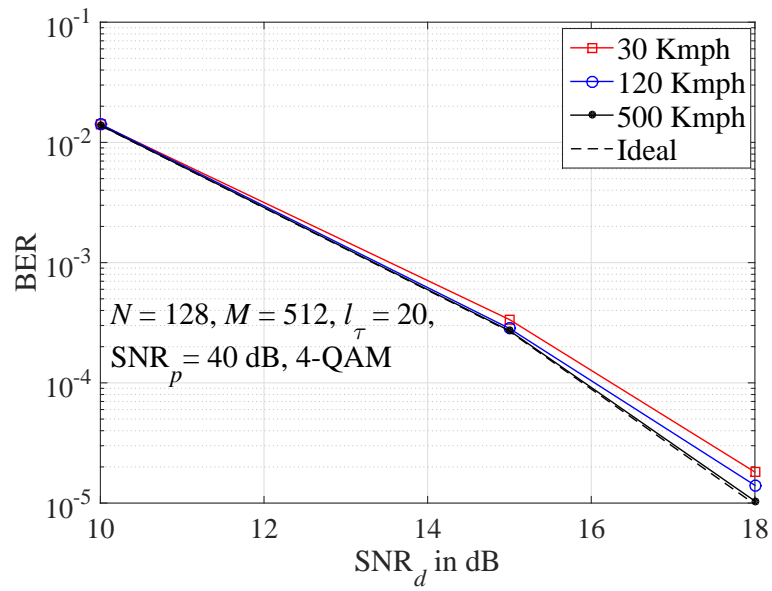
Figure 4.5: BER versus SNR_d for different Dopplers
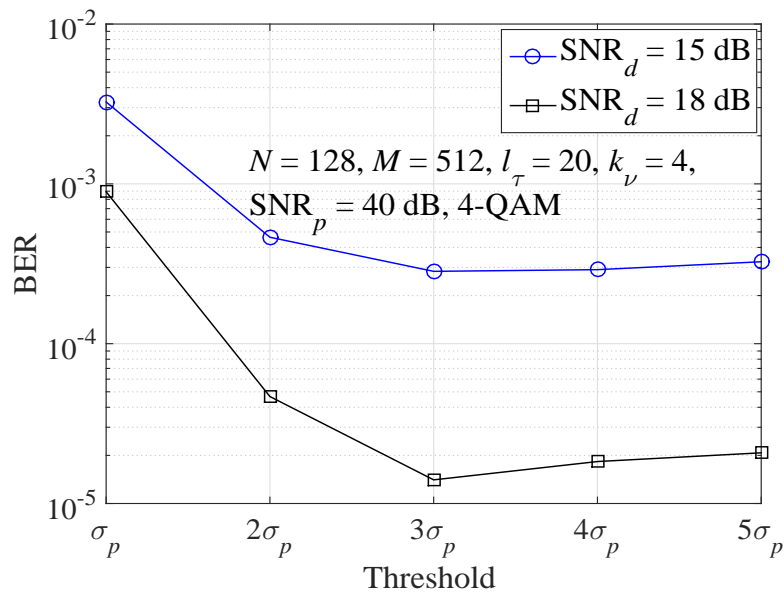
Figure 4.6: BER versus channel estimation thresholds: Integer Doppler case.
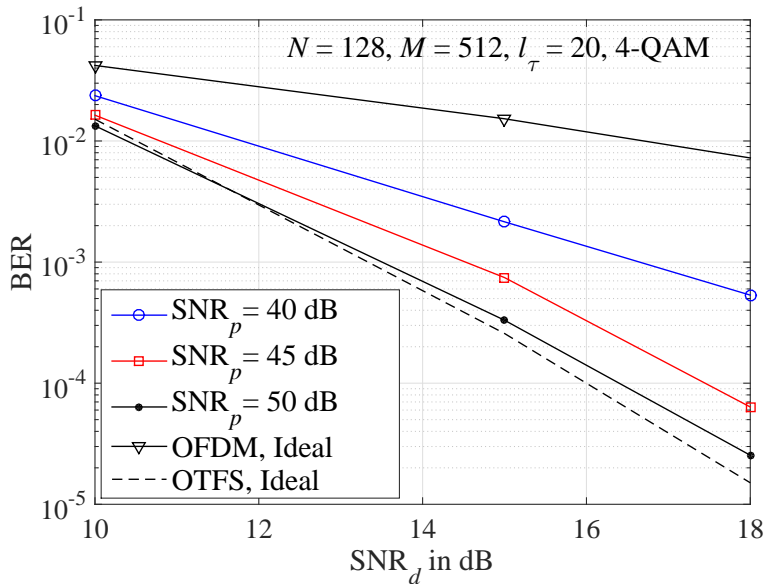
Figure 4.7: BER versus SNR_d: Fractional Doppler with full guard symbols.

Fix $\text{SNR}_p = 40$ dB. Fig. 4.6 displays BER versus SNR_d with different $\mathcal{T}$. We observe that the BER performance improves as $\mathcal{T}$ increases. For small threshold values, the path false detection probability is higher (i.e., it is more likely to detect non-existent paths), which degrades the BER performance. However, at the same time, increasing the threshold beyond a certain value may cause the likely miss detection of paths with small path-gains, resulting in performance loss. Hence, there is an optimal threshold to balance the false detection and miss detection probabilities. For the given system parameters, we observe that the optimal threshold is approximately 3σ.

4.4.2 The Fractional Doppler Case

Fig. 4.7 shows the BER for different SNR_p with a threshold of $\mathcal{T} = 3\sigma_p$. In this case, the pilot and guard symbols occupy approximately 8% of an OTFS frame. Similar to the integer Doppler case, as the pilot power is increased, the error performance is improved. As $\text{SNR}_p = 50$ dB, OTFS with our proposed embedded channel estimation attains similar performance as OTFS with known channel information. We can see that a larger pilot power is required for channels with fractional Doppler shifts than integer Doppler shifts. Last, we compare the BERs of OTFS with channel estimation and OFDM with known channel information and find that OTFS significantly outperforms OFDM, demonstrating the effectiveness of OTFS over delay–Doppler channels.
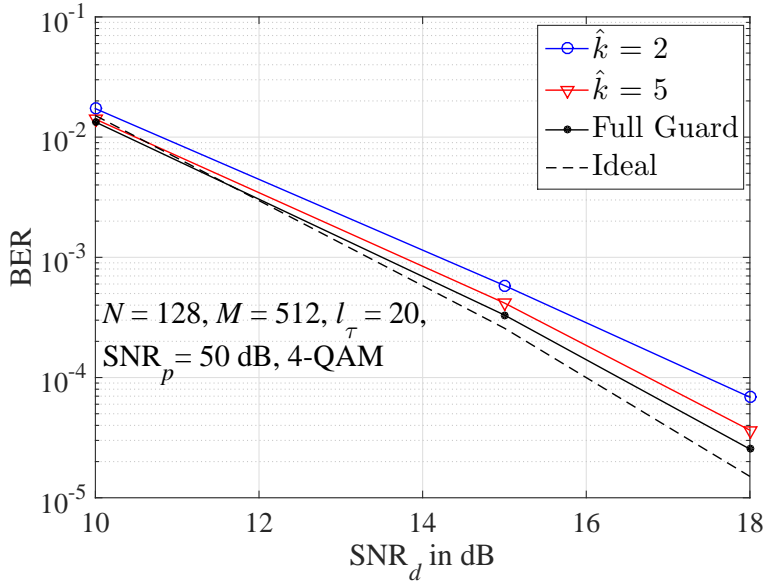
Figure 4.8: BER versus SNR_d: Fractional Doppler with reduced guard symbols.

In Fig. 4.8, we compare the BER performance of OTFS using the proposed channel estimation scheme with reduced guard symbols for $\hat{k} = 2$ and 5. Fix $\text{SNR}_p = 50$ dB, $\mathcal{T} = 3\sigma_p$, and 4-QAM. With $\hat{k} = 2$, and 5, the overheads for pilot and guard symbols are roughly 1.5% and 2.3%, respectively, which are much less than the full guard symbols case (roughly 8%). We observe that, as $\hat{k}$ becomes larger, the performance improves. In particular, with $\hat{k} = 5$, the performance is very close to that with full guard symbols. For larger $\hat{k}$, smaller interference from neighboring data symbols improves the channel estimation accuracy. Hence, there is a tradeoff between spectral efficiency and error performance.

In Fig. 4.9, we illustrate the effectiveness of the proposed channel estimation scheme with full and reduced guard symbols, respectively, using 16-QAM, $\text{SNR}_p = 60$ dB, and $\mathcal{T} = 3\sigma_p$. We see that with the higher pilot power (i.e., 60 dB), the performance of our channel estimation scheme with full guard symbols is the same as that of the ideal case. Moreover, with 16-QAM, a larger number of guard symbols are required (i.e., $\hat{k} = 10$, about 3.6% guard symbols overhead) to achieve a performance close to the full guard symbols case, when compared to the 4-QAM case that adopts $\hat{k} = 5$, about 2.3% guard symbols overhead. This is due to the fact that the data detection of 16-QAM case is more sensitive to the channel estimation and hence requires more guard symbols.
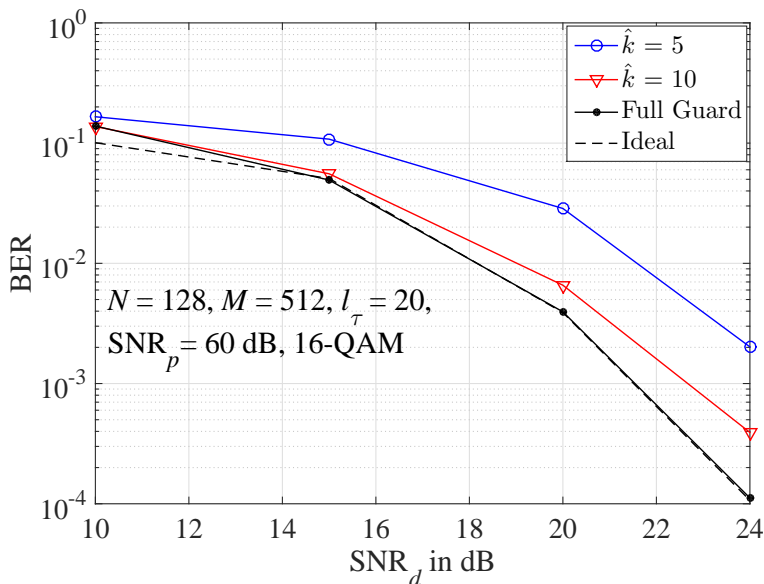
Figure 4.9: BER versus SNR_d: Fractional Doppler with reduced guard symbols for 16-QAM.

4.4.3   OTFS Under Low Latency Communications

As next-generation wireless communications mostly require low latency communications, we next simulate the proposed OTFS channel estimation schemes under such scenario. Fig. 4.10 shows the OTFS performance for low latency application with $N = 16$ and $M = 128$, corresponding to frame duration of 1.1 ms. We consider a UE speed of 120 Kmph, corresponding to a maximum Doppler tap, $k_\nu = 1$. We consider the channel estimation scheme with full guard symbols as the reduced guard symbols case will not improve significantly the spectral efficiency with small N. We observe that the OTFS performance with channel estimation is very close to the ideal case with $\text{SNR}_p = 60$ dB. Hence, we can conclude that the proposed channel estimation schemes are very efficient under low latency communications.
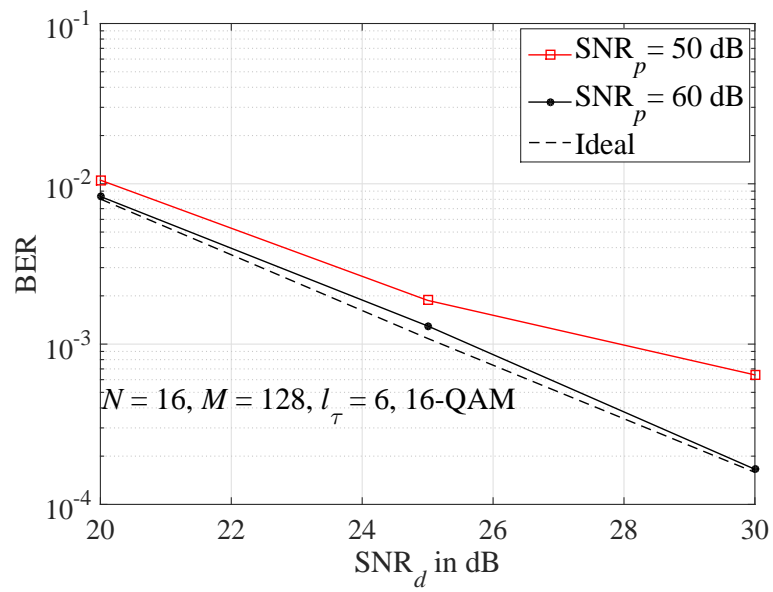
Figure 4.10: BER versus SNR_d: low latency communication

Chapter 5

OTFS Performance on Static Multipath Channels

Even though OTFS has been originally proposed for the highly time-variant channels, it's system architecture can also be suitable for time-invariant channels. In this chapter, we explore the performance of OTFS on time-invariant multipath channels and show that it still outperforms OFDM. We show that, in static multipath channels, the system structure of OTFS is equivalent to the A-OFDM [46], bridging between CPSC and traditional OFDM. We derive a condition on the parameters of OTFS to guarantee that all the transmitted symbols experience uniform channel gains, as in CPSC. Finally, we apply a low-complexity MP detection to OTFS/A-OFDM and show a significant performance improvement over ZF and MMSE detection originally proposed for A-OFDM.

The rest of the chapter is organized as follows. Section 5.1 presents the OTFS system model in static channels and establishes a relation with A-OFDM. In Section 5.2, we derive a condition to optimize the OTFS system performance. Finally, we present the simulation results in 5.3.

5.1 OTFS System Model in Static Multipath Channels

We consider an OTFS system with single antenna transmitter and receiver over static multipath channels, i.e., the channel consists of P zero-Doppler multipaths with the ith path delay denoted by τ_i, for $i = 1, 2, \cdots, P$. We assume that a total of $N_c = MN$ symbols are transmitted in an

OTFS frame of duration $N_c T_s$, where T_s is the sampling interval. Let $\tau_{\max} = (L-1)T_s$ denote the maximum delay of an L-tap channel. The static multipath channel is represented by the L tap coefficients $[h_0, h_1, \cdots, h_{L-1}]$, where only P elements are non-zero.

Let $\mathbf{x} = \text{vec}(\mathbf{X}) \in \mathbb{C}^{N_c \times 1}$ denote one OTFS frame containing N_c transmitted information symbols, each with average energy E_s, where the matrix $\mathbf{X} \in \mathbb{C}^{M \times N}$ represents the two-dimensional information symbols transmitted in the delay-Doppler plane. The transmitted time domain signal in OTFS can be obtained by first applying the (2D) *ISFFT* on $\mathbf{X}$ followed by *Heisenberg transform* [17]. Assuming rectangular transmit waveform, the output of the Heisenberg transform can be written from Chapter 3 as

$$\mathbf{S} = \mathbf{F}_M^{\mathrm{H}}(\mathbf{F}_M \mathbf{X} \mathbf{F}_N^{\mathrm{H}}) = \mathbf{X}\mathbf{F}_N^{\mathrm{H}} \tag{5.1}$$

The transmitted time domain signal can be generated by column-wise vectorization of $\mathbf{S}$:

$$\mathbf{s} = \text{vec}(\mathbf{S}) = (\mathbf{F}_N^{\mathrm{H}} \otimes \mathbf{I}_M)\mathbf{x} \tag{5.2}$$

We assume a CP of length $(L-1)$ is added to $\mathbf{s}$ before transmission. The received signal in time domain, after discarding the CP, can be written as

$$\mathbf{r} = \mathbf{H}\mathbf{s} + \mathbf{w}, \tag{5.3}$$

where $\mathbf{H} = \text{circ}[h_0, h_1, \cdots, h_{L-1}, 0, \cdots, 0] \in \mathbb{C}^{N_c \times N_c}$ is the circulant matrix, and $\mathbf{w} \in \mathbb{C}^{N_c \times 1}$ is the i.i.d. Gaussian noise vector with the ith entry, $w_i \sim \mathcal{CN}(0, \sigma^2)$.

At the receiver, the received signal $\mathbf{r}$ is devectorized into an $M \times N$ matrix $\mathbf{R}$, followed by a *Wiegner transform* as well as a SFFT, yielding

$$\mathbf{Y} = \mathbf{F}_M^{\mathrm{H}}(\mathbf{F}_M \mathbf{R})\mathbf{F}_N = \mathbf{R}\mathbf{F}_N \tag{5.4}$$

Finally, the input–output relation of OTFS in the information domain can be obtained by column-wise vectorization of (5.4):

$$\mathbf{y} = \text{vec}(\mathbf{Y}) = (\mathbf{F}_N \otimes \mathbf{I}_M)\mathbf{r}$$
$$= (\mathbf{F}_N \otimes \mathbf{I}_M)\mathbf{H}(\mathbf{F}_N^{\mathrm{H}} \otimes \mathbf{I}_M)\mathbf{x} + \widetilde{\mathbf{w}}$$
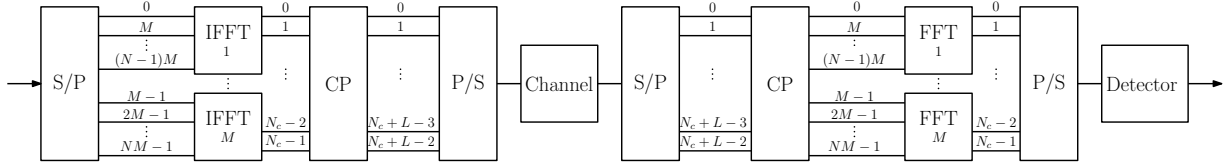
Figure 5.1: OTFS/A-OFDM for static multipath channels

$$= \mathbf{H}_{\text{eff}}\mathbf{x} + \widetilde{\mathbf{w}} \tag{5.5}$$

where $\mathbf{H}_{\text{eff}} = (\mathbf{F}_N \otimes \mathbf{I}_M)\mathbf{H}(\mathbf{F}_N^{\text{H}} \otimes \mathbf{I}_M)$ is the effective channel matrix. Since $(\mathbf{F}_N \otimes \mathbf{I}_M)$ is a unitary matrix, $\widetilde{\mathbf{w}} = (\mathbf{F}_N \otimes \mathbf{I}_M)\mathbf{w}$ preserves the same statistical properties of $\mathbf{w}$.

Let us consider the following two special cases for OTFS over static multipath channels.

1. If $M = 1$ then (5.4) reduces to $\mathbf{y} = \mathbf{F}_N\mathbf{H}\mathbf{F}_N^{\text{H}}\mathbf{x} + \widetilde{\mathbf{w}}$, i.e., a conventional N-subcarrier OFDM system, when a CP is added to $\mathbf{x}$.

2. If $N = 1$ then (5.4) reduces to $\mathbf{y} = \mathbf{H}\mathbf{x} + \widetilde{\mathbf{w}}$, i.e., a conventional CPSC system.

This shows that OTFS can be seen as a generalization of both OFDM and CPSC systems.

5.1.1 Relation Between OTFS and A-OFDM

Now we are ready to reveal the relation between OTFS and A-OFDM systems in static multipath channels.

Specifically, at the transmitter of an A-OFDM system [46, Fig. 1], the input data of length N_c is arranged into an $M \times N$ matrix and a N-point IFFT is then applied to each row. The transmitted outputs after IFFT are read out column-wise and can be written as

$$\breve{\mathbf{S}} = \mathbf{X}\mathbf{F}_N^{\text{H}}, \tag{5.6}$$

which yields the transmitted time domain signal, $\breve{\mathbf{s}} = (\mathbf{F}_N^{\text{H}} \otimes \mathbf{I}_M)\mathbf{x}$.

At the receiver of A-OFDM, the N_c received signals are converted to a $M \times N$ matrix and a N-point FFT is applied to each row. Similar to the transmitter, the receiver output of A-OFDM can be written as

$$\breve{\mathbf{Y}} = \mathbf{R}\mathbf{F}_N$$

$$\breve{\mathbf{y}} = (\mathbf{F}_N \otimes \mathbf{I}_M)\breve{\mathbf{r}} \tag{5.7}$$

Therefore, from (5.1), (5.4), (5.6), and (5.7), we can conclude that, under static multipath channels, OTFS and A-OFDM systems share the same transmitter and receiver structure (see Fig. 5.1).

Note that OTFS/A-OFDM uses M copies of an N-point IFFT and FFT at transmitter and receiver, respectively. Comparing to a conventional OFDM with $N_c = MN$ subcarriers, the complexity of OTFS/A-OFDM reduces from $MN\log_2(MN)$ to $MN\log_2 N$ complex multiplications and the maximum PAPR reduces from MN to N.

5.2   Detection of OTFS/A-OFDM

In this section, we first review traditional ZF and MMSE detections, originally proposed for A-OFDM in [46, 47] and also applicable for OTFS in static multipath channels. Further, we derive a necessary and sufficient condition on the number of subcarriers in OTFS to guarantee that all the transmitted symbols experience uniform channel gains, as in CPSC (a special case of OTFS/A-OFDM). We then apply the low-complexity MP detection algorithm for OTFS (see Chapter 2) with improved error performance over ZF and MMSE detections.

5.2.1   ZF Detection

It was identified in [46, Theorem 1] for A-OFDM that the effective channel matrix has a block diagonal structure, $\mathbf{H}_{\text{eff}} = \text{diag}[\breve{\mathbf{H}}_0, \breve{\mathbf{H}}_1, \cdots, \breve{\mathbf{H}}_{N-1}]$ with $\breve{\mathbf{H}}_0, \cdots, \breve{\mathbf{H}}_{N-1} \in \mathbb{C}^{M \times M}$. Further, each $\breve{\mathbf{H}}_n$, for $n = 0, \cdots, N-1$, can be diagonalized as $\breve{\mathbf{H}}_n = \mathbf{F}_M^{\text{H}} \mathbf{D}_n \mathbf{F}_M$. Therefore, from (5.5), received symbols can be simplified as

$$\mathbf{y}_n = \breve{\mathbf{H}}_n \mathbf{x}_n + \widetilde{\mathbf{w}}_n \tag{5.8}$$

$$\hat{\mathbf{y}}_n = \mathbf{F}_M \mathbf{y}_n = \mathbf{D}_n \mathbf{F}_M \mathbf{x}_n + \mathbf{F}_M \widetilde{\mathbf{w}}_n \tag{5.9}$$

for $n = 0, 1, \cdots, N-1$. Here, $\mathbf{y}_n, \mathbf{x}_n$, and $\widetilde{\mathbf{w}}_n$, are the subvectors formed by taking nM to $(n+1)M-1$ elements from $\mathbf{y}, \mathbf{x}$, and $\widetilde{\mathbf{w}}$, respectively. Hence, the estimated symbols after ZF detection can be

written as

$$\hat{\mathbf{x}}_n = \mathbf{F}_M^{\mathrm{H}} \mathbf{D}_n^{-1} \hat{\mathbf{y}}_n \tag{5.10}$$

5.2.2 MMSE Detection

From (5.9), the estimated symbols after MMSE detection can be written as

$$\hat{\mathbf{x}}_n = \mathbf{F}_M^{\mathrm{H}} \mathbf{D}_n^{\mathrm{H}} \left(\mathbf{D}_n \mathbf{D}_n^{\mathrm{H}} + \frac{\sigma^2}{E_s} \mathbf{I}_M \right)^{-1} \hat{\mathbf{y}}_n \tag{5.11}$$

Note that the complexity of ZF and MMSE detectors is of the order of $\mathcal{O}(M \log_2 M)$. However, ZF and MMSE linear detectors do not fully exploit the available system diversity. Finally, these detection methods do not take advantage of the sparsity of $\breve{\mathbf{H}}_n$.

5.2.3 Message Passing Detection

For OTFS in static multipath channels, we first establish the relation between $\mathbf{H}_{\mathrm{eff}}$ and $\mathbf{H}$ using the following lemma, which is based upon the observation that $\mathbf{H} = \mathrm{circ}[\mathbf{H}_0, \mathbf{H}_1, \cdots, \mathbf{H}_{N-1}]$, is a block circulant matrix, where $\mathbf{H}_n, 0 \leq n \leq N - 1$, are $M \times M$ submatrix.

Lemma 5.1. $\breve{\mathbf{H}}_n(i,j), 0 \leq i,j \leq N - 1$, *is equal to the* n^{th} *element in the FFT of* $\mathbf{u}_{(i,j)} \triangleq [\mathbf{H}_0(i,j), \cdots, \mathbf{H}_{N-1}(i,j)]$.

Proof: Since $\mathbf{H}$ is a block circulant matrix of N blocks of size $M \times M$, it can be block-diagonalized using $(\mathbf{F}_N \otimes \mathbf{I}_M)$ and $(\mathbf{F}_N^{\mathrm{H}} \otimes \mathbf{I}_M)$ [40], and the result follows from (5.5). ■

Next, using Lemma 5.1, we prove the following theorem on the minimum value of M in OTFS to guarantee that all the transmitted symbols experience uniform channel gains, as in CPSC.

Theorem 5.1. *The input–output relation in an OTFS system of* NM *transmitted symbols is equivalent to* N *parallel CPSCs of length* M *with the identical time-domain channel, except for an additional phase shift, if and only if* $M \geq L$.

Proof: See Appendix C.1. ■

Detector

Since the OTFS input–output relation for static multipath channels is sparse (C.2), we propose to use the MP algorithm presented in the Chapter 2. The complexity of MP algorithm for each block is $\mathcal{O}(n_{\text{iter}}MPQ)$, where n_{iter} is the number of iterations in MP and Q is the modulation alphabet size. In general, even the value of L is large, but the value of P can be small, for example, in EVA channel model, $L = 72$ and $P = 9$.

Remark 5.1. *OTFS has the same performance and detection complexity as N consecutive blocks of CPSCs of length M, but has higher spectral efficiency, since OTFS only requires one CP, whereas CPSC requires N CPs. On the other hand, OTFS has a higher PAPR $= N$ than CPSC (PAPR $= 1$). Therefore, OTFS offers a tradeoff between spectral efficiency and PAPR.*

Remark 5.2. *As the proposed MP detector is highly non-linear and the number of codewords are huge, it is difficult to derive the theoretical BER expressions for MP detector. However, we provide the performance of MP using Monte-Carlo simulations in the numerical results section.*

5.2.4 Channel Estimation

We now propose an embedded pilot channel estimation method to estimate the P non-zero channel coefficients for OTFS with $M \geq L$. In this method, we allocate first M symbols of $\mathbf{x}$ as a header and the remaining $M(N - 1)$ symbols for data. In the header, we transmit a known pilot symbol x_p followed by $M - 1$ zeros. Therefore, from (5.8) and (C.2), $\mathbf{y}_0$ reduces to

$$\mathbf{y}_0(m) = h_m x_p + \widetilde{\mathbf{w}}_0(m) \quad \text{for } 0 \leq m \leq M - 1 \tag{5.12}$$

and h_m can be estimated using the threshold method proposed in the Chapter 4. Note that the pilot power $|x_p|^2$ can be M times higher than the data signal power without increasing the average transmitted power.

Also note that OTFS enables simple correction of any carrier frequency offset (CFO). This is due to the fact that the CFO effect is equivalent to applying a single Doppler shift to all the paths in the OTFS channel. This can be easily detected and corrected in the channel estimation using a pilot signal and thus enables to compensate for much larger CFOs than OFDM.
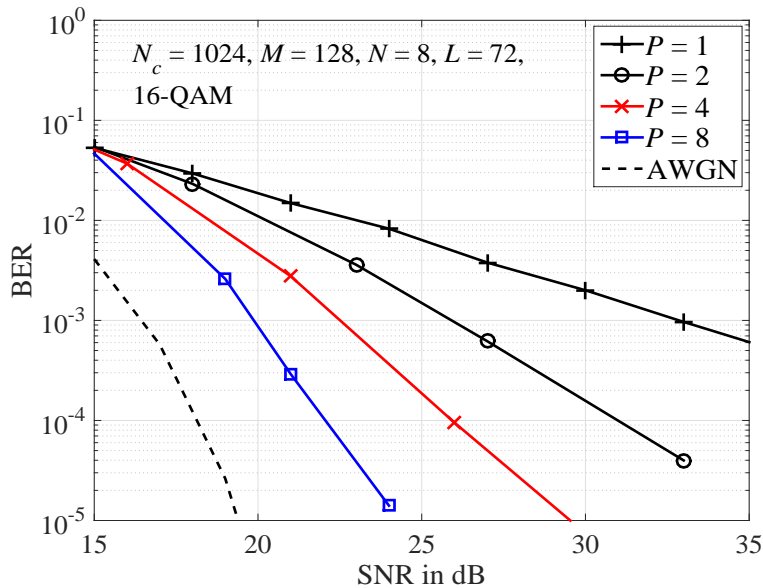
Figure 5.2: BER of OTFS for different P with $N_c = 1024, M = 128, N = 8, L = 72$, and 16-QAM

5.3   Numerical Results and Discussions

In this section, we compare BER of OTFS with OFDM and CPSC for different P and M. In all simulations, we consider $N_c = 1024$ and 16-QAM modulation alphabet ($Q = 16$). In order to obtain BER, we consider 10^5 different channel realizations in Monte-Carlo simulations.

Fig. 5.2 illustrates the BER performance of OTFS for different $P = 1, 2, 4$, and 8 with $M = 128, N = 8, L = 72$. Note that we consider $M > L$ in the figure so that all transmitted symbols experience equal channel gains. We assume that the P paths are uniformly distributed in L, for example, when $P = 4$, we assume only h_0, h_{23}, h_{46}, and h_{69} have non-zero coefficients. Moreover, if $P = 1$ then it reduces to a flat fading channel. The channel coefficients of the P paths are generated using i.i.d. complex Gaussian distribution, $\mathcal{CN}(0, 1/P)$. Here we adopt MP detection algorithm and assume perfect CSI is available at the receiver. We observe from Fig. 5.2 that as P increases, the BER slope improves. This diversity advantage is due to the fact that each information symbol experience the channel gains from P paths.

In Fig. 5.3, we present the performance of OTFS for different M with $L = 72$ and $P = 9$. We consider LTE EVA channel model for generating channel tap coefficients (h_l) and assume perfect CSI is available at the receiver.. We observe that, for $M = 128, 256$, ($M > L$), the performance
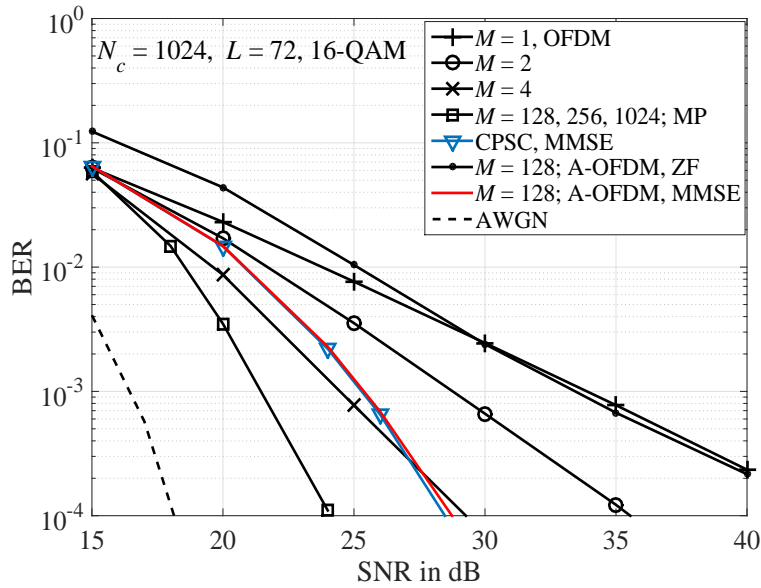
Figure 5.3: BER of OTFS for different M with $N_c = 1024$, $L = 72$, and 16-QAM

of OTFS using MP detection improves with M and achieves the performance similar to CPSC of $M = 1024$, which agrees to Theorem 5.1. Moreover, OTFS using MP detection outperforms OTFS/A-OFDM using MMSE detection by approximately 5 dB, and OFDM by 15 dB. This is due to the fact that MP detection is approximate to maximum likelihood detection and better exploits the full channel diversity, when compared to MMSE.

Fig. 5.4 compares the BER of OTFS for different pilot SNRs, $\mathrm{SNR_p} = |x_p|^2/\sigma^2$, with $M = 128$, $N = 8$ and $L = 72$. We adopt a threshold of $\frac{3}{\sqrt{\mathrm{SNR_p}}}$. We observe that BER performance improves as $\mathrm{SNR_p}$ increases and approaches the performance of the perfect CSI (ideal) case for $\mathrm{SNR_p} = 40$ dB.
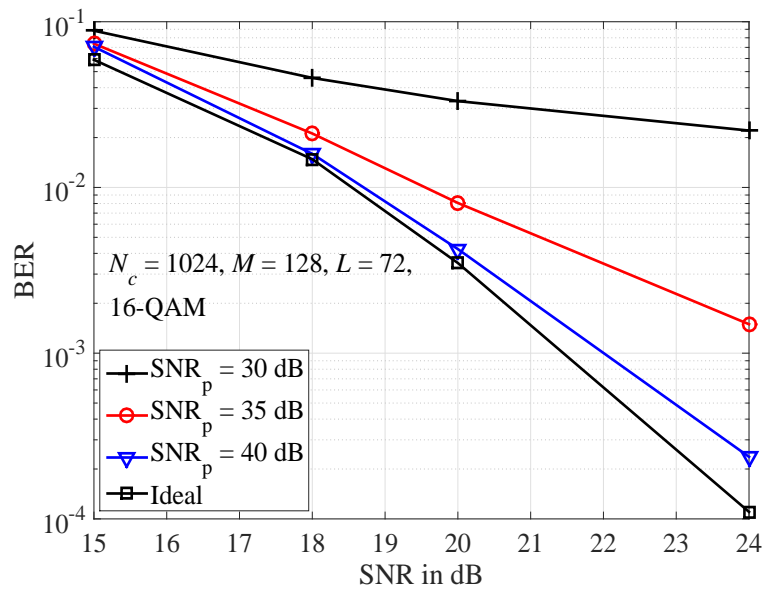
Figure 5.4: BER of OTFS for different SNR_p with $N_c = 1024, M = 128, L = 72$, and 16-QAM

Part 2: Millimeter Wave Analog Beamforming With Low Resolution Phase Shifters

Chapter 6

Channel Estimation in Point-to-Point Millimeter Wave System

In this chapter, we consider analog beamforming using low resolution phase shifters for mm-Wave point-to-point communication system. We propose a hierarchical codebook design, where the beamforming vectors in the codebook are grouped into multiple levels and the preferred beamforming vector at each level is constructed to approximate an amplitude beamforming gain mask by using a low complexity local search algorithm (LSA). We show, by simulations, that the proposed codebook using low resolution phase shifters outperforms the existing schemes using high resolution phase shifters.

The rest of the chapter is organized as follows. In Section 6.1, we present the system model. In Section 6.2, we define the notion of *ideal beamforming vector* with two properties and propose a new codebook design using LSA. The simulation results are shown in Section 6.3.

6.1   System Model

We consider a point-to-point mm-Wave communication system in Fig. 6.1, where the transmitter and receiver have N_t and N_r antennas, respectively, and each has only one RF chain. The phase shifters are assumed to operate on q angles that are spaced uniformly in $[0, 2\pi)$. The set of all

---

Part of the content of this chapter appears as, P. Raviteja, Y. Hong, and E. Viterbo, "Analog beamforming with low resolution phase shifters," *IEEE Wireless Commun. Lett.,*, vol. 6, no. 4, pp. 502-505, Aug. 2017.
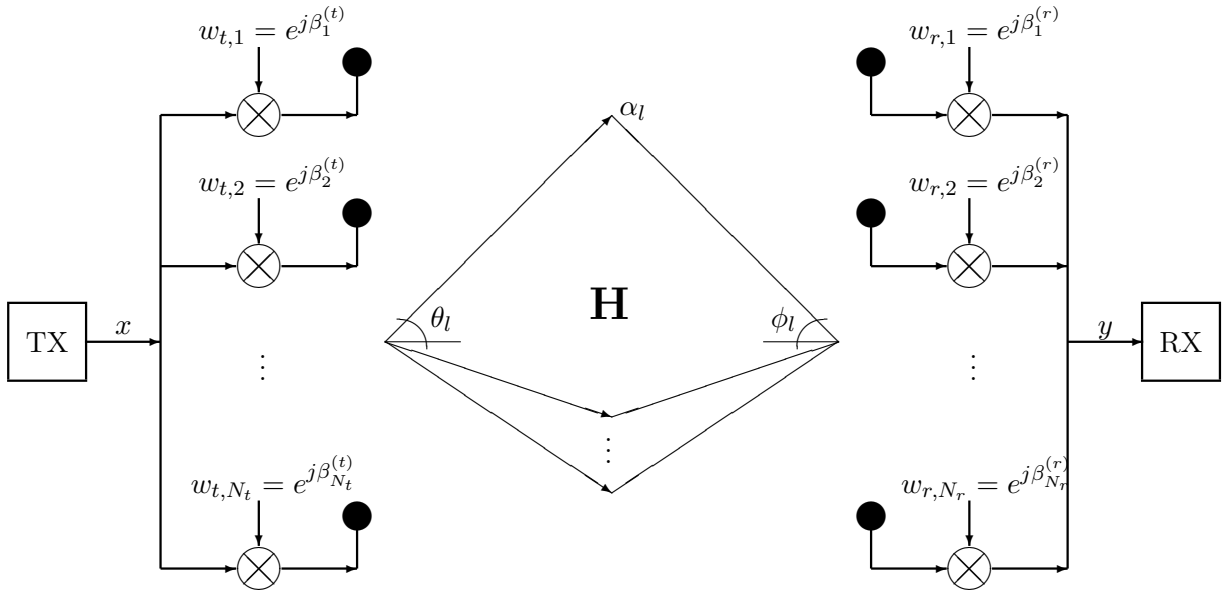
Figure 6.1: Point-to-point analog beamforming system model

possible beamforming vectors for a terminal with N antennas is denoted by

$$\mathcal{S}_q(N) = \left\{ \mathbf{w} \in \mathbb{C}^{N \times 1} : w_i = e^{j\beta_i}, \beta_i \in \left\{ 0, \frac{2\pi}{q}, \ldots, 2\pi \frac{q-1}{q} \right\} \forall\, i = 0, 1, \ldots, N-1 \right\}, \qquad (6.1)$$

where $\|\mathbf{w}\|^2 = N$ and $|\mathcal{S}_q(N)| = q^N$. We let $\mathbf{w}_t$ and $\mathbf{w}_r$ denote the transmit and receive beamforming vectors, chosen from codebooks $\mathcal{C}_t \subset \mathcal{S}_q(N_t)$ and $\mathcal{C}_r \subset \mathcal{S}_q(N_r)$, respectively.

Channel Model: Let the antenna response vector in the angular direction θ be $\mathbf{a}(\theta, N) \triangleq [1, e^{j\pi \cos(\theta)}, \ldots, e^{j\pi(N-1)\cos(\theta)}]^T$ then the millimeter wave channel can be written as

$$\mathbf{H} = \sum_{l=1}^{L} \alpha_l \mathbf{a}(\phi_l, N_r) \mathbf{a}(\theta_l, N_t)^H$$

where $\alpha_l \sim \mathcal{CN}(0, \sigma_{\alpha_l}^2)$ is the path-loss coefficient of the lth path such that $\sum_{l=1}^{L} \sigma_{\alpha_l}^2 = 1$, ϕ_l and θ_l are the corresponding AoA and AoD, respectively, and L is the total number of paths. Since the path loss and materials absorption are high at mm-Wave frequencies, the number of paths can usually be $L = 3$ or 4. We assume ULA at both transmitter and receiver with antenna spacing by half wavelength.

Let x denote the baseband equivalent complex symbol sent through the transmitter phase shifters

$\mathbf{w}_t \in \mathcal{C}_t \subset \mathcal{S}_q(N_t)$, then the received signal after receiver phase shifters $\mathbf{w}_r \in \mathcal{C}_r \subset \mathcal{S}_q(N_r)$ is

$$y = \frac{1}{\sqrt{N_r N_t}} \sum_{l=1}^{L} \alpha_l \mathbf{w}_r^H \mathbf{a}(\phi_l, N_r) \mathbf{a}(\theta_l, N_t)^H \mathbf{w}_t\, x + \mathbf{n}, \qquad (6.2)$$

where $\frac{1}{\sqrt{N_r}}$ and $\frac{1}{\sqrt{N_t}}$ are the normalization factors for $\mathbf{w}_r$ and $\mathbf{w}_t$ respectively, and $\mathbf{n} = (n_1, \ldots, n_{N_r})^T$ is the received noise vector with i.i.d entries (i.e., $n_i \sim \mathcal{CN}(0, \sigma^2)$). Here $|\mathbf{w}_r^H \mathbf{a}(\phi_l, N_r)|$ and $|\mathbf{a}(\theta_l, N_t)^H \mathbf{w}_t|$ represent the beamforming gains of $\mathbf{w}_r$ and $\mathbf{w}_t$ in angular directions ϕ_l and θ_l, respectively.

We define the transmit SNR as $\mathrm{SNR}_{\mathrm{Tx}} \triangleq P_x/\sigma^2$, where $P_x = E\{|x|^2\}$ denotes the transmitted power of the symbol x and σ^2 is the noise power. Similarly, the receive SNR is defined as $\mathrm{SNR}_{\mathrm{Rx}} \triangleq \frac{P_x |\mathbf{w}_r^H \mathbf{H} \mathbf{w}_t|^2}{\sigma^2 N_r N_t}$. The spectral efficiency of the link in (6.2) is given by [71]

$$C = \log_2 \left[1 + \mathrm{SNR}_{\mathrm{Rx}} \right] \quad \text{bits/s/Hz}, \qquad (6.3)$$

which depends on the beamforming vectors $\mathbf{w}_t$ and $\mathbf{w}_r$.

Beamforming Protocol: Considering the hierarchical codebook based protocol (e.g. [71]), the beamforming vectors in the codebook are selected to generate beams with preferred beam-widths and directions. In particular, the beamforming vectors in the codebook are grouped into m different levels. For each level $\ell = 1, \cdots, m$, there are K^ℓ disjoint beams of decreasing beam-width. The protocol selects the narrowest beamforming vectors aligned with the strongest channel path from the transmit/receive codebooks at level m by an exchange of pilot tones. Both transmitter and receiver cooperatively scan all the beamforming vectors in the codebook at level 1 ($K \times K$ pilot tones) and select the best one at that level. Then both of them repeat the search over K^2 beamforming vector pairs at level 2, which cover the same angular region of the best pair at level 1. This process is repeated until the last level m. This protocol only uses mK^2 pilot tones, which improves over the exhaustive search protocol in [73] with K^{2m} pilot tones.

6.2 The Codebook Design Using LSA

In this section, we present our hierarchical codebook design for analog beamforming at a Tx/Rx terminal with arbitrary N antennas using low resolution phase shifters ($q = 4, 8, 16$).

Let us consider the discrete time Fourier transform (DTFT) of a beamforming vector $\mathbf{w}$, using a continuous frequency variable $\omega \in (-1, 1]$, $\mathcal{W}(e^{j\pi\omega}) = \sum_{n=0}^{N-1} \mathbf{w}(n)e^{-jn\pi\omega}$. The DTFT describes the beamforming gain of $\mathbf{w}$ in all azimuth angles $\psi = \cos^{-1}(\omega) \in [0, \pi)$. Therefore, $|\mathcal{W}(e^{j\pi\omega})|$ represents the amplitude beamforming gain given by $\mathbf{w}$ along the angular directions ψ. In order to efficiently plot the radiation pattern of the beamformer, we consider the DTFT at R discrete points $z_1, z_2, \ldots, z_R$, which are equally spaced in $(-1, 1]$, i.e., $z_i = (-1 + \frac{2i}{R})$, for $i = 1, 2, \ldots, R$. Note that this results in a non-uniform angular resolution $(\Delta\psi)$ in the variable ψ, as well as a smooth diagram when $R > N$ is sufficiently large. Fig. 6.2 show the hierarchical codebook structure for $R = 512$. We see that the value of angular resolution $(\Delta\psi)$ is high at the edges (around -1 and 1) and low at the center (around 0) which is due to the behaviour of $\cos(\psi)$.
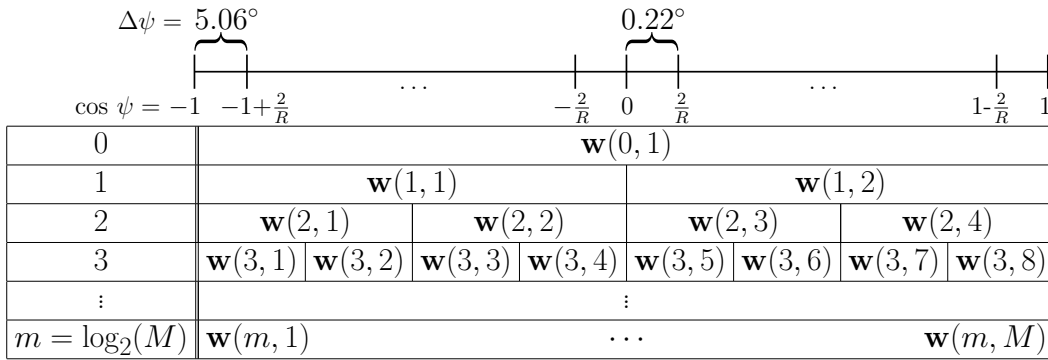
Figure 6.2: The hierarchical codebook structure for $R = 512$.

The corresponding DFT is obtained by defining an $N \times R$ matrix $\mathbf{A}$ such that $\mathbf{A}^H \mathbf{w} = [\mathcal{W}(e^{j\pi z_1}), \ldots, \mathcal{W}(e^{j\pi z_R})]^T$. Then $|\mathbf{A}^H \mathbf{w}| \triangleq [|\mathcal{W}(e^{j\pi z_1})|, \ldots, |\mathcal{W}(e^{j\pi z_R})|]^T$ denotes the vector of amplitude beamforming gains in the angular directions $\psi_i = \pm\cos^{-1}(z_i)$, for $i = 1, 2, \ldots, R$. The matrix $\mathbf{A}^H$ is given by

$$
\mathbf{A}^H = \begin{pmatrix}
1 & e^{-j\pi z_1} & e^{-j\pi 2 z_1} & \cdots & e^{-j\pi(N-1)z_1} \\
\vdots & \vdots & \vdots & \ddots & \vdots \\
1 & 1 & 1 & \cdots & 1 \\
\vdots & \vdots & \vdots & \ddots & \vdots \\
1 & e^{-j\pi z_R} & e^{-j\pi 2 z_R} & \cdots & e^{-j\pi(N-1)z_R}
\end{pmatrix},
$$

$$= \left(\mathbf{a}(\psi_1, N) \quad \mathbf{a}(\psi_2, N) \quad \cdots \quad \mathbf{a}(\psi_R, N) \right)^H . \tag{6.4}$$

Since $z_i = (-1 + \frac{2i}{R})$, the $(R/2)^{th}$ row of $\mathbf{A}^H$ has all one entries and $\mathbf{A}^H$ can be related to the first N columns of an $R \times R$ DFT matrix $\mathbf{F} = \{e^{-j2\pi nk/R}\}_{k,n=0}^{R-1}$ by swapping the block of the first $\frac{R}{2} - 1$ rows with the block of last $\frac{R}{2} + 1$ rows, i.e. the submatrix with the first N columns of $\mathbf{F}$ is given by $\mathbf{F}_N = \mathbf{P}\mathbf{A}^H$, where

$$\mathbf{P} = \begin{pmatrix} \mathbf{0} & \mathbf{I}_{\frac{R}{2}+1} \\ \mathbf{I}_{\frac{R}{2}-1} & \mathbf{0} \end{pmatrix}$$

and $\mathbf{I}_r$ is an $r \times r$ identity matrix and $\mathbf{0}$ is an all zero matrix.

Amplitude Beamforming Gain Mask: The amplitude beamforming gain mask for the beams in the hierarchical codebook should have a constant amplitude in the main lobe and zero everywhere else. We let $\mathbf{g}(\ell, i)$, an R component vector, denote the mask for level $\ell = 1, \ldots, m = \log_K N$ and $i = 1, \ldots, K^\ell$. The j-th component of $\mathbf{g}(\ell, i)$, for $j = 1, \ldots, R$, is given by

$$g_j(\ell, i) \triangleq \begin{cases} c_\ell & \text{if } \frac{R(i-1)}{K^\ell} < j \le \frac{Ri}{K^\ell} \\ 0 & \text{otherwise} \end{cases} . \tag{6.5}$$

where c_ℓ value is given by the following lemma.

Lemma 6.1. *The value of c_ℓ in (6.5) is upper bounded by $\sqrt{NK^\ell}$.*

Proof: See Appendix D.1.   ∎

That is, an ideal steering vector should result in a beam with a constant amplitude c_ℓ in the covered angular region

$$\left[\cos^{-1}\left(-1 + \frac{2i}{K^\ell}\right), \cos^{-1}\left(-1 + \frac{2(i-1)}{K^\ell}\right) \right)$$

and zero in the other angular positions. For example, for $\ell = 1, i = 1$, and $K = 2$, we have

$$\mathbf{g}(1, 1) = [\underbrace{c_1, \ldots, c_1}_{R/2 \text{ values}}, \underbrace{0, \ldots, 0}_{R/2 \text{ values}}]^T$$

covering the angular region $[\pi/2, \pi)$.

Remark 6.1. *In principle it is possible to consider levels $\ell > \log_K N$, where all the beams maintain the same width and gain of level $\ell = \log_K N$, but can be steered to higher resolution angles. In this case, we can still use the non-overlapping masks in (6.5) with the same $c_\ell = N$, for $\ell > \log_K N$. The actual K^ℓ beams will have a larger overlap with a main lobe peak at the mid-angle of the mask and a minimum at the edge of the mask. Our simulations have shown minor performance improvements when $\ell > \log_K N$.*

Hierarchical Codebook Design: Given an arbitrary steering vector $\mathbf{x} \in \mathcal{S}_q(N)$, we let

$$\zeta_{(\ell,i)}(\mathbf{x}) \triangleq \||\mathbf{A}^H\mathbf{x}| - \mathbf{g}(\ell,i)\|^2 \tag{6.6}$$

for $\ell = 1, \ldots, m$, and $i = 1, \ldots, K^\ell$, be the error between the amplitude beamforming gain of $\mathbf{x}$ relative to the amplitude beamforming gain mask $\mathbf{g}(\ell, i)$. Therefore the optimum steering vector $\mathbf{w}(\ell, i) \in \mathcal{S}_q(N)$ is given by

$$\mathbf{w}(\ell, i) \triangleq \underset{\mathbf{x} \in \mathcal{S}_q(N)}{\arg\min} \, \zeta_{(\ell,i)}(\mathbf{x}). \tag{6.7}$$

Then the best hierarchical codebook can be obtained by $\mathcal{C} \triangleq \{\mathbf{w}(\ell, i)|\ell = 1, \ldots, m, \ i = 1, \ldots, K^\ell\}$. The following proposition gives the conditions for which (6.7) can be solved only once for each level.

Proposition 6.1. *If K^ℓ divides q, then $w_s(\ell, p) = w_s(\ell, 1)e^{jr2\pi\left(\frac{p-1}{K^\ell}\right)}$, where $w_s(\ell, p)$ is the sth element in beamforming vector $\mathbf{w}(\ell, p)$, which corresponds to the phase shift of the sth antenna.*

Proof: See Appendix D.2. ∎

Local Search Algorithm (LSA): In the following we drop the index (ℓ, i) for simplicity. An exhaustive search to solve (6.7) has an exponential complexity $|\mathcal{S}_q(N)| = q^N$. For example, in a mm-Wave system with $q = 4$ and $N = 64$, we need to compute $4^{64}(\approx 10^{38.5})$ values. To reduce the complexity, we propose an LSA, which provides a sub-optimal solution to (6.7). The LSA starts with an initial value of $\mathbf{x}$, which can be chosen randomly or obtained by the compressed sensing method proposed in [71]. Then the algorithm computes (6.6) for all the vectors in the neighborhood

of solution $\mathbf{x}$, defined as

$$\mathcal{N}_d(\mathbf{x}) \triangleq \{\mathbf{y} : \mathbf{y} \in \mathcal{S}_q(N) \text{ and } 0 < \|\mathbf{x} - \mathbf{y}\|_0 \leq d\}$$

where $\|\mathbf{x} - \mathbf{y}\|_0$ denotes the number of non-zero values in $(\mathbf{x} - \mathbf{y})$. Hence, we can interpret $\mathcal{N}_d(\mathbf{x})$ as the set of all vectors in $\mathcal{S}_q(N)$ that differ in at most d positions from $\mathbf{x}$. The size of the neighborhood is $|\mathcal{N}_d(\mathbf{x})| = \sum_{i=1}^{d} \binom{N}{i}(q-1)^i$.

If the best solution found in the neighborhood has smaller $\zeta(\mathbf{x})$ than the present solution, then $\mathbf{x}$ is updated. This process stops when the present solution yields a smaller error than all its neighbors. To improve the performance, we can run the algorithm r_s times, each time starting with different initial vector $\mathbf{x}$, and then select the solution with the least error. A similar approach applied to constant envelop multiuser precoding is proposed in [76]. The pseudo-code of LSA is given in **Algorithm 6.1**.

Algorithm 6.1 Local Search Algorithm for Codebook Design

Inputs: $\mathbf{A}$, $\mathbf{g}$, d, r_s

for $i = 1$ **to** r_s **do**

    Compute $\mathbf{x}^{(i)}$ % Initial vector at i^{th} start

    while (1) **do**

        Find $\mathbf{z} = \underset{\mathbf{y} \in \mathcal{N}_d(\mathbf{x}^{(i)})}{\arg\min} \zeta(\mathbf{y})$ % Finding the best vector in neighborhood

        if $\zeta(\mathbf{x}^{(i)}) > \zeta(\mathbf{z})$ **then**

            $\mathbf{x}^{(i)} = \mathbf{z}$ % Update solution with the better

        else

            break % Stop the algorithm if the present sol. is the best in neighborhood

        end if

    end while

end for

Output: $\mathbf{w} = \underset{\mathbf{x}^{(i)}, 1 \leq i \leq r_s}{\arg\min} \zeta(\mathbf{x}^{(i)})$ % Finding the best vector from all the restarts

---

Complexity and convergence: The complexity of the algorithm is $\mathcal{O}(r_s |\mathcal{N}_d(\mathbf{x})|)$. Fig. 6.3 shows the variation of $\zeta(\mathbf{w})/R$ as a function of d and r_s for $N = 32$. We observed that the optimum metric is converging when $d = 2$ and $r_s = 1000$. Note that the codebook design is performed offline and hence large r_s can be used.

In summary, the proposed LSA provides a heuristic solution for any given value of K and N with low resolution phase shifters. In contrast, in [70], the hierarchical codebooks using DEACT
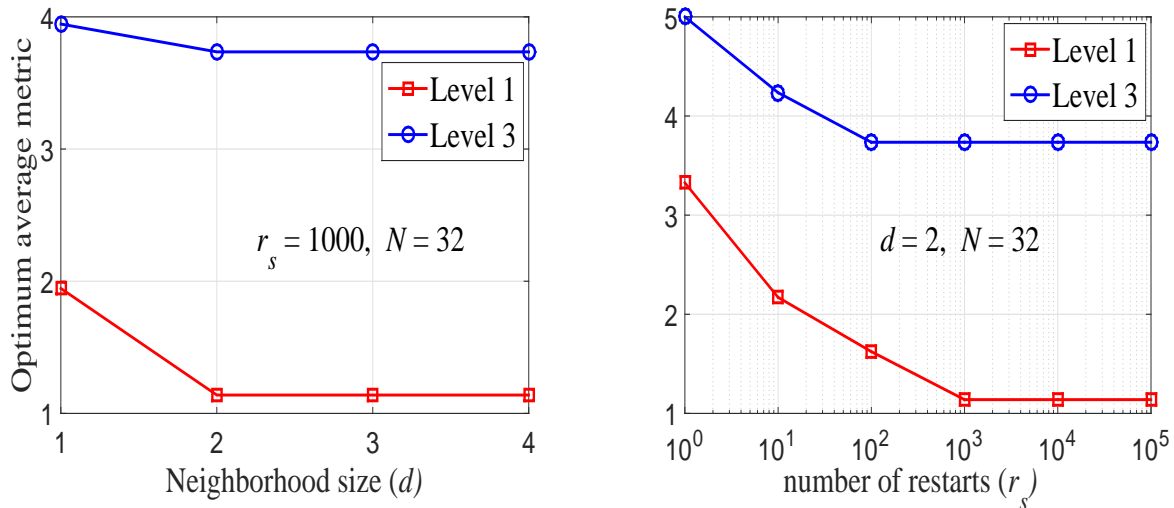
Figure 6.3: The variation of optimum average metric with d and r_s for $N = 32$.

method and BMW-SS method were designed for *non-quantized phase shifters* $(q \to \infty)$ supporting a continuous range of phase shifts, which can only be implemented by high resolution phase shifters. Moreover, for some hierarchical levels in these codebooks, some antennas are turned off. Hence, to preserve a constant total power for all beams, the active antennas have a higher peak power requirement. Further, the BMW-SS approach was designed only for $N = K^p$, for some positive integer p, since it needs to divide the antennas into K smaller sub-arrays, while our method uses all antennas to form the beams, which reduces the peak power.

Furthermore, the method in [71] finds the optimal solution and then quantizes it to the constrained beamforming vector in $\mathcal{S}_q(N)$, where the quantization requires high resolution phase shifters to reduce the overall error. In contrast, our method directly selects the best beamforming vector from the set $\mathcal{S}_q(N)$.

6.3   Simulation Results

In this section, we compare the spectral efficiencies of our hierarchical codebook for low resolution phase shifters $(q = 4, 8, 16)$ and the other codebook using BMW-SS [70] for high resolution phase shifters $(q \to \infty)$. In all simulations, we consider the per-antenna transmission power model in [70] and assume that the power per antenna is the same in all cases rather than a constant total power. We adopt the following parameters: $K = 2$, $N = 32$, 64, 128, $m = \log_2(N)$, $r_s = 1000$, and $d = 2$,

(a) Level 1   (b) Level 2   (c) Level 5
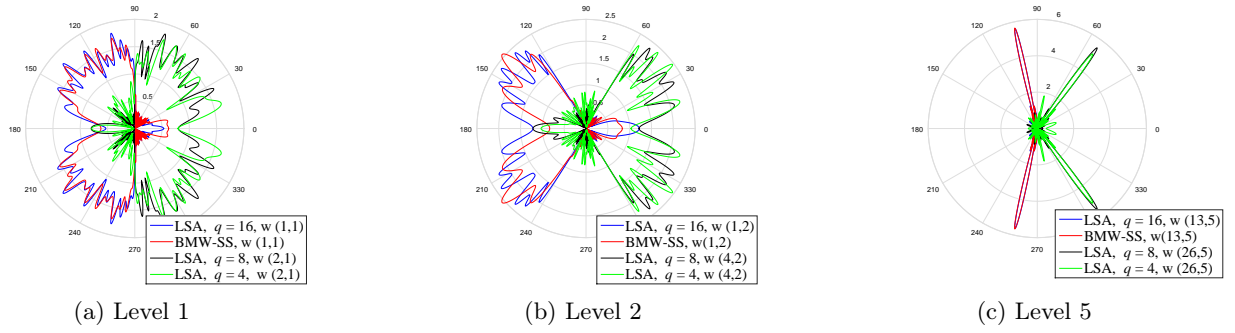
Figure 6.4: Beam pattern of the designed codebook at different levels for $N = 32, K = 2,$ and $d = 2$.

(a) Level 2   (b) Level 3   (c) Level 4
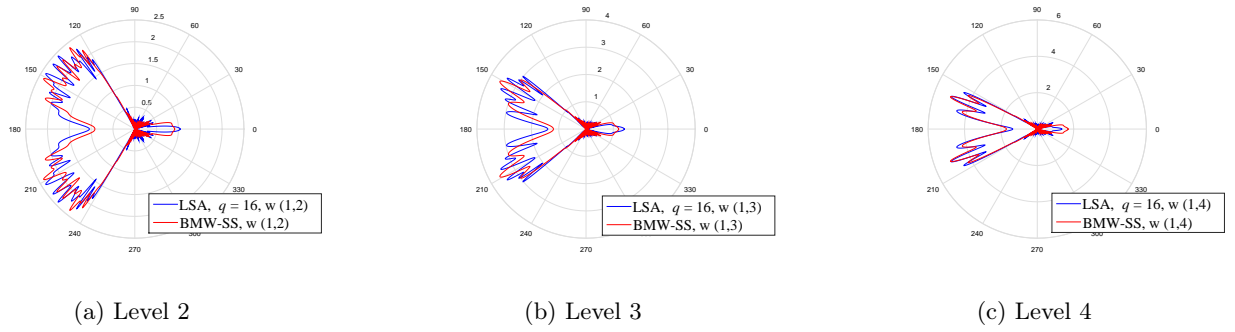
Figure 6.5: Beam pattern of the designed codebook at different levels for $N = 64, K = 2, q = 16,$ and $d = 2$.

and $L = 3$ (channel paths containing one line of sight (LoS) path and two non line of sight (NLoS) paths). We assume the variance of the LoS path (η) is greater than that of the NLoS paths by 10 dB.

In Figs. 6.4 and 6.5, we illustrate the beam pattern for different N and q. We plot the value of the beamforming gain $\frac{1}{\sqrt{N}}|\mathbf{a}(\psi, N)^H \mathbf{w}|$ at an angle $\psi \in (-\pi, \pi]$. We see that the gain is around $\sqrt{K^\ell}$ for the level ℓ in the codebook, which corresponds to the maximum achievable limit given in Lemma 6.1. The gain is almost zero in all other angular directions. We also observe that even with low phase shifter resolutions ($q = 4, 8, 16$), the gain of LSA is comparable to BMW-SS with full resolution phase shifters ($q = \infty$).

Fig. 6.6 illustrates the spectral efficiencies of our codebook with $q = 16$ and the BMW-SS one using high resolution phase shifters [70], for $N = 64, 128$, respectively. The *upper bound* is obtained by assuming the genie-aided receiver that knows perfect CSI and uses the *amplitude beamforming gain mask* in (6.5) for the beam search protocol. The perfect CSI case is plotted with the best
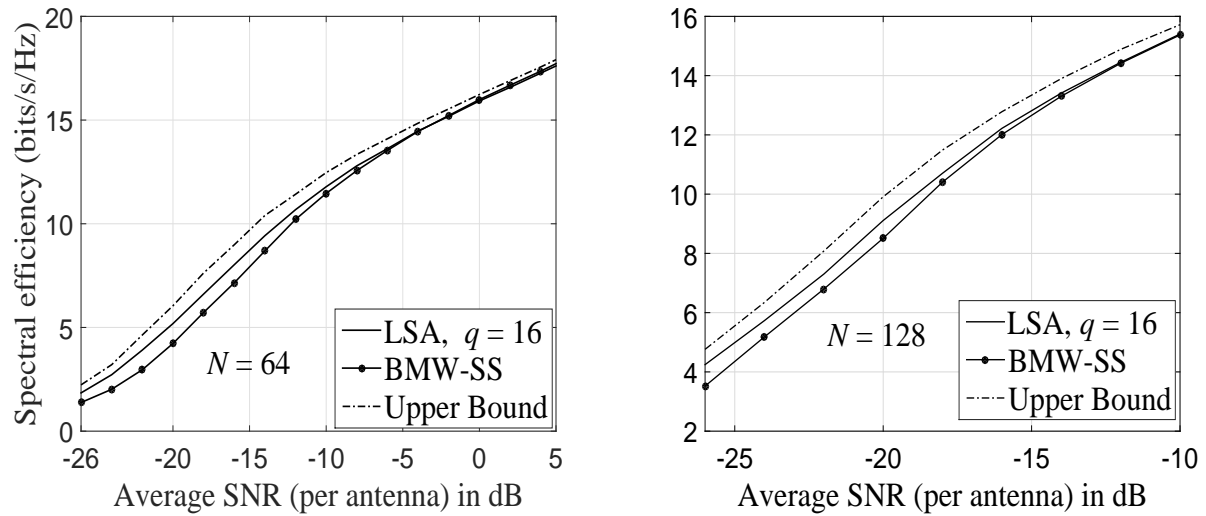
Figure 6.6: The spectral efficiency of the proposed design codebook for different values of N (64, 128) with $L = 3, q = 16, K = 2, r_s = 1000,$ and $d = 2.$
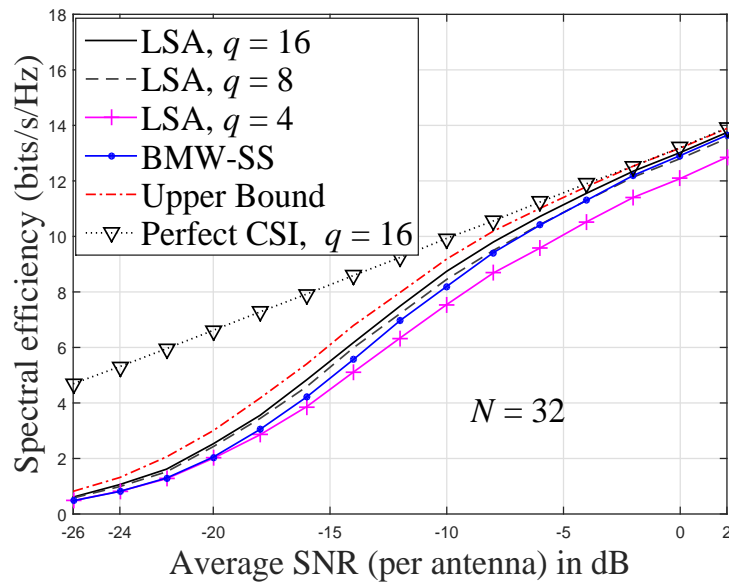
Figure 6.7: The comparison of the proposed LSA design codebook with the BMW-SS method for $N = 32$ and different values of q (4, 8, 16)
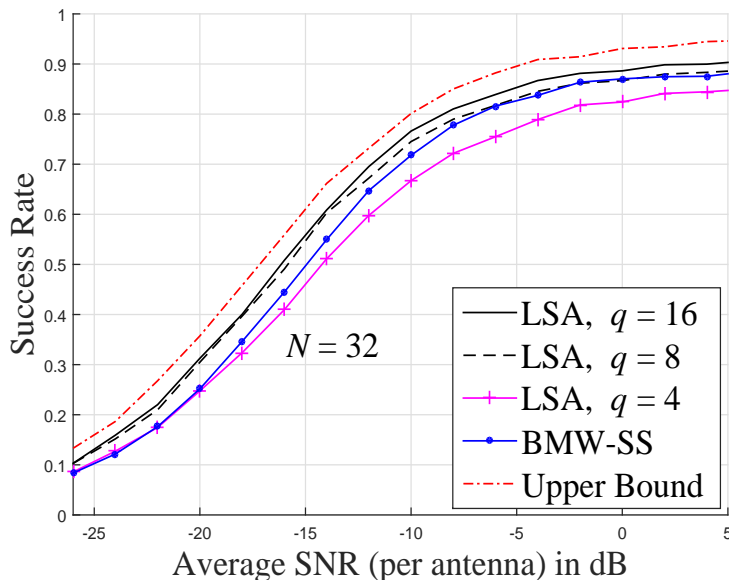
Figure 6.8: The comparison of the proposed LSA design codebook with the BMW-SS method in terms of success rate for $N = 32$ and different values of q (4, 8, 16)

beamforming vectors selected directly using full CSI. We observe that the performance of our codebook with low resolution phase shifters outperforms the BMW-SS codebook with high resolution phase shifters. Similar observations can be found in Fig. 6.7 when $N = 32$, and $q = 8$, 16. When $q = 4$, the codebook using LSA method has similar performance to BMW-SS at low SNR region, but degrades in high SNR region. We also observe that the LSA performance is approaching the perfect CSI case at high SNR's for $q = 16$. Similar performance can also be found for the cases $q = 4$ and $q = 8$.

In Figs. 6.8, 6.9, and 6.10, we show the search performance in terms of *success rate*, as defined in [70], for different values of N. We observe both LSA and BMW-SS have similar performance as the spectral efficiency for all N: worse for $q = 4$, but better for $q = 8, 16$.
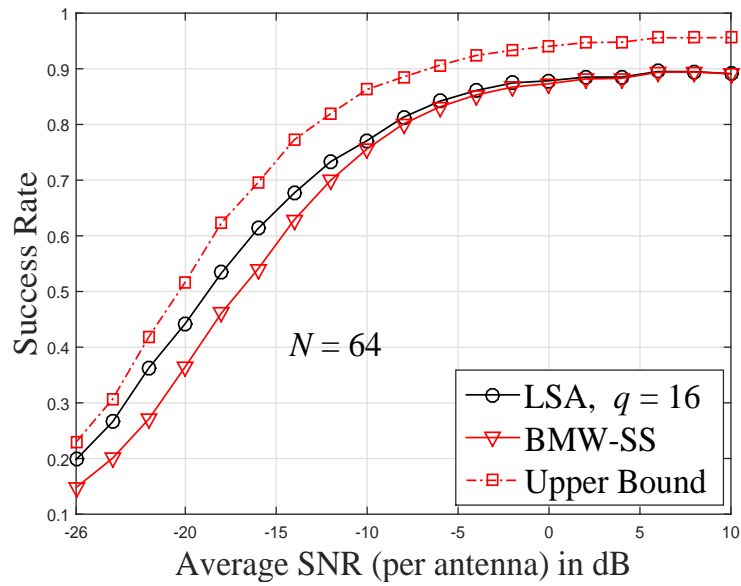
Figure 6.9: The comparison of the proposed LSA design codebook with the BMW-SS method in terms of success rate for $N = 64$ and $q = 16$
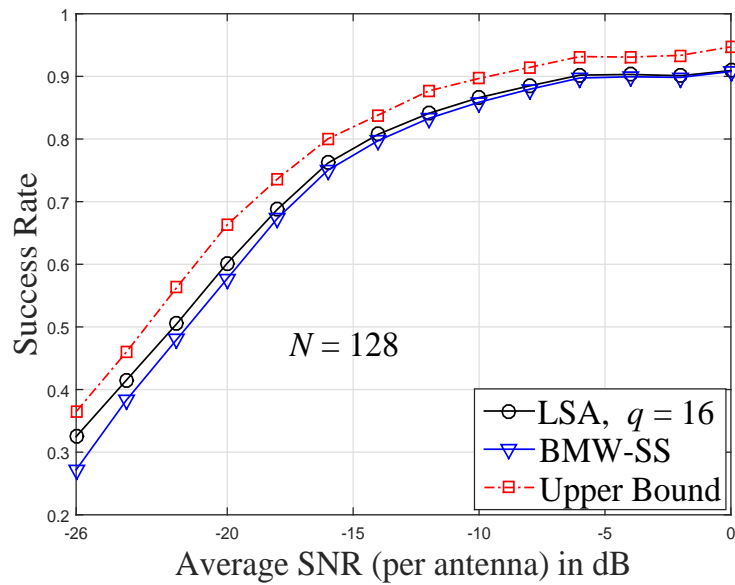
Figure 6.10: The comparison of the proposed LSA design codebook with the BMW-SS method in terms of success rate for $N = 128$ and $q = 16$

Chapter 7

Precoder and Detector Designs in Millimeter Wave Multiuser Uplink System

This chapter extends the idea of designing low resolution beamforming vectors in the previous chapter to the multiuser millimeter wave uplink system, where users transmit simultaneously to base station. In this chapter, we first propose a joint precoder and detector design based on the low-complexity local search algorithm that iteratively finds the preferred transmit and receive beamforming vectors, which maximizes the sum-rate of the multiuser uplink system. Although the joint design achieves similar sum-rate to a fully digital system, the computation complexity to determine good beamforming vectors is high. To reduce complexity, we then propose non-joint designs of precoder and detector. For the precoder design, the transmit beamforming vectors are chosen to maximize either SNR or the SINR of each user. For the detector design, the receiver beamforming vectors are selected using either an approximate ML detector (AMLD) or a successive cancellation detector (SCD). We show by simulations that the proposed designs with low resolution phase shifters outperform the traditional methods with high resolution phase shifters.

The rest of the chapter is organized as follows. We introduce the system model in Section 7.1, and then present the joint precoding and detector design in Section 7.2. We present multiple independent precoding and detector designs in Section 7.3. The simulation results of both joint and independent designs are presented in Section 7.4.
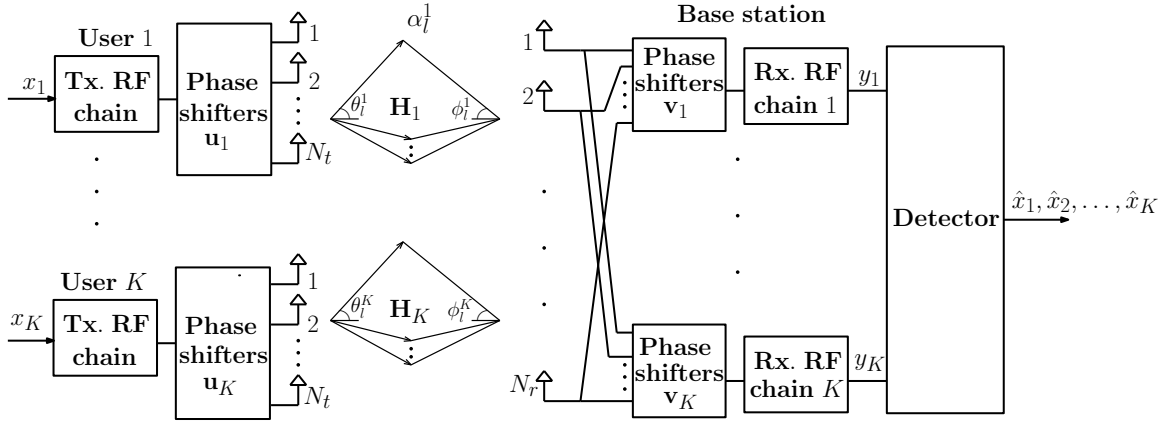
Figure 7.1: Multiuser uplink millimeter wave system.

7.1 System Model

Consider a multiuser uplink mm-Wave system with K users and a BS, as shown in Fig. 7.1. We assume that each user is equipped with N_t transmit antennas over one RF chain, i.e., each user supports only one data stream to be transmitted. We also assume that all K users transmit simultaneously with perfect synchronization to the BS that contains K RF chains and N_r receive antennas. All K users and the BS adopt phase shifters for transmit and receive analog beamforming. These phase shifters change phases of analog signals by a discrete number of steps q, and the q phase shifts are uniformly distributed in $[0, 2\pi)$.

Let $\mathcal{S}_q(N)$ be the set of all possible beamforming vectors of phase shifters of a terminal with N antennas as in Chapter 6, i.e.,

$$\mathcal{S}_q(N) = \left\{ \mathbf{w} \in \mathbb{C}^{N \times 1} : w_i = e^{j\beta_i}, \beta_i \in \left\{0, \frac{2\pi}{q}, \ldots, 2\pi \frac{q-1}{q}\right\} \forall \, i = 0, 1, \ldots, N-1 \right\}. \tag{7.1}$$

with $\|\mathbf{w}\|^2 = N$ and $|\mathcal{S}_q(N)| = q^N$. We let $\mathbf{u}_i \in \mathbb{C}^{N_t \times 1}$ and $\mathbf{v}_j \in \mathbb{C}^{N_r \times 1}$ represent the transmit and receive beamforming vectors at the ith user and the jth RF chain of the BS, respectively, chosen from the codebooks $\mathbf{u}_i \in \mathcal{C}_t \subset \mathcal{S}_q(N_t)$, $\mathbf{v}_j \in \mathcal{C}_r \subset \mathcal{S}_q(N_r)$, $i, j = 1, \ldots, K$.

We assume ULA antenna structure at all terminals (users and the BS) with $\lambda/2$ antenna spacing, where λ is the carrier wavelength. Let the antenna response vector in the angular direction θ be

$$\mathbf{a}(\theta, N) \triangleq [1, e^{j\pi \cos(\theta)}, \ldots, e^{j\pi(N-1)\cos(\theta)}]^T , \tag{7.2}$$

then the channel between the BS and the ith user, $\mathbf{H}_i \in \mathbb{C}^{N_r \times N_t}$, $i = 1, \ldots, K$, is of the form

$$\mathbf{H}_i = \frac{1}{\sqrt{L}} \sum_{l=1}^{L} \alpha_l^i \mathbf{a}(\phi_l^i, N_r) \mathbf{a}(\theta_l^i, N_t)^H, \tag{7.3}$$

where L is the total number of propagation paths, α_l^i is the gain of the l-th path, ϕ_l^i and θ_l^i are the corresponding AoA and AoD, respectively.

Let x_i be the unit power complex symbol (base-band equivalent) taken from a modulation alphabet $\mathcal{A}$ such as M-QAM, transmitted through the transmit phase shifters $\mathbf{u}_i \in \mathbb{C}^{N_t \times 1}$ of the i-th user. Then the received signal at the jth RF chain of the BS after using receive phase shifters $\mathbf{v}_j \in \mathbb{C}^{N_r \times 1}$, is given by

$$y_j = \sqrt{\frac{P}{N_t N_r}} \mathbf{v}_j^H \sum_{i=1}^{K} \mathbf{H}_i \mathbf{u}_i x_i + \sqrt{\frac{1}{N_r}} \mathbf{v}_j^H \mathbf{n}, \ j = 1, \ldots, K, \tag{7.4}$$

where P is the average transmit power of each user, $\sqrt{\frac{1}{N_t}}$ and $\sqrt{\frac{1}{N_r}}$ are the normalization factors for $\mathbf{u}_i$ and $\mathbf{v}_j$, respectively, and $\mathbf{n} \in \mathbb{C}^{N_r \times 1}$ is the noise vector with each entry $\sim \mathcal{CN}(0, \sigma^2)$. After the receive phase shifters, $y_j, \ j = 1, \cdots, K$ are passed to the detector, which is in digital domain, to estimate the transmitted signals. Different detector designs are explained in next sections. We consider SNR $= P/\sigma^2$ as the average transmit power per user to noise ratio. Here, we name $\tilde{\mathbf{h}}_i \triangleq \mathbf{H}_i \mathbf{u}_i$ as the *effective channel* for user i.

In our system, we assume the channel state information is available only at the receiving base station. Specifically, the BS first computes the transmit and receive beamforming vectors based on the proposed design, and then forwards the beamforming vectors ($N_t \log_2 q$ bits) to each user. Millimeter wave channel information can be found by using the compressive-sensing approaches as discussed in [71,97]. These compressive-sensing approaches can be applied to analog beamforming with low resolution phase shifters, as discussed in Chapter 6. The algorithms proposed in [83,84] uses AoD and channel gains to compute the beamforming vectors in the multiuser downlink system. In this work, we assume the full channel state information, which requires AoA in addition to AoD and channel gains. Beamforming designs in multiuser uplink that uses only AoA information is very interesting and we consider it in our future work.

From (7.4), we clearly observe that the system performance depends on the selection of transmit

and receive beamforming vectors $\mathbf{u}_i$ and $\mathbf{v}_j$, respectively, for $i, j = 1, \ldots, K$. In the following, we denote the selection of $\mathbf{u}_i$'s and $\mathbf{v}_j$'s as *precoder* and *detector design.*

7.2   Joint Precoder and Detector Design

In this section, we propose a joint precoder and detector [1] design for low resolution phase shifters ($q = 4, 8, 16$). The preferred transmit and receive beamforming vectors $\mathbf{u}_i$ and $\mathbf{v}_j$, $i, j \in [1, K]$ are chosen to approximately maximize the sum-rate of the uplink system by using an iterative joint search algorithm.

We first rewrite (7.4) as

$$\mathbf{y} = \sqrt{P}\, \mathbf{V}^H \mathbf{H} \mathbf{U} \mathbf{x} + \mathbf{V}^H \mathbf{n}$$
$$= \sqrt{P}\, \tilde{\mathbf{H}} \mathbf{x} + \mathbf{V}^H \mathbf{n}, \tag{7.5}$$

where $\mathbf{y} \triangleq [y_1 \, y_2 \, \cdots \, y_K]$, $\mathbf{V} \triangleq \sqrt{\frac{1}{N_r}} [\mathbf{v}_1 \, \mathbf{v}_2 \, \cdots \, \mathbf{v}_K] \in \mathbb{C}^{N_r \times K}$, $\mathbf{H} \triangleq [\mathbf{H}_1 \, \mathbf{H}_2 \, \cdots \, \mathbf{H}_K] \in \mathbb{C}^{N_r \times K N_t}$, $\mathbf{x} \triangleq [x_1 \, x_2 \, \cdots \, x_K] \in \mathbb{C}^{K \times 1}$, $\tilde{\mathbf{H}} \triangleq \mathbf{V}^H \mathbf{H} \mathbf{U} \in \mathbb{C}^{N_r \times K}$, and

$$\mathbf{U} \triangleq \sqrt{\frac{1}{N_t}} \begin{bmatrix} \mathbf{u}_1 & \mathbf{0} & \cdots & \mathbf{0} \\ \mathbf{0} & \mathbf{u}_2 & \cdots & \mathbf{0} \\ \vdots & \vdots & \ddots & \vdots \\ \mathbf{0} & \mathbf{0} & \cdots & \mathbf{u}_K \end{bmatrix} \in \mathbb{C}^{K N_t \times K}.$$

Let the sum-rate of the multiuser uplink system be

$$C = \log_2 \det \left[\frac{P}{\sigma^2} \tilde{\mathbf{H}} \tilde{\mathbf{H}}^H + \mathbf{V}^H \mathbf{V} \right]$$
$$= \log_2 \det \left[\frac{P}{\sigma^2} \mathbf{V}^H \mathbf{H} \mathbf{U} \mathbf{U}^H \mathbf{H}^H \mathbf{V} + \mathbf{V}^H \mathbf{V} \right] \text{bits/s/Hz}, \tag{7.6}$$

---

[1] We use the detector term to represent both the combiner operation at analog beamforming stage and the detection part at digital stage.

Then our joint design aims at finding the best $\mathbf{U}$ and $\mathbf{V}$ to maximize C, i.e.,

$$\hat{\mathbf{U}}, \hat{\mathbf{V}} = \arg\max_{\mathbf{U},\mathbf{V}} \det \left[\frac{P}{\sigma^2} \mathbf{V}^H \mathbf{H} \mathbf{U} \mathbf{U}^H \mathbf{H}^H \mathbf{V} + \mathbf{V}^H \mathbf{V} \right]$$

$$= \arg\max_{\mathbf{U},\mathbf{V}} f(\mathbf{U}, \mathbf{V}). \tag{7.7}$$

where $f(\mathbf{U}, \mathbf{V})$ is named as the *metric of the joint precoder and detector design.*

This sum-rate expression is the same as the one in [91] except for the analog receive beamforming ($\mathbf{V}$) at BS which is due to the hybrid architecture used in mm-Wave systems, whereas full digital signal is used for microwave communications in [91]. After analog processing at BS, we assume optimal detection in digital stage (see Section 7.3.2 for details). Note that the optimization of the metric in (7.7) is different from the one considered in mm-Wave literature [93, 96, 98], where receive SINR is maximized by using linear detectors such as MMSE.

To solve (7.7), the brute-force search requires an exponential computation complexity of

$$|\mathcal{S}_q(N_t)|^K |\mathcal{S}_q(N_r)|^K = q^{K(N_t+N_r)}.$$

Even for a small mm-Wave system of $q = 4, K = 2, N_t = 16$, and $N_r = 16$, it requires to compute 4^{64} values. To reduce the complexity, we propose a *low complexity iterative joint precoder and detector design* algorithm, which can find a sub-optimal solution to (7.7).

Iterative Joint Design Algorithm: The iterative joint design algorithm starts with the randomly chosen initial values of $\hat{\mathbf{U}}$ and $\hat{\mathbf{V}}$. In each iteration we sequentially update $\hat{\mathbf{U}}$ and $\hat{\mathbf{V}}$ using the local search (LS) method, as discussed below. The output of the previous iteration is used as the initial solution for LS in the next iteration. The algorithm stops when the difference of C between successive iterations is arbitrarily small or when the maximum iterations are reached.

Local Search (LS) Method: LS starts with an initial solution. Then it computes the best solution to (7.7) in the neighborhood of the initial solution. We denote the neighborhood of $\mathbf{x} \in \mathcal{S}_q(N)$ as $\mathcal{N}_{d,N}(\mathbf{x})$, which is the set of all vectors in $\mathcal{S}_q(N)$ that differs in at most d positions from $\mathbf{x}$, i.e.,

$$\mathcal{N}_{d,N}(\mathbf{x}) \triangleq \{\mathbf{p} : \mathbf{p} \in \mathcal{S}_q(N) \text{ and } 0 < \|\mathbf{x} - \mathbf{y}\|_0 \leq d\}, \tag{7.8}$$

where $\|\mathbf{x} - \mathbf{y}\|_0$ denotes the number of non-zero values in $(\mathbf{x} - \mathbf{y})$ and

$$|\mathcal{N}_{d,N}(\mathbf{x})| = \sum_{i=1}^{d} \binom{N}{i}(q-1)^i .$$

The pseudocode of the proposed joint design is presented in **Algorithm 7.1**. Note that, in the pseudocode, at the t-th iteration, $\hat{\mathbf{U}}_{(i,\mathbf{p})}^{(t)}$ and $\hat{\mathbf{V}}_{(j,\mathbf{p})}^{(t)}$ are obtained by replacing $\mathbf{u}_i^{(t)}$ and $\mathbf{v}_j^{(t)}$ with the vector $\mathbf{p}$ in $\hat{\mathbf{U}}^{(t)}$ and $\hat{\mathbf{V}}^{(t)}$, respectively.

Note that a tabu search algorithm similar to this local search was proposed in [88] to find the near-optimal analog beamforming vectors for point-to-point mm-Wave system. This scheme is different from our algorithm in two aspects: $i)$ we consider multiuser uplink system and $ii)$ we consider the full search space $\mathcal{S}_q(N)$ for finding beamforming vectors whereas only steering vectors $(\mathbf{a}(\theta, N))$ were used in [88].

Remark 7.1. *Please note the following points regarding the motivation of the joint design proposed in this work. The optimal closed form solution is not known even for a full digital system without constant amplitude phase shifters constraint. An iterative solution was proposed for full digital system in [89], but its convergence has never been studied for hybrid systems. Even if an optimal iterative solution were available, approximating this solution with the hybrid beamforming matrix requires* high resolution phase shifters *and* a large number of RF chains *[85]. This is in contrast to our assumption that users have* only one RF chain *and* low resolution phase shifters. *In this case, there will be a significant performance loss, compared to the optimal solution.*

7.2.1 Complexity

The complexity of the precoder design is $\mathcal{O}(Kl_p(|\mathcal{N}_{d,N_t}(\mathbf{x})|)((2K)^3 + N_r))$, where l_p represents the number of loops in LS, $|\mathcal{N}_{d,N_t}(\mathbf{x})|$ is the total number of neighbour vectors tested in each loop, and $(2K)^3 + N_r$ is the complexity taking into account of both determinant computation and the operations needed for updating $\frac{P}{\sigma^2}\tilde{\mathbf{H}}\tilde{\mathbf{H}}^H + \mathbf{V}^H\mathbf{V}$ for every neighborhood vector (only one column in $\mathbf{U}$ is updated and no updates in $\mathbf{V}$).

Similarly, the complexity of the detector design is $\mathcal{O}(Kl_d(|\mathcal{N}_{d,N_r}(\mathbf{x})|)((2K)^3 + K))$, where l_d is the number of loops in LS and $|\mathcal{N}_{d,N_r}(\mathbf{x})|$ is the total number of neighbour vectors tested in each loop.

Algorithm 7.1 The Joint Precoder and Detector Design

1: **Input:** $\mathbf{H}_1, \mathbf{H}_2, \cdots, \mathbf{H}_K$
2: **Initialize:** $\hat{\mathbf{u}}_i^{(0)}$, $\hat{\mathbf{v}}_j^{(0)}$, for $i, j = 1, \cdots, K$
3: **for** $t = 1$ **to** number_of_iterations **do**
4:      $\hat{\mathbf{U}}^{(t)} \leftarrow \hat{\mathbf{U}}^{(t-1)}$
5:      $\hat{\mathbf{V}}^{(t)} \leftarrow \hat{\mathbf{V}}^{(t-1)}$
6:      **for** $i = 1$ **to** K **do**
7:          $\mathbf{x} \leftarrow \hat{\mathbf{u}}_i^{(t)}$
8:          **while** (1) **do**
9:              Find $\mathbf{z} \leftarrow \underset{\mathbf{p} \in \mathcal{N}_{d,N_t}(\mathbf{x})}{\arg\max} \; f(\hat{\mathbf{U}}_{(i,\mathbf{p})}^{(t)}, \hat{\mathbf{V}}^{(t)})$
10:              **if** $f(\hat{\mathbf{U}}_{(i,\mathbf{z})}^{(t)}, \hat{\mathbf{V}}^{(t)}) > f(\hat{\mathbf{U}}_{(i,\mathbf{x})}^{(t)}, \hat{\mathbf{V}}^{(t)})$ **then**
11:                  $\mathbf{x} \leftarrow \mathbf{z}$
12:              **else**
13:                  break
14:              **end if**
15:          **end while**
16:          $\hat{\mathbf{u}}_i^{(t)} \leftarrow \mathbf{x},$
17:          $\hat{\mathbf{U}}^{(t)} \leftarrow \hat{\mathbf{U}}_{(i,\mathbf{x})}^{(t)}$
18:      **end for**
19:      **for** $j = 1$ **to** K **do**
20:          $\mathbf{x} \leftarrow \hat{\mathbf{v}}_j^{(t)}$
21:          **while** (1) **do**
22:              Find $\mathbf{z} \leftarrow \underset{\mathbf{p} \in \mathcal{N}_{d,N_r}(\mathbf{x})}{\arg\max} \; f(\hat{\mathbf{U}}^{(t)}, \hat{\mathbf{V}}_{(j,\mathbf{p})}^{(t)})$
23:              **if** $f(\hat{\mathbf{U}}^{(t)}, \hat{\mathbf{V}}_{(j,\mathbf{z})}^{(t)}) > f(\hat{\mathbf{U}}^{(t)}, \hat{\mathbf{V}}_{(j,\mathbf{x})}^{(t)})$ **then**
24:                  $\mathbf{x} \leftarrow \mathbf{z}$
25:              **else**
26:                  break
27:              **end if**
28:          **end while**
29:          $\hat{\mathbf{v}}_j^{(t)} \leftarrow \mathbf{x}$
30:          $\hat{\mathbf{V}}^{(t)} \leftarrow \hat{\mathbf{V}}_{(j,\mathbf{x})}^{(t)}$
31:      **end for**
32:      **if** $\frac{f(\hat{\mathbf{U}}^{(t)}, \hat{\mathbf{V}}^{(t)})}{f(\hat{\mathbf{U}}^{(t-1)}, \hat{\mathbf{V}}^{(t-1)})} < 2^\epsilon$ **then**
33:          break
34:      **end if**
35: **end for**
36: **Output:** $\hat{\mathbf{u}}_i^{(t)}$, $\hat{\mathbf{v}}_j^{(t)}$, for $i, j = 1, \cdots, K$

Finally, the complexity of the joint design is $N_{\text{Iter}} \times C_{\text{Iter}}$, where N_{Iter} is the total number of iterations in the joint design, and

$$C_{\text{Iter}} = (\mathcal{O}(Kl_p(|\mathcal{N}_{d,N_t}(\mathbf{x})|)((2K)^3 + N_r)) + \mathcal{O}(Kl_d(|\mathcal{N}_{d,N_r}(\mathbf{x})|)((2K)^3 + K)))$$

is the complexity of joint design per iteration.

7.2.2   Detection

The received signal vector in (7.5) contains the transmitted signals and the colored Gaussian noise $\mathbf{V}^H\mathbf{n}$ with covariance matrix $\Sigma = \mathbf{V}^H\mathbf{V}$. Applying ML detection yields

$$
\begin{aligned}
\hat{\mathbf{x}} &= \arg\max_{\mathbf{x}\in\mathcal{A}^K} \Pr(\mathbf{y}/\tilde{\mathbf{H}}, \mathbf{x}) \\
&= \arg\min_{\mathbf{x}\in\mathcal{A}^K} (\mathbf{y} - \sqrt{P}\tilde{\mathbf{H}}\mathbf{x})^H \Sigma^{-1} (\mathbf{y} - \sqrt{P}\tilde{\mathbf{H}}\mathbf{x}) \\
&= \arg\min_{\mathbf{x}\in\mathcal{A}^K} \|\mathbf{L}^H\mathbf{y} - \sqrt{P}\mathbf{L}^H\tilde{\mathbf{H}}\mathbf{x}\|^2,
\end{aligned}
\tag{7.9}
$$

where $\mathbf{L}$ is the lower triangular matrix in the Cholesky decomposition of Σ^{-1}, i.e., $\mathbf{LL}^H = \Sigma^{-1}$. A sphere decoding ML can be implemented to solve (7.9).

7.2.3   Upper Bound on Sum-rate

The upper bound on sum-rate is computed based upon the following setting.

1. We assume fully digital systems for users and the BS, i.e., each user has N_t RF chains and the BS has N_r RF chains, and thus all N_r received signals are available at the BS.

2. We consider all users are cooperative and then the precoder matrix $\mathbf{U}_{\text{dig}}$ is a full complex-entry matrix. To maintain the total power constraint, we consider only the orthonormal vectors as the columns of $\mathbf{U}_{\text{dig}}$, i.e., $\mathbf{U}_{\text{dig}}^H\mathbf{U}_{\text{dig}} = \mathbf{I}_K$.

The received signal for the point-to-point digital system is

$$
\begin{aligned}
\mathbf{y}_{\text{dig}} &= \sqrt{P}\,\mathbf{H}\mathbf{U}_{\text{dig}}\mathbf{x} + \mathbf{n} \\
&= \mathbf{H}\mathbf{x}_{\text{dig}} + \mathbf{n},
\end{aligned}
\tag{7.10}
$$

where $\mathbf{x}_{\text{dig}} = \mathbf{U}_{\text{dig}}\mathbf{x}$ and $\|\mathbf{x}\|^2 = \|\mathbf{x}_{\text{dig}}\|^2$. The achievable rate of the system in (7.10) is given by

$$C_{\text{dig}} = \log_2 \det \left[\frac{P}{\sigma^2}\mathbf{H}\mathbf{H}^H + \mathbf{I}_{N_r} \right] \text{bits/s/Hz.} \tag{7.11}$$

By using singular value decomposition (SVD) of $\mathbf{H}$, the rate in (7.11) can be written as [28],

$$C \le C_{\text{dig}} = \sum_{i=1}^{K} \log_2 \left(1 + \frac{\lambda_i^2 P}{\sigma^2} \right) \text{bits/s/Hz,} \tag{7.12}$$

where λ_i, for $i = 1, \cdots, K$ are the K largest singular values of $\mathbf{H}$.

Through the simulation results in Sec. 7.4.1, we can observe that the sum-rate of the proposed joint precoder and detector design is very close to the upper bound. Although the joint design performs well, it requires high complexity. To reduce the complexity, we propose separate designs of precoder and detector in the next section.

7.3   Separate Precoder and Detector Design

In this section, we present the two precoder designs based on SNR and SINR maximization, followed by the two detector designs.

7.3.1   The Precoder Design

We propose two different precoder designs for limited resolution phase shifters ($q = 4, 8, 16$).

Conventional Precoder (CP)

For user i with its known CSI, the conventional precoder selects $\mathbf{u}_i$ that maximizes the total effective channel power, i.e.,

$$\mathbf{u}_i = \arg\max_{\mathbf{x} \in \mathcal{S}_q(N_t)} \|\mathbf{H}_i\mathbf{x}\|^2, \text{for } i = 1, \ldots, K. \tag{7.13}$$

This design requires a very high processing time as $|\mathcal{S}_q(N_t)| = q^{N_t}$. For example, in the case of $q = 16$ and $N_t = 16$, we need to check for 16^{16} values, which is impractical. To reduce the complexity, we adopt LS method to find an approximate solution to (7.13). In LS, we consider $\mathcal{E}(\mathbf{x}) \triangleq \|\mathbf{H}_i\mathbf{x}\|^2$

as the *metric of the algorithm.* The complexity of this algorithm is $\mathcal{O}(Kl_p|\mathcal{N}_{d,N_t}(\mathbf{x})|)$, much less than joint design in Section 7.2.

However, the performance of CP can be poor due to high correlation between the effective channels of different users. Consequently, the BS fails to distinguish different users, since the precoder design is based only on the respective channel of each user. To reduce such correlations by taking advantage of other users' CSIs, we propose below a successive estimation precoder.

Successive Estimation Precoder (SEP)

We let $i_1, i_2, \ldots, i_K \in \{1, \ldots, k, \ldots, K\}$ be the *users order*, for which each precoding vector is successively computed to maximize its SINR. Here, the SINR of user i_k is defined as the ratio of the user's total effective channel power and the interference from users $i_1, \ldots, i_{k-1}$ together with the noise.

Matched Filter (MF) Based SINR

For user i_k, based on the MF detector weights (i.e., $(\mathbf{H}_{i_k}\mathbf{x})^H / \|\mathbf{H}_{i_k}\mathbf{x}\|$) for its SINR computation, the SEP selects $\mathbf{u}_{i_k}$ such as

$$
\begin{aligned}
\mathbf{u}_{i_k} &= \arg\max_{\mathbf{x}\in\mathcal{S}_q(N_t)} \frac{\|\mathbf{H}_{i_k}\mathbf{x}\|^2}{\displaystyle\sum_{j=1}^{k-1} \left| \frac{(\mathbf{H}_{i_k}\mathbf{x})^H}{\|\mathbf{H}_{i_k}\mathbf{x}\|} (\mathbf{H}_{i_j}\mathbf{u}_{i_j}) \right|^2 + N_t\sigma^2}, \\
&= \arg\max_{\mathbf{x}\in\mathcal{S}_q(N_t)} \mathcal{Z}_{i_k}^k(\mathbf{x}), \text{ for } k = 1, \ldots, K.
\end{aligned}
\tag{7.14}
$$

MMSE Based SINR

For user i_k, assuming the interference only from users $i_1, i_2, \ldots, i_{k-1}$, we apply the MMSE detector weights $\mathbf{w}_{i_k}^k$ to (7.14) to select

$$
\begin{aligned}
\mathbf{u}_{i_k} &= \arg\max_{\mathbf{x}\in\mathcal{S}_q(N_t)} \frac{\mathbf{w}_{i_k}^k \mathbf{H}_{i_k}\mathbf{x}}{\displaystyle\sum_{j=1}^{k-1} \left| \mathbf{w}_{i_k}^k \mathbf{H}_{i_j}\mathbf{u}_{i_j} \right|^2 + N_t\sigma^2}, \\
&= \arg\max_{\mathbf{x}\in\mathcal{S}_q(N_t)} \mathcal{M}_{i_k}^k(\mathbf{x}), \text{ for } k = 1, \ldots, K.
\end{aligned}
\tag{7.15}
$$

By letting $\mathbf{H}_{\text{eff}} \triangleq \begin{bmatrix} \mathbf{H}_{i_k}\mathbf{x} & \mathbf{H}_{i_1}\mathbf{u}_{i_1} & \dots & \mathbf{H}_{i_{k-1}}\mathbf{u}_{i_{k-1}} \end{bmatrix} \in \mathbb{C}^{N_r \times k}$, the MMSE weight matrix $\mathbf{W}^k_{\text{mmse}} \in \mathbb{C}^{k \times N_r}$ can be written as

$$\mathbf{W}^k_{\text{mmse}} \triangleq (\mathbf{H}^H_{\text{eff}}\mathbf{H}_{\text{eff}} + N_t\sigma^2\mathbf{I})^{-1}\mathbf{H}^H_{\text{eff}} . \tag{7.16}$$

Therefore, $\mathbf{w}^k_{i_k} \in \mathbb{C}^{1 \times N_r}$ is the normalized version of the first row of $\mathbf{W}^k_{\text{mmse}}$, corresponding to user i_k.

Finding the user order for precoder design: The user order can be randomly chosen. However, to improve the performance, at stage k, we choose the i_k-th user as the one which has the least maximum SINR from the user index set $\mathcal{U}_k = \big\{\{1, 2, \dots, K\} - \{i_1, i_2, \dots, i_{k-1}\}\big\}$. We name this order as *minimum order* (see more detailed discussions about alternative user ordering in Section 7.4).

At the initial stage, we choose the i_1-th user which has the least maximum effective channel power, since we disregard the interference from others. This is because, as the number of stages increases, the number of interference terms increases, which puts more constraints on the selection of precoding vector, yielding a further reduction in SNR of that user. With the user ordering, SEP design requires $\frac{K(K+1)}{2}$ of computations in (7.14). Similar idea applies to the MMSE based scheme. The corresponding pseudocode is given in **Algorithm 7.2**.

To reduce the exponential computation complexity of (7.14), we adopt the LS method in **Algorithm 7.2** to provide sub-optimal solutions to (7.14) prior to deciding the i_k-th user order. To further reduce the complexity of LS method, for user i_k, we use the first stage solution of SEP as the initial solution in the next stage and then update it at each stage.

Overall **Algorithm 7.2** works as follows: In the first stage, the precoding vectors of all the users are computed by maximizing their corresponding SINR using LS method. Then the user with the least SINR is selected and its precoding vector is finalized. In the next stage, the precoding vectors of the users except the selected user in the first stage $\mathcal{U}_2 = \big\{\{1, 2, \dots, K\} - \{i_1\}\big\}$ are computed by maximizing the modified SINR and the user with the least SINR is selected and its precoding vector is finalized. This process continues until precoding vectors of all users are finalized. The complexity order of **Algorithm 7.2** is $\mathcal{O}(K^2 l_p |\mathcal{N}_{d,N_t}(\mathbf{x})|)$.

Algorithm 7.2 The Successive Estimation Precoder

1: **Input:** $\mathbf{H}_1, \mathbf{H}_2, \cdots, \mathbf{H}_K$
2: **for** $k = 1$ **to** K **do**
3:     **for** $l \in \mathcal{U}_k$ **do**
4:         $\mathbf{p}_l \leftarrow \text{LS}(\mathcal{Z}_l^k(\mathbf{x}))$
5:     **end for**
6:     $i_k \leftarrow \underset{l \in \mathcal{U}_k}{\arg\min}\, \mathcal{Z}_l^k(\mathbf{p}_l)$
7:     $\mathbf{u}_{i_k} \leftarrow \mathbf{p}_{i_k}$
8: **end for**
9: **Output:** $\mathbf{u}_1, \mathbf{u}_2, \ldots, \mathbf{u}_K$

7.3.2 The Detector Design

In this subsection, we propose two different detectors: one provides an approximate solution to ML detection and the other is based on successive cancellation. In both designs, we assume that the $\mathbf{u}_i$'s are already made available using computations in Section 7.3.1.

Approximate ML Detector (AMLD)

Given the known received signal $\mathbf{s} \in \mathbb{C}^{N_r \times 1}$ (the received signal at the BS before phase shifters) and assuming that the BS adopts N_r RF chains (the optimal case), the ML detection is given by

$$\hat{\mathbf{x}} = \underset{\mathbf{x} \in \mathcal{A}^K}{\arg\min} \|\mathbf{s} - \tilde{\mathbf{H}}\mathbf{x}\|^2, \tag{7.17}$$

where $\tilde{\mathbf{H}} \triangleq [\tilde{\mathbf{h}}_1, \tilde{\mathbf{h}}_2, \ldots, \tilde{\mathbf{h}}_K] \in \mathbb{C}^{N_r \times K}$, $\hat{\mathbf{x}} = [\hat{x}_1, \hat{x}_2, \ldots, \hat{x}_K]^T$, and $\hat{x}_i$ is the decoded symbol corresponding to user i. Considering

$$\tilde{\mathbf{H}} = \mathbf{Q}\mathbf{R} = \begin{bmatrix} \mathbf{Q}_1 & \mathbf{Q}_2 \end{bmatrix} \begin{bmatrix} \mathbf{R}_1 \\ \mathbf{0} \end{bmatrix}, \tag{7.18}$$

where $\mathbf{Q} \in \mathbb{C}^{N_r \times N_r}$ is a unitary matrix and $\mathbf{R} \in \mathbb{C}^{N_r \times K}$ is an upper triangular matrix with the last $N_r - K$ rows as completely zeros, the ML detection in (7.17) can be rewritten as

$$\begin{aligned} \hat{\mathbf{x}} &= \underset{\mathbf{x} \in \mathcal{A}^K}{\arg\min} \|\mathbf{Q}^H \mathbf{s} - \mathbf{R}\mathbf{x}\|^2, \\ &= \underset{\mathbf{x} \in \mathcal{A}^K}{\arg\min} \|\mathbf{Q}_1^H \mathbf{s} - \mathbf{R}_1 \mathbf{x}\|^2, \end{aligned} \tag{7.19}$$

where $\mathbf{Q}_1 \in \mathbb{C}^{N_r \times K}$ is the matrix with first K columns of $\mathbf{Q}$ and $\mathbf{R}_1 \in \mathbb{C}^{K \times K}$ is the matrix with first K rows of $\mathbf{R}$. From (7.19), we observe that ML detection can also be implemented by using $\mathbf{Q}_1^H \mathbf{s} \in \mathbb{C}^{K \times 1}$ instead of $\mathbf{s} \in \mathbb{C}^{N_r \times 1}$.

Therefore, we apply ML detection in our hybrid beamforming at the BS by i) letting the $\mathbf{v}_j$'s equal to the columns in $\mathbf{Q}_1$ to obtain $\mathbf{Q}_1^H \mathbf{s}$ in analog domain, and ii) applying (7.19) on $\mathbf{Q}_1^H \mathbf{s}$ in digital domain. Unfortunately, the elements of $\mathbf{v}_j$'s have a constant amplitude constraint and cannot be made equal to those of $\mathbf{Q}_1$ which have different amplitudes and phases. To solve this problem, we propose a solution that is based on the following Lemma derived in [81, 82].

Lemma 7.1. *Every element of $\mathbf{Q}_1$ can be written as a sum of two unit amplitude values. That is, (i,j)-th element of $\mathbf{Q}_1$, $e_{i,j}$, can be written as*

$$e_{i,j} = e^{j(\cos^{-1}(a_{i,j}/2) + \theta_{i,j})} + e^{j(-\cos^{-1}(a_{i,j}/2) + \theta_{i,j})}, \qquad (7.20)$$

where, $a_{i,j}$ and $\theta_{i,j}$ are the amplitude and phase of $e_{i,j}$ respectively. ∎

Since a large array of antennas is used in mm-Waves to compensate path-loss, in most of the cases, the value of $a_{i,j}$ is close to 0 and the difference of the angles in (7.20), $2\cos^{-1}(a_{i,j}/2)$, is close to 180^0, i.e., one angle in $[0, \pi)$ and the other in $[\pi, 2\pi)$. Therefore, $[\mathbf{v}_1, \mathbf{v}_2, \ldots, \mathbf{v}_K] = \mathbf{Q}_1$ is implemented in the analog domain with $2N_r K$ high resolution discrete phase shifters, of which $N_r K$ covers the range $[0, \pi)$ and the other $N_r K$ covers the remaining range.

We name it as *approximate ML detection (AMLD)*, since discrete phase shifters are used rather than continuous ones. In Section 7.4, we present the BER performance with different resolutions of phase shifters $(16, 32, 64)$ and show that with high resolution phases shifters, we can approach the optimal performance. Although the performance of AMLD is close to optimal, it requires twice amount (i.e., $2N_r K$) of phase shifters of high resolution, when compared to a regular hybrid beamforming structure. To tackle this problem, in the following subsection, we present a detector which requires much lesser phase shifters of *low resolution* with trade-offs in performance.

Successive Cancellation Detector (SCD)

Similar to the SEP in Section 7.3.1, this detector is also implemented in K stages. Let

$$j_1, \ldots, j_k, \ldots, j_K \in \{1, 2, \ldots, K\}$$

be the *users order* at which the corresponding decoding vectors $\{\mathbf{v}_{j_k}\}_{k=1}^K$ are successively computed. At stage k, we select the detection vector for user j_k as

$$
\begin{aligned}
\mathbf{v}_{j_k} &= \underset{\mathbf{x} \in \mathcal{S}_q(N_r)}{\arg\max} \frac{|\mathbf{x}^H \tilde{\mathbf{h}}_{j_k}|^2}{\displaystyle\sum_{i=k+1}^{K} |\mathbf{x}^H \tilde{\mathbf{h}}_{j_i}|^2 + N_r \sigma^2}, \\
&= \underset{\mathbf{x} \in \mathcal{S}_q(N_r)}{\arg\max} \, \mathcal{D}_{j_k}^k(\mathbf{x}), \text{ for } k = 1, \ldots, K.
\end{aligned}
\tag{7.21}
$$

Note that the interference term in (7.21) only takes into account those users for which decoding vectors are not computed. Similar to (7.13), the computation of (7.21) requires q^{N_r} comparisons, which is impractical for large values of N_r (32, 64). We thus use the local search to find the approximate solution to (7.21) with metric $\mathcal{D}_{j_k}^k(\mathbf{x})$.

Finding user order for detector design: At stage k, we choose user j_k as the one with the highest maximum SINR, i.e., $\underset{l \in \mathcal{V}_k}{\max} \left(\underset{\mathbf{x} \in \mathcal{S}_q(N_r)}{\max} \mathcal{D}_l^k(\mathbf{x}) \right)$, from the user set $\mathcal{V}_k = \{\{1, 2, \ldots, K\} - \{j_1, j_2, \ldots, j_{k-1}\}\}$. We name this order as *maximum order*. As the stage increases, fewer interference terms are involved in (7.21) and also the interference from high SINR users $j_1, \ldots, j_{k-1}$ is removed, leading to improved performance for users with low SINR.

The corresponding pseudocode is given in **Algorithm** 7.3. The LS method is used to find sub-optimal solution to $\underset{\mathbf{x} \in \mathcal{S}_q(N_r)}{\max} \mathcal{D}_l^k(\mathbf{x})$ for a given $l \in \mathcal{V}_k$. The complexity order of this algorithm is $\mathcal{O}(K^2 l_d |\mathcal{N}_{d,N_r}(\mathbf{x})|)$.

Detection Rule: The detector follows the same order as above to detect the transmitted signals $x_{j_1}, \ldots, x_{j_k}, \ldots, x_{j_K}$. In particular, the detection rule for signal x_{j_k} is

$$
\begin{aligned}
\hat{x}_{j_k} &= \underset{z \in \mathcal{A}}{\arg\min} \left| \mathbf{v}_{j_k}^H (\mathbf{s} - \sum_{i=1}^{k-1} \tilde{\mathbf{h}}_{j_i} \hat{x}_{j_i}) - \mathbf{v}_{j_k}^H \tilde{\mathbf{h}}_{j_k} z \right|^2, \\
&= \underset{z \in \mathcal{A}}{\arg\min} \left| y_{j_k} - \sum_{i=1}^{k-1} \mathbf{v}_{j_k}^H \tilde{\mathbf{h}}_{j_i} \hat{x}_{j_i} - \mathbf{v}_{j_k}^H \tilde{\mathbf{h}}_{j_k} z \right|^2,
\end{aligned}
\tag{7.22}
$$

Algorithm 7.3 The Successive Cancellation Detector

1: **Input:** $\tilde{\mathbf{h}}_1, \tilde{\mathbf{h}}_2, \cdots, \tilde{\mathbf{h}}_K$
2: **for** $k = 1$ **to** K **do**
3:      **for** $l \in \mathcal{V}_k$ **do**
4:          $\mathbf{p}_l \leftarrow \text{LS}(\mathcal{D}_l^k(\mathbf{x}))$
5:      **end for**
6:      $j_k \leftarrow \arg\max_{l \in \mathcal{V}_k} \mathcal{D}_l^k(\mathbf{p}_l)$
7:      $\mathbf{v}_{j_k} \leftarrow \mathbf{p}_{j_k}$
8: **end for**
9: **Output:** $\mathbf{v}_1, \mathbf{v}_2, \ldots, \mathbf{v}_K$

---

where $\left(\mathbf{s} - \sum_{i=1}^{k-1} \tilde{\mathbf{h}}_{j_i} \hat{x}_{j_i}\right)$ denotes the received signal after canceling the interference from users $j_1, \cdots, j_{k-1}$. Here, we can see that the interference from users $j_{k+1}, \ldots, j_K$ in $\mathbf{v}_{j_k}^H$ is neglected, simply because we design $\mathbf{v}_{j_k}^H$ based on reducing the interference from these set of users (see (7.21)). Different from [95], our detector uses LS to select $\mathbf{v}_i$ for low-resolution phase shifters, whereas in [95], the detector was designed for high resolution phase shifters by considering only the detection vectors $(\mathbf{v}_i)$ of structure $\mathbf{a}(\phi, N_r)$, i.e., one parameter ϕ decides the entire vector $\mathbf{v}_i$.

7.4 Simulation Results And Discussion

In this section, we first present the sum-rate of the proposed joint precoder and detector design and compare with the upper bound achieved by the point-to-point digital system. We then compare BER performance using our proposed joint design as well as separate precoder and detector designs. We also compare our system performance with the performance of other existing schemes in [95, 96, 98], as well as a fully digital system with ML detection.

7.4.1 Joint Precoder and Detector Design

In simulations, we adopt the following setting: $K = 4$, $N_t = 20$, $N_r = 60$, and QPSK signalling for transmission. The channel between the BS and each user has $L = 3$ propagation paths, where one path is LoS and the other two are NLoS paths. For LoS path, we assume the path gain as $\alpha_1^i = 1$, for $i = 1, \ldots, K$, and for NLoS paths, the path gain as $(\alpha_l^i) \sim \mathcal{CN}(0, \frac{1}{\sqrt{L}})$, where $l = 2, \ldots, L$ and $i = 1, \ldots, K$ [95]. The AoD (θ_l^i) is uniformly distributed in $[0, 2\pi)$ and the AoA (ϕ_l^i) is uniformly distributed in $[-\pi/3, +\pi/3)$ due to sectorization at BS. For LS, we adopt $d = 1$ in (7.8) to list the neighborhood of $\mathbf{x}$.
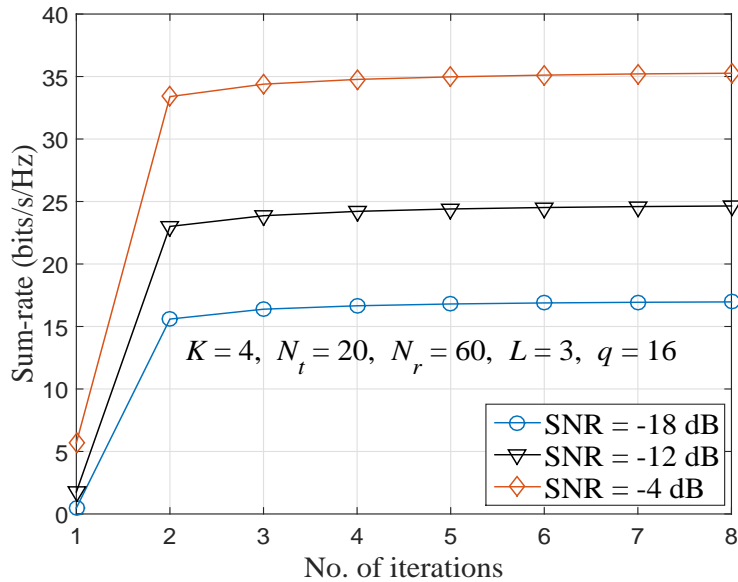
Figure 7.2: The sum-rate of the proposed joint design as a function of number of iterations at different SNR's with $N_t = 20, N_r = 60, K = 4, q = 16$, and $L = 3$.

In Fig. 7.2, we illustrate the variation of the sum-rate of the proposed joint design with the number of iterations at different SNRs for low resolution phase shifter $q = 16$. We observe that the proposed joint design approaches the maximum sum-rate in only 3 iterations. In this simulation, we found the average number of loops in LS are $l_p = 30$ for precoder design and $l_d = 90$ for detector design, respectively.

Figs. 7.3 and 7.4 show the variation of sum-rate as a function of number of iterations and neighborhood size (d) with different number of users ($K = 1, 2, 5, 8$) with $N_t = 20, N_r = 60$, $P/\sigma^2 = -10$ dB, and $L = 3$, respectively. We can see that the joint design is converging in 3 iterations for different number of users. This behavior may be heuristically explained by the fact that the neighborhood size is large enough to avoid the local traps in the search. We also observe that the increase in value of d does not effect the performance as the size of neighborhood is large even with $d = 1$, i.e., $N_t(q - 1)$ or $N_r(q - 1)$. Finally, convergence analysis of the local search algorithm is an interesting open problem that has not been solved yet in the literature.

Figs. 7.5 and 7.6 illustrate the sum-rate of the proposed joint design at different SNRs and for different number of users, respectively, with low resolution phase shifters $q = 4, 8, 16$. In both figures, we also compare the sum-rate of our design with the corresponding upper bound C_{dig} and those of the iterative hybrid precoder and combiner design (HPC) [98]. We observe that the sum-
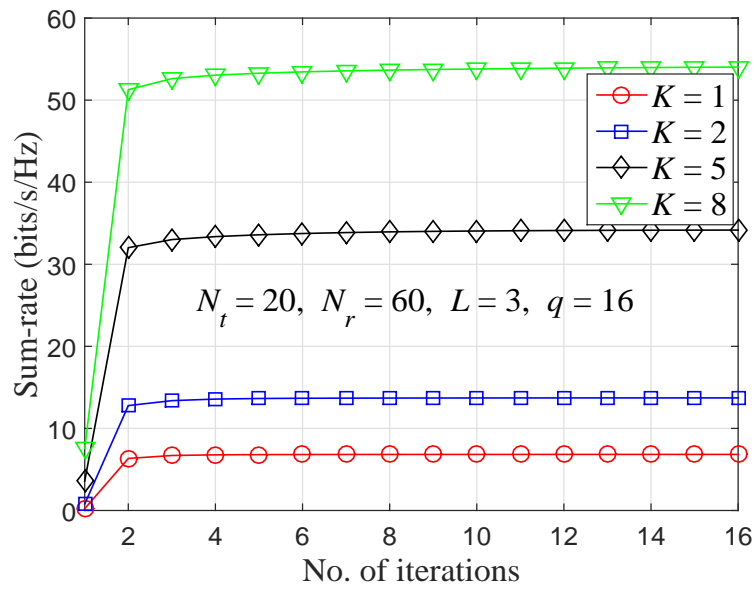
Figure 7.3: The sum-rate of the proposed joint design as a function of number of iterations for different number of users with $N_t = 20, N_r = 60, P/\sigma^2 = -10$ dB, and $L = 3$.
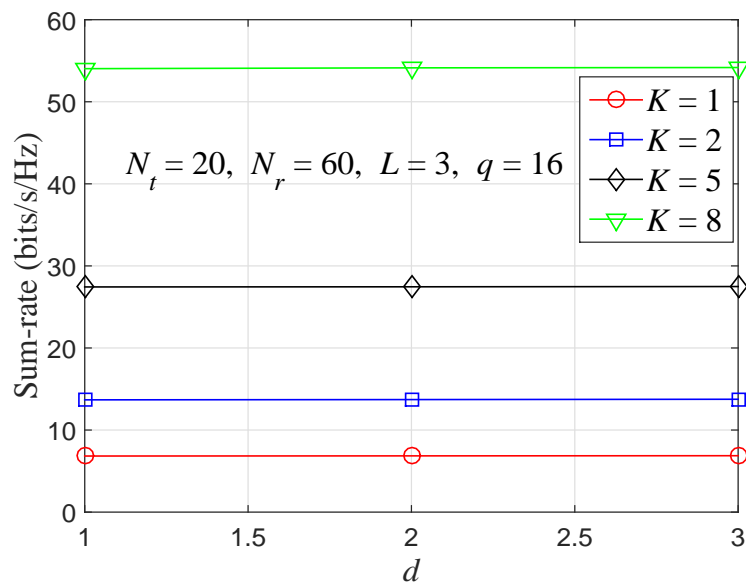
Figure 7.4: The sum-rate of the proposed joint design as a function of neighborhood size d for different number of users (K) with $N_t = 20, N_r = 60, P/\sigma^2 = -10$ dB, and $L = 3$.
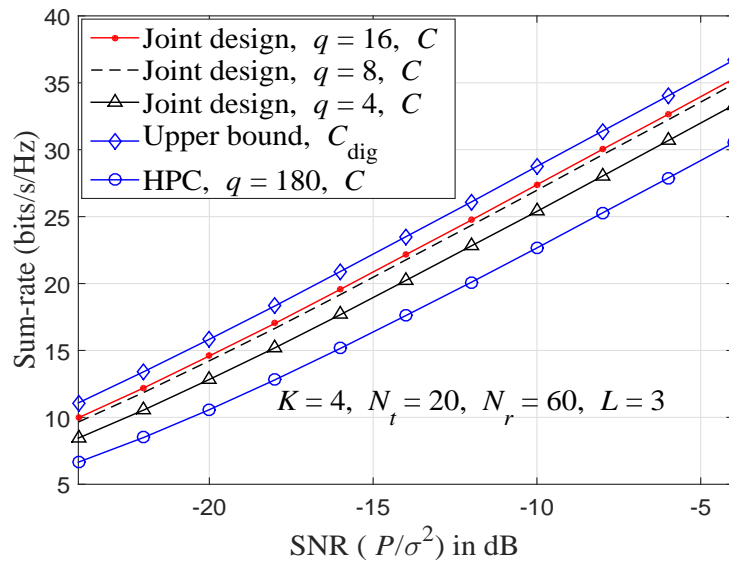
Figure 7.5: The sum-rate of the proposed joint design at different SNR's with $N_t = 20, N_r = 60, K = 4$, and $L = 3$.
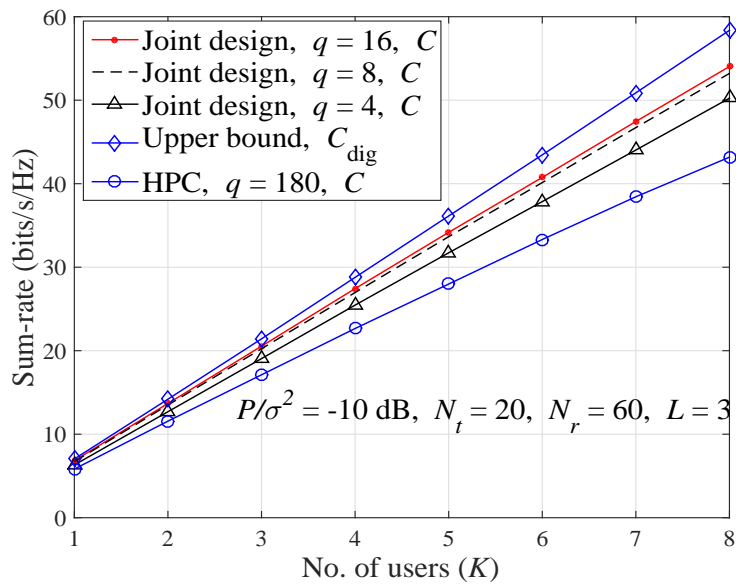
Figure 7.6: The sum-rate of the proposed joint design for different number of users (K) with $N_t = 20, N_r = 60, P/\sigma^2 = -10$ dB, and $L = 3$.

Figure 7.7: The BER performance of CP, SEP-MF, and SEP-MMSE precoders with SCD detector for different values of q with $N_t = 20, N_r = 60, K = 4$, and $L = 3$.

rate of our design outperforms HPC by approximately 5 bits/s/Hz thanks to fully exploitation of all possible combinations for precoders and detectors ($\mathcal{S}_q(N_t)$ and $\mathcal{S}_q(N_r)$) rather than constraining to the form of $\mathbf{a}(\theta, N)$ as in [98]. We also see that our design with $q = 8, 16$ is the closest to the upper bound among all, though the joint design has overall high complexity, as discussed in Section 7.2.1.

7.4.2 Separate Precoder and Detector Design

In the simulations, we consider the settings presented in the subsection 7.4.1. For BER computations, we consider the SNR as E_b/σ^2.

Fig. 7.7 shows the BER of the joint precoder and detector design with low resolution phase shifters of $q = 4, 8, 16$. We observe that the performance improves as q increases. We also see that the joint design with $q = 8$ and $q = 16$ significantly outperforms that with $q = 4$.

Fig. 7.8 compares the BER performance of CP and SEP using MF and MMSE weights for SINR computations, denoted by SEP-MF and SEP-MMSE. We observe that: i) SEP-MMSE outperforms CP and SEP-MF (more than 4 dB gain at 10^{-4} BER), ii) performance improves as q increases, and iii) all the schemes exhibit an error floor at high SNRs due to the residual correlations. This is due to the sparsity of mm-wave channels, where there are more chances of having correlations

Figure 7.8: The BER performance of CP, SEP-MF, and SEP-MMSE precoders with SCD detector for different values of q with $N_t = 20, N_r = 60, K = 4$, and $L = 3$.

between the channels of different users. If the users' channels are highly correlated, the base station fails to recognize different users and cannot detect the signal, even at high SNR with any precoding and detection scheme. This is why there is flooring effect in all plots. Note that this flooring effect occurs at different BERs for different detection schemes, mainly depending on their interference cancellation capability.
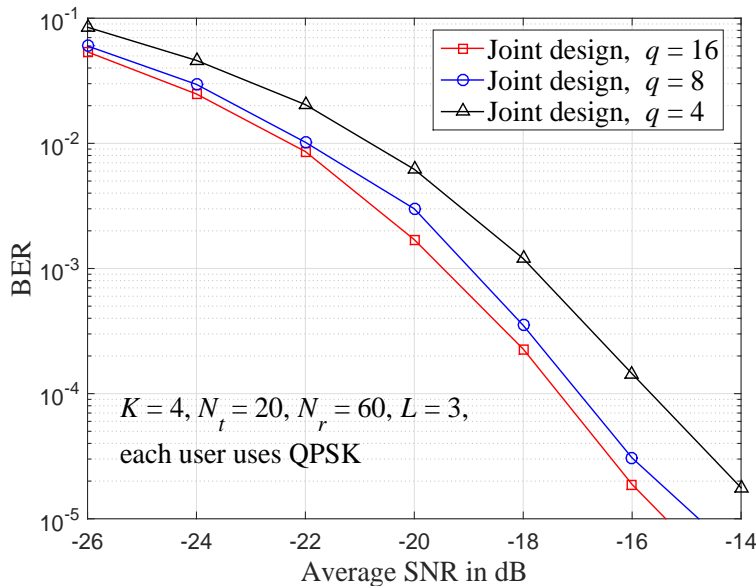
The performance of SEP-MMSE precoder using different user orders is illustrated in Fig. 7.9. The SCD proposed in Section 7.3.2 is used at the BS. Three different precoder users orders are considered: i) maximum order: the user with the largest maximum SINR at every stage (considered $\arg \max$ at line number 6 in **Algorithm 7.2**), ii) fixed order: the user order of $1, 2, \cdots, K$, iii) minimum order: the user with the least maximum SINR at every stage, as in **Algorithm 7.2**. We can observe that, at high SNRs, the precoder with the minimum order performs the best.

In Fig. 7.10, we compare the performance of a fully digital system using ML detection and our system using SEP-MMSE precoder with SCD and AMLD at the receiver, respectively. The AMLD uses 480 $(60 \times 4 \times 2)$ phase shifters of resolutions $q = 16, 32, 64$ with 240 covering the range $[0, \pi)$ and the other 240 covering $[\pi, 2\pi)$. We can see that the BER of AMLD with $q = 64$ is closest to the fully digital performance, when compared to the others, while the SCD achieves reasonably good performance with 240 low resolution phase shifters.
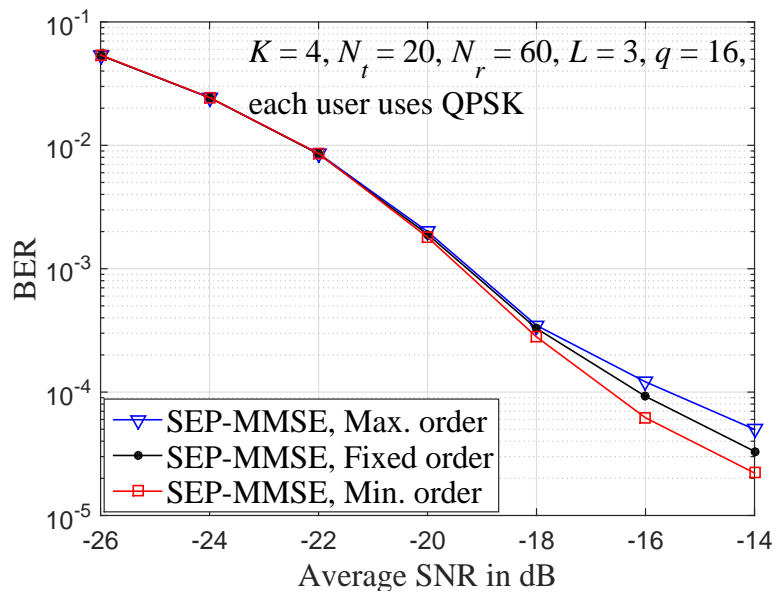
Figure 7.9: The BER performance of SEP-MMSE precoder with SCD detector for different user orders with $N_t = 20, N_r = 60, K = 4$, q = 16 and $L = 3$.

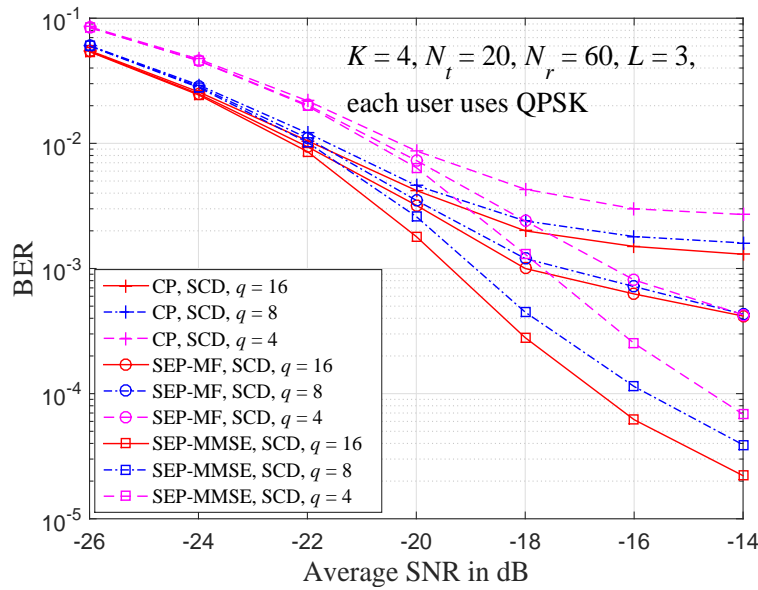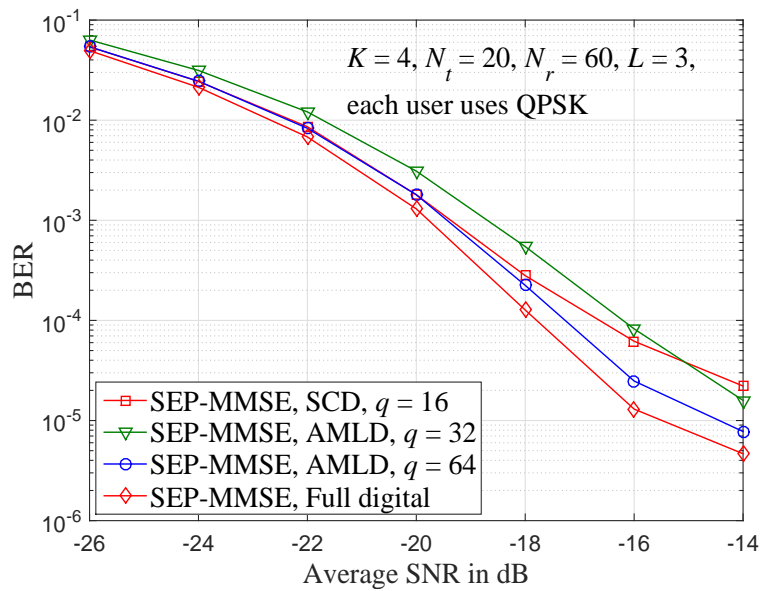
Figure 7.10: The BER performance of SEP-MMSE precoder with SCD and AMLD detectors for different values of q with $N_t = 20, N_r = 60, K = 4$, and $L = 3$.
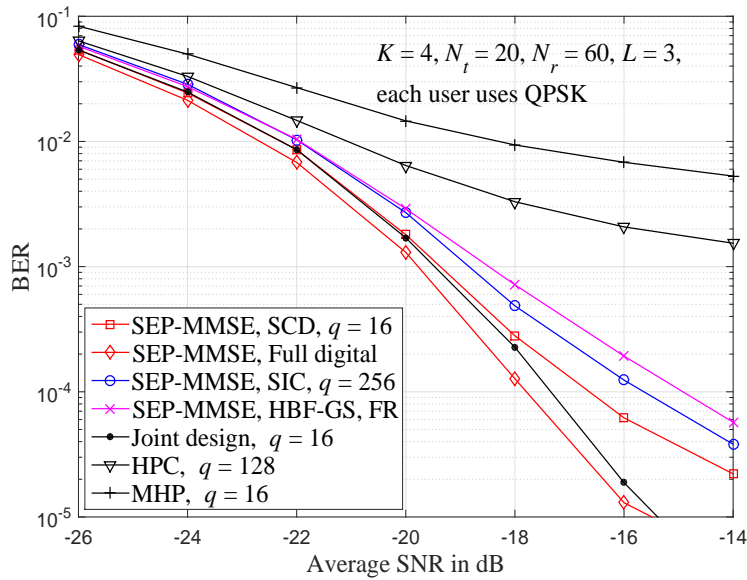
Figure 7.11: The BER performance of SEP-MMSE precoder with SCD detector, SIC, HBF-GS, MHP, and HPC for $N_t = 20, N_r = 60, K = 4$, and $L = 3$.

In Fig. 7.11, we compare the performance of various systems: i) using a SEP-MMSE precoder at transmitter but different detection schemes at receiver: a fully digital one with ML detection, our system using SCD, the systems using the ordered successive interference cancellation (SIC) method in [95], and Gram-Schmidt (HBF-GS) method in [96] for receive beamforming design, ii) two-stage multiuser hybrid precoder (MHP) in [92] , iii) the HPC design in [98], and iv) joint precoder and detector design. Here, we assume that ordered SIC uses 240 phase shifters with $q = 256$ resolution, HBF-SC uses 240 phase shifters of full resolution (FR), i.e., it covers all continuous range of angles, MHP uses $q = 16$ resolution phase shifters, and HPC uses $q = 128$ resolution phase shifters.

Complexity Comparison: The schemes in [95, 96] only design the detector assuming the precoding vectors are already available. The complexity order of both designs is $\mathcal{O}(N_r K^2)$, which is similar to our SCD when $K << N_r$. The HPC design in [98] is a joint precoder and detector design with complexity order $\mathcal{O}(N_r N_t K^2)$, which is also similar to our joint design. Through simulations, we observe the similar average CPU running times for all these methods.

From Fig. 7.11, we see that the joint design performs closely to the fully digital one, and better than all the other designs. We also observe various detector designs together with our SEP-MMSE precoder have better performance than MHP [92] and HPC [98], where an error floor occurs at 10^{-3} BER. This is due to the fact that MHP selects the analog beamforming vectors of a user based on its

own channel and the interference between users is handled only by the digital stage at BS. Further, hybrid precoder and combiner (HPC) design in [98] aims at maximizing the multiuser sum-rate, when a linear MMSE linear detector is adopted at the receiver. The BER of HPC is mainly limited by this linear MMSE detector, while other schemes are non-linear and able to cancel the interference more effectively.

Moreover we see that our SCD detector with low resolution phase shifters ($q = 16$) outperforms the SIC system [95] and HBF-GS [96] with FR phase shifters by 1 dB and 2 dB, respectively, at BER of 10^{-4}. This performance gain is because of the exploration of more combinations for beamforming vectors ($\mathcal{S}_q(N)$) rather than constrained to a particular form of $\mathbf{a}(\theta, N)$.

Chapter 8

Conclusions and Future Directions

In this thesis, we studied two efficient physical layer techniques for the next generation wireless systems, namely, waveform design and mm-Wave systems. In the first part, we investigated several aspects of the recently proposed OTFS modulation, such as OTFS with practical waveforms and channel estimation, and showed that it outperforms the current OFDM system. In the second part, we studied the design of best beamforming weight vectors for the practically feasible low resolution phase shifters for mm-Wave point-to-point and multiuser uplink systems. In the following, we summarize our key contributions and then some possible future directions.

8.1 Contributions

8.1.1 OTFS Modulation

In Chapter 2, we analyzed the input–output relation describing OTFS mod/demod over delay–Doppler channels. We studied in detail the cases of ideal waveforms and rectangular waveforms. In particular, we characterized IDI, ICI, and ISI using sparse representation of the channel in the delay–Doppler domain. A low-complexity yet efficient MP algorithm for joint interference cancellation and symbol detection was proposed, which is suitable for large-scale OTFS with inherent channel sparsity. In the MP algorithm, the ISI and ICI can be cancelled by using appropriate phase shifting, while the IDI can be mitigated by accounting for a small number of significant interference terms only. The proposed MP algorithm can effectively compensate for a wide range of channel Doppler spreads. Moreover, we demonstrated that it is possible to achieve the performance of OTFS

117

with ideal yet *non-realizable* waveforms using *practical* rectangular waveforms. Through simulations, we showed that OTFS has significant error performance gains over OFDM under various communications scenarios including ideal and non-ideal channel estimation, low-latency communications etc.

In Chapter 3, we analyzed the input–output relation of OTFS system for arbitrary pulse-shaping waveforms using a block-circulant matrix decomposition. We showed that the OTFS has a simple sparse input-output relation which enables the use of low-complexity detection algorithms. Simulation results, comparing the error performance of OTFS with different waveforms, showed a tradeoff between out-of-band radiation and BER.

In Chapter 4, we developed embedded pilot-aided OTFS channel estimation schemes. In particular, we arranged pilot, guard, and information symbols in the delay–Doppler grids to suitably avoid interference between pilot and data symbols. We designed such arrangements for OTFS with ideal and rectangular pulses over channels with integer or fractional Doppler paths, respectively. At the receiver, channel estimation was performed based on a threshold method and the estimated channel information was used for data detection via MP algorithm proposed in Chapter 2. We compared by simulations the error performance of OTFS using the proposed channel estimation schemes and OTFS with perfectly known channel information and observed only a marginal performance loss. Further, we showed that OTFS with our channel estimation significantly outperforms OFDM with ideal channel information.

Finally, in Chapter 5, we studied OTFS in static multipath channels and showed that its structure is equivalent to A-OFDM. Further, we derived a necessary and sufficient condition in OTFS to guarantee that all the transmitted symbols experience uniform channel gains, as in CPSC. We applied low-complexity MP detection algorithm in Chapter 2 to OTFS and showed that OTFS with MP detection performs similarly to CPSC, but better than OTFS/A-OFDM with ZF and MMSE detections. We also showed that the performance of OTFS using channel estimation with embedded pilots approaches the performance with ideal channel state information at the receiver.

Table 8.1 briefly summarize the differences between OTFS and OFDM systems.

Parameter	OFDM	OTFS
Transform	Fourier transform	Zak transform
Operating domain	Time–frequency	Delay–Doppler
Maximum PAPR	M	N
CP	$(L-1)N$	$L-1$
Tx complexity	$MN\log_2 M$	$MN\log_2 N$
Rx complexity	$MN\log_2 M$	$MN\log_2 N$
Detector complexity	$\mathcal{O}(NM)$	MP – $\mathcal{O}(n_{\text{iter}}NMPQ)$
Maximum Doppler allowed	$< 10\%$ of Δf	Δf
Diversity gain	1	Almost P (no. of paths)

Table 8.1: Comparison between OFDM and OTFS systems

8.1.2 Millimeter Wave Communications

In Chapter 6, we proposed a hierarchical codebook design for analog beamforming with low resolution phase shifters. The beamforming vectors in our codebook are grouped into multiple levels. At each level, the preferred beamforming vector is constructed to approach the corresponding amplitude beamforming gain mask using a low complexity local search algorithm. Through simulations, we showed that our codebooks with low resolution phase shifters outperform an existing scheme with high resolution phase shifters.

In Chapter 7, we considered a mm-Wave multiuser uplink system for low resolution phase shifters ($q = 4, 8, 16$). We proposed a joint precoder and detector design to maximize the sum-rate of the uplink system. Although the joint design approaches the sum-rate of a fully digital system, the computation complexity to determine the good beamforming vectors is high. Hence, we separately designed precoders and detectors, to provide a tradeoff between complexity and performance. For the precoder designs, the preferred transmit beamforming vectors were chosen to maximize either SNR or SINR of each user, using a low complexity LS method. For detector designs, the receiver beamforming vectors were selected using AMLD and SCD, respectively. Although AMLD has similar performance to the fully digital system, it requires to double the number of phase shifters and a higher phase resolution, when compared to a regular hybrid beamforming receiver. In contrast, the SCD uses only low resolution phase shifters without doubling their number. We showed by

simulations that both joint design and separate designs with low resolution phase shifters outperform the traditional methods using steering vectors as beamforming vectors with high resolution phase shifters.

8.2   Future Directions

We now discuss some of the possible future extensions to the work reported in this thesis.

8.2.1   OTFS Modulation

We analyzed the system model and channel estimation aspects of single input single output (SISO) OTFS system. A list of suggestions for future research are provided below.

- Analyse the theoretical BER and capacity of OTFS with the ideal ML detector and the proposed MP detector. This analysis can also be extended to address the impact of channel estimation errors on the BER performance.

- Study on the effect of hardware impairments on the OTFS system model. This may include CFO, timing synchronization, sampling clock offset, and phase noise.

- Methods to reduce the memory requirement of the proposed MP detection with a compromise in performance as the proposed MP detection has a high memory requirement for larger constellations.

- Hardware implementation of our MP detection using the state-of-the-art processors.

- Extensions of the proposed system to MIMO, multiuser, and massive MIMO cases. This may need investigating the precoding techniques that can be applied in the delay–Doppler plane rather than the current techniques in the time–frequency plane. The precoding techniques may also be used to reduce the detection complexity at the receiver.

- Explore the uses of OTFS in the areas other than communications.

8.2.2 Millimeter Wave Communications

In this thesis, we provided several beamforming design methods based on the local search algorithm for point-to-point and multiuser systems. A list of suggestions for future research are provided below.

- Study on the performance of the proposed methods to other antenna arrangements, such as uniform planar arrays.

- Extension of the proposed method to the mm-Wave multiuser downlink system.

- Theoretical analysis of the proposed method to guarantee the minimum beamforming gains.

- In this work, we consider the frequency flat mm-Wave channel models. However, mm-Wave systems can operate over huge bandwidths for which the channel will be frequency selective. At the same time, OTFS modulation provides a better solution to operate at the frequency selective and high Doppler (doubly dispersive) channels. Finding the optimum beamforming vector designs for the frequency selective mm-Wave systems with OTFS modulation will be very attractive future direction.

Bibliography

[1] Cisco, "Visual networking index: Forecast and trends," White paper, 2018, available: www.Cisco.com. [page 1]

[2] Huawei, "5G a technology vision," White paper, 2013, available: www.Huawei.com. [page 1]

[3] Qualcomm Technologies, Inc., "Qualcomm's 5G vision," White paper, 2014, available: www.Qualcomm.com. [page 1]

[4] A. Osseiran et al., "Scenarios for 5G mobile and wireless communications: The vision of the METIS project," *IEEE Commun. Mag.,* vol. 52, no. 5, pp. 26-35, May 2014. [page 1]

[5] B. Bangerter, S. Talwar, R. Arefi, and K. Stewart, "Networks and devices for the 5G era," *IEEE Commun. Mag.,* vol. 52, no. 2, pp. 90-96, Feb. 2014. [page 1]

[6] F. Boccardi, R. Heath, A. Lozano, T. Marzetta, and P. Popovski, "Five disruptive technology directions for 5G," *IEEE Commun. Mag.,* vol. 52, no. 2, pp. 74-80, Feb. 2014. [page 1]

[7] J. Andrews, S. Buzzi, W. Choi, S. Hanly, A. Lozano, A. Soong, and J. Zhang, "What will 5G be?" *IEEE J. Sel. Areas Commun.,* vol. 32, no. 6, pp. 1065-1082, June 2014. [page 1]

[8] M. Agiwal, A. Roy, and N. Saxena, "Next generation 5G wireless networks: A comprehensive survey," *IEEE Communications Surveys & Tutorials,* vol. 18, no. 3, pp. 1617-1655, Feb. 2016. [page 1]

[9] S. Chen and J. Zhao, "The requirements, challenges, and technologies for 5G of terrestrial mobile telecommunication," *IEEE Commun. Mag.,* vol. 52, no. 5, pp. 36-43, May 2014. [page 1]

[10] A. Gupta and R. K. Jha, "A survey of 5G network: Architecture and emerging technologies," *IEEE Access,* vol. 3, pp. 1206-1232, July 2015. [page 1]

[11] T. S. Rappaport, S. Sun, R. Mayzus, H. Zhao, Y. Azar, K. Wang, G. N. Wong, J. K. Schulz, M. Samimi, and F. Gutierrez, "Millimeter wave mobile communications for 5G cellular: It will work!," *IEEE Access Journal*, vol. 1, pp. 335-349, May 2013. [pages 1, 2, 11]

[12] E. G. Larsson, O. Edfors, F. Tufvesson, and T. L. Marzetta, "Massive MIMO for next generation wireless systems," *IEEE Commun. Mag.,*, vol. 52, no. 2, pp. 186-195, February 2014. [page 1]

[13] T. Wang, J. G. Proakis, E. Masry, and J. R. Zeidler, "Performance degradation of OFDM systems due to Doppler spreading," *IEEE Trans. Wireless Commun.*, vol. 5, no. 6, pp. 1422-1432, June 2006. [page 4]

[14] G. Matz, H. Bölcskei, and F. Hlawatsch, "Time–frequency foundations of communications: Concepts and tools," *IEEE Signal Processing Mag.*, vol. 30, no. 6, pp. 87-96, 2013. [page 4]

[15] K. Liu, T. Kadous, and A. M. Sayeed, "Orthogonal time–frequency signaling over doubly dispersive channels," *IEEE Trans. Inf. Theory*, vol. 50, no. 11, pp. 2583-2603, 2004. [page 4]

[16] A. Fish, S. Gurevich, R. Hadani, A. M. Sayeed, and O. Schwartz, "Delay-Doppler channel estimation in almost linear complexity," *IEEE Trans. Inf. Theory*, vol. 59, no. 11, pp. 7632-7644, Nov 2013. [page 49]

[17] R. Hadani, S. Rakib, M. Tsatsanis, A. Monk, A. J. Goldsmith, A. F. Molisch, and R. Calderbank, "Orthogonal time frequency space modulation," in *Proc. IEEE Wireless Communications and Networking Conference (WCNC)*, San Francisco, CA, USA, March 2017. [pages 2, 5, 6, 8, 21, 23, 25, 48, 54, 73]

[18] R. Hadani, S. Rakib, S. Kons, M. Tsatsanis, A. Monk, C. Ibars, J. Delfeld, Y. Hebron, A. J. Goldsmith, A.F. Molisch, and R. Calderbank, "Orthogonal time frequency space modulation," Available online: https://arxiv.org/pdf/1808.00519.pdf. [pages 5, 6, 21, 25, 26, 48, 54]

[19] R. Hadani, and A. Monk, "OTFS: A new generation of modulation addressing the challenges of 5G," *OTFS Physics White Paper*, Cohere Technologies, 7 Feb. 2018. Available online: https://arxiv.org/pdf/1802.02623.pdf. [pages 5, 8, 9]

[20] R. Hadani, S. Rakib, A. F. Molisch, C. Ibars, A. Monk, M. Tsatsanis, J. Delfeld, A. Goldsmith, and R. Calderbank, "Orthogonal time frequency space (OTFS) modulation for millimeter-wave communications systems," in *Proc. 2017 IEEE MTT-S International Microwave Symposium (IMS),* Honololu, HI, USA, June 2017. [page 5]

[21] W. Jakes, *Microwave mobile communications.* New York, NY: Wiley, 1974. [pages 6, 23]

[22] L. Li, H. Wei, Y. Huang, Y. Yao, W. Ling, G. Chen, P. Li, and Y. Cai, "A simple two-stage equalizer with simplified orthogonal time frequency space modulation over rapidly time-varying channels," available online: https://arxiv.org/abs/1709.02505. [pages 8, 9, 48]

[23] A. Farhang, A. RezazadehReyhani, L. E. Doyle, and B. Farhang-Boroujeny, "Low complexity modem structure for OFDM-based orthogonal time frequency space modulation," *IEEE Wireless Commun. Lett.,* vol. 7, no. 3, pp. 344-347, June 2018. [pages 8, 9, 48]

[24] A. RezazadehReyhani, A. Farhang, M. Ji, R. R. Chen, and B. Farhang-Boroujeny, "Analysis of discrete-time MIMO OFDM-based orthogonal time frequency space modulation," in *Proc. 2018 IEEE International Conference on Communications (ICC),* Kansas City, MO, USA, May 2018. [pages 8, 9, 48]

[25] P. Som, T. Datta, N. Srinidhi, A. Chockalingam, and B. S. Rajan, "Low-complexity detection in large-dimension MIMO-ISI channels using graphical models," *IEEE J. Sel. Topics Signal Process.,* vol. 5, no. 8, pp. 1497–1511, Dec. 2011. [pages 10, 35]

[26] W. Mecklenbrauker, *A tutorial on non-parametric bilinear time–frequency signal rtepresentations*, Time and Frequency Representation of Signals and Systems (Eds. G Longo and B. Picinbono), vol. 309, pp. 11-68, 1989. [page 23]

[27] D. N. C. Tse and P. Viswanath, *Fundamentals of Wireless Communications.* Cambridge, U.K.: Cambridge Univ. Press, 2005. [pages 1, 24]

[28] A. Goldsmith, *Wireless Communications.* Cambridge, U.K.: Cambridge Univ. Press, 2005. [pages 1, 102]

[29] F. Hlawatsch and G. Matz, *Wireless Communications Over Rapidly Time-Varying Channels.* Amsterdam: Academic, 2011. [pages 2, 4, 6, 8]

[30] W. Kozek and A. F. Molisch, "Nonorthogonal pulseshapes for multicarrier communications in doubly dispersive channels," *IEEE J. Select. Areas Commun.,* vol. 16, no. 8, pp. 1579-1589, Aug. 1998. [page 25]

[31] G. Durisi, U. Schuster, H. Bölcskei, and S. Shamai, "Noncoherent capacity of underspread fading channels," *IEEE Trans. Inf. Theory,* vol. 56, no. 1, pp. 367-395, Jan. 2010. [pages 4, 25]

[32] M. Pretti, "A message passing algorithm with damping," *J. Stat. Mech.: Theory and Experiment,* P11008, Nov. 2005. [page 37]

[33] Y. Zhao and S. Haggman, "Sensitivity to Doppler shift and carrier frequency errors in OFDM systems-the consequences and solutions," in *Proc. IEEE Vehicular Technology Conf.*, Atlanta, GA, USA, April 1996. [page 39]

[34] T. Yoo and A. Goldsmith, "Capacity of fading MIMO channels with channel estimation error," in *Proc. IEEE International Conference on Communications (ICC),* Paris, France, vol. 2, June 2004. [page 46]

[35] E. LTE, "Evolved universal terrestrial radio access (E-UTRA); base station (BS) radio transmission and reception (3GPP TS 36.104 version 8.6. 0 release 8), July 2009," ETSI TS, vol. 136, no. 104, p. V8. [pages 39, 56, 65]

[36] T. Zemen, M. Hofer, and D. Loeschenbrand, "Low-complexity equalization for orthogonal time and frequency signaling (OTFS)," available online: https://arxiv.org/pdf/1710.09916.pdf. [pages 8, 48]

[37] T. Zemen, M. Hofer, D. Loeschenbrand, and C. Pacher, "Iterative detection for orthogonal precoding in doubly selective channels," available online: https://arxiv.org/pdf/1710.09912.pdf. [pages 8, 48]

[38] H. Bölcskei, P. Duhamel, and R. Hleiss, "Orthogonalization of OFDM/OQAM pulse shaping filters using the discrete Zak transform," *Signal Processing (Elsevier),* vol. 83, pp, 1379-1391, 2003. [page 4]

[39] G. Durisi, V. I. Morgenshtern, H. Bölcskei, U. G. Schuster, and S. Shamai (Shitz), "Information Theory of Underspread WSSUS Channels," in *Wireless Communications over Rapidly Time-Varying Channels,* Amsterdam:Academic, 2011. [page 4]

[40] P. J. Davis, *Circulant Matrices.* New York, NY:Chelsea Publ, 1994. [pages 51, 52, 76]

[41] D. Slepian, "Prolate spheroidal wave functions, Fourier analysis, and uncertainty — V: The discrete case," *Bell System Technical Journal,* vol. 57, no. 5, pp. 1371-1430, May-June 1978. [page 55]

[42] K. R. Murali and A. Chockalingam, "On OTFS modulation for high-Doppler fading channels," in *Proc. ITA'2018,* San Diego, Feb. 2018. [page 8]

[43] M. K. Ramachandran and A. Chockalingam, "MIMO-OTFS in high-Doppler fading channels: Signal detection and channel estimation," available online: https://arxiv.org/abs/1805.02209. [pages 8, 9]

[44] R. Hadani and S. Rakib. "OTFS methods of data channel characterization and uses thereof." U.S. Patent 9 444 514 B2, Sept. 13, 2016. [page 59]

[45] A. Monk, R. Hadani, M. Tsatsanis, and S. Rakib, "OTFS - Orthogonal time frequency space: A novel modulation technique meeting 5G high mobility and massive MIMO challenges." Technical report. Available online: https://arxiv.org/ftp/arxiv/papers/1608/1608.02993.pdf. [pages 60, 61]

[46] J. Zhang, A. D. S. Jayalath, and Y. Chen, "Asymmetric OFDM systems based on layered FFT structure," *IEEE Signal Process. Lett.,* vol. 14, no. 11, pp. 812-815, Nov. 2007. [pages iii, 11, 72, 74, 75]

[47] L. Luo, J. Zhang, and Z. Shi, "BER analysis for asymmetric OFDM systems," in *Proc. 2008 IEEE Global Telecommunications Conference (GLOBECOM),* New Orleans, LO, USA, 2008. [pages 11, 75]

[48] A. Nimr, M. Chafii, M. Matthe, and G. Fettweis, "Extended GFDM framework: OTFS and GFDM comparison," available online: https://arxiv.org/pdf/1808.01161.pdf. [pages 8, 9]

[49] A. M. Sayeed and B. Aazhang, "Joint multipath-Doppler diversity in mobile wireless communications," *IEEE Trans. Commun.,* vol. 47, pp. 123-132, Jan. 1999. [page 4]

[50] S. Bhashyam, A. M. Sayeed, and B. Aazhang, "Time-selective signaling and reception for communication over multipath fading channels," *IEEE Trans. Commun.,* vol. 48, pp. 83-94, Jan. 2000. [page 4]

[51] X. Ma and G. B. Giannakis, "Maximum-diversity transmissions over doubly selective wireless channels," *IEEE Trans. Inf. Theory,* vol. 49, no. 7, July 2003, pp. 1832-1840. [page 4]

[52] Z. Wang and G. B. Giannakis, "Linearly precoded or coded OFDM for wireless channels?," in *Proc. 3rd Workshop Signal Processing Advances in Wireless Communications,* Taiwan, ROC, Mar. 2001. [page 4]

[53] T. S. Rappaport, R. W. Heath, R. C. Daniels, and J. N. Murdock, *Millimeter Wave Wireless Communications.* Prentice Hall, 2015. [page 11]

[54] S. Rangan, T. Rappaport, and E. Erkip, "Millimeter-wave cellular wireless networks: Potentials and challenges," in *Proc. of the IEEE,* vol. 102, no. 3, pp. 366-385, Mar. 2014. [page 11]

[55] H. Zhang, S. Venkateswaran, and U. Madhow, "Channel modeling and MIMO capacity for outdoor millimeter wave links," in *Proc. IEEE Wireless Communications and Networking Conference (WCNC),* pp. 1-6, April 2010. [page 11]

[56] IEEE 802.11ad-2012, " IEEE Standard for information technology - telecommunications and information exchange between systems - local and metropolitan area networks - specific requirements - part 11: wireless LAN medium access control (MAC) and physical layer (PHY) specifications - amendment 3: enhancements for very high throughput in the 60 GHz band," *IEEE*, Dec. 2012. [page 11]

[57] J. Wells, "Faster than fiber: The future of multi-G/s wireless," *IEEE Microwave Mag.,* vol. 10, no. 3, pp. 104-112, May 2009. [page 11]

[58] T. S. Rappaport, J. Murdock, and F. Gutierrez, Jr., "State of the art in 60-GHz integrated circuits and systems for wireless communications," in *Proc. of the IEEE,* vol. 99, no. 8, pp. 1390-1436, Aug. 2011. [page 11]

[59] M. Bensebti, J. P. McGeehan, and M. A. Beach, "Indoor multipath radio propagation measurements and characterization at 60 GHz," in *1991 European Microwave Conf.,* vol. 2, pp. 1217-1222, Sept. 1991. [page 11]

[60] F. Gutierrez, K. Parrish, and T. S. Rappaport, "On-chip integrated antenna structures in CMOS for 60 GHz WPAN systems," *IIEEE J. Sel. Areas Commun.,* vol. 27, no. 8, pp. 1367-1378, Oct. 2009. [page 11]

[61] S. Kutty and D. Sen, "Beamforming for millimeter wave communications: An inclusive survey," *IEEE Communications Surveys and Tutorials,* vol. 18, no. 2, pp. 949-973, May 2016. [page 11]

[62] M. R. Akdeniz et al., "Millimeter wave channel modeling and cellular capacity evaluation," *IEEE J. Sel. Areas Commun.,* vol. 32, no. 6, pp. 1164-1179, Jun. 2014. [page 11]

[63] J. Wang, Z. Lan, C. Pyo, T. Baykas, C. Sum, M. Rahman, J. Gao, R. Funada, F. Kojima, and H. Harada, "Beam codebook based beamforming protocol for multi-Gbps millimeter-wave WPAN systems," *IEEE J. Sel. Areas Commun.,* vol. 27, no. 8, pp. 1390-1399, Oct. 2009. [pages 12, 13, 14, 15]

[64] Y. Peng, Y. Li, and P. Wang, "An enhanced channel estimation method for millimeter wave systems with massive antenna arrays," *IEEE Commun. Lett.,* vol. 19, no. 9, pp. 1592-1595, Sept. 2015. [page 12]

[65] Z. Xiao, L. Bai, and J. Choi, "Iterative joint beamforming training with constant-amplitude phased arrays in millimeter-wave communications," *IEEE Commun. Lett.,* vol. 18, no. 5, pp. 829-832, May 2014. [page 12]

[66] O. El Ayach, S. Rajagopal, S. Abu-Surra, Z. Pi, and R. Heath, "Spatially sparse precoding in millimeter wave MIMO systems," *IEEE Trans. Wireless Commun.,* vol. 13, no. 3, pp. 1499-1513, March 2014. [page 12]

[67] L. Chen, Y. Yang, X. Chen, and W. Wang, "Multi-stage beamforming codebook for 60GHz WPAN," in *2011 6th International ICST Conference on Communications and Networking in China (CHINACOM),* Harbin, China, pp. 361-365, Aug. 2011. [pages 12, 14, 15]

[68] S. Hur, T. Kim, D. J. Love, J. V. Krogmeier, T. A. Thomas, and A. Ghosh, "Millimeter wave beamforming for wireless backhaul and access in small cell networks," *IEEE Trans. Commun.,* vol. 61, no. 10, pp. 4391-4403, Oct. 2013. [page 12]

[69] T. He and Z. Xiao, "Sub optimal beam search algorithm and codebook design for millimeter-wave communications," in *Mobile Networks and Applications,* pp. 86-97, Jan. 2015. [pages 14, 15]

[70] Z. Xiao, T. He, P. Xia, and X. Xia, "Hierarchical codebook design for beamforming training in millimeter-wave communication," *IEEE Trans. Wireless Commun.,* vol. 15, no. 5, pp. 3380-3392, May 2016. [pages 12, 14, 15, 88, 89, 90, 92]

[71] A. Alkhateeb, O. E. Ayach, G. Leus, and R. W. Heath, "Channel estimation and hybrid precoding for millimeter wave cellular systems," *IEEE J. Sel. Topics Signal Process.,* vol. 8, no. 5, pp. 831-846, Oct. 2014. [pages 12, 14, 15, 84, 87, 89, 96]

[72] J. Lee, G. Gil, and Y. Lee, "Exploiting spatial sparsity for estimating channels of hybrid MIMO systems in millimeter wave communications," in *Proc. IEEE GLOBECOM Symp.,* Austin, TX, pp. 3326-3331, Dec. 2014. [page 14]

[73] N. Celik, et al., "Implementation and experimental verification of a smart antenna system operating at 60GHz band," *IEEE Trans. Antennas Propagat.,* vol. 56, no. 9, pp. 2790-2800, Sept. 2008. [pages 13, 14, 84]

[74] R. Mendez-Rial et al., "Channel estimation and hybrid combining for mmWave: Phase shifters or switches?," *IEEE J. Sel. Topics Signal Process.,* vol. 8, no. 5, pp. 831-846, Oct. 2014. [page 13]

[75] Yu Yue, B. Yan, and R. Xu, "A millimeter-wave 4-bit digital phase shifter", in *2005 Asia-Pacific Microwave Conference Proceedings,* vol. 2, Dec. 2005. [page 12]

[76] S. Mohammed and E. Larsson, "Constant-envelope multi-user precoding for frequency-selective massive MIMO systems", *IEEE Wireless Commun. Lett.,* vol. 2, no. 5, pp. 547-550, Oct. 2013. [page 88]

[77] Z. Xiao, P. Xia, and X. Xia, "Codebook design for millimeter-wave channel estimation with hybrid precoding structure," *IEEE Trans. Wireless Commun.,* vol. 16, no. 1, pp. 141-153, Jan. 2017. [page 16]

[78] S. Kutty and D. Sen, "Beamforming for millimeter wave communications: An inclusive survey," *IEEE Commun. Surveys Tuts.,* vol. 18, no. 2, pp. 949-973, May 2016. [pages 12, 15]

[79] J. Roderick, H. Krishnaswamy, K. Newton, and H. Hashemi, "Silicon-based ultra-wideband beam-forming," *in IEEE J. Solid-State Circuits,* vol. 41, no. 8, pp. 1726-1739, Aug. 2006. [page 12]

[80] Z. Yonghong, F. Zhenghe, and F. Yong, "Ka-band 4-bit phase shifter with low phase deviation," in *Proc. International Conference on Microwave and Millimeter Wave Technology,* pp. 382-385, Aug. 2004. [page 12]

[81] F. Sohrabi and W. Yu, "Hybrid digital and analog beamforming design for large-scale antenna arrays," *IEEE J. Sel. Topics Signal Process.,* vol. 10, no. 3, pp. 501-513, April 2016. [page 106]

[82] T. E. Bogale, L. B. Le, A. Haghighat, and L. Vadndendorpe, "On the number of RF chains and phase shifters, and scheduling design with hybrid analog-digital beamforming," *IEEE Trans. Wireless Commun.,* vol. 15, no 5, pp. 3311-3326, May 2016. [page 106]

[83] R. Rajashekar and L. Hanzo, "Iterative matrix decomposition aided block diagonalization for mm-Wave multiuser MIMO systems," *IEEE Trans. Wireless Commun.,* vol. 16, no. 3, pp. 1372-1384, March 2017. [page 96]

[84] R. Rajashekar and L. Hanzo, "User selection algorithms for block diagonalization aided multiuser downlink mm-Wave communication," *IEEE Access,* vol. 5, pp. 5760-5772, March 2017. [page 96]

[85] O. El Ayach, S. Rajagopal, S. Abu-Surra, Z. Pi, and R. Heath, "Spatially sparse precoding in millimeter wave MIMO systems," *IEEE Trans. Wireless Commun.,* vol. 13, no. 3, pp. 1499-1513, March 2014. [pages 12, 15, 99]

[86] W. Ni, X. Dong, and W. S. Lu, "Near-optimal hybrid processing for massive MIMO systems via matrix decomposition," *IEEE Trans. Signal Process.,* vol. 65, no. 15, pp. 3922-3933, Aug. 2017. [page 16]

[87] R. Rajashekar and L. Hanzo, "Hybrid beamforming in mm-Wave MIMO systems having a finite input alphabet," *IEEE Trans. Commun.,* vol. 64, no. 8, pp. 3337-3349, Aug. 2016. [page 16]

[88] X. Gao, L. Dai, C. Yuen, and Z. Wang, "Turbo-like beamforming based on tabu search algorithm for millimeter-wave massive MIMO systems," *IEEE Trans. Veh. Technol.,* vol. 65, no. 7, pp. 5731-5737, Jul. 2016. [page 99]

[89] C.-B. Chae, D. Mazzarese, T. Inoue, and R. Heath, "Coordinated beamforming for the multiuser MIMO broadcast channel with limited feedforward," *IEEE Trans. Signal Process.,* vol. 56, no. 12, pp. 6044-6056, Dec. 2008. [page 99]

[90] J. Choi, "Beam selection in mm-Wave multiuser MIMO systems using compressive sensing," *IEEE Trans. Commun.,* vol. 63, no. 8, pp. 2936–2947, Aug. 2015. [page 16]

[91] W. Rhee, W. Yu, and J. M. Cioffi, "The optimality of beamforming in uplink multiuser wireless systems," *IEEE Trans. Wireless Commun.,* vol. 3, no. 1, pp. 86-96, Jan. 2004. [page 98]

[92] A. Alkhateeb, G. Leus, and R. W. Heath, "Limited feedback hybrid precoding for multi-user millimeter wave systems," *IEEE Trans. Wireless Commun.,* vol. 14, no. 11, pp. 6481-6494, Nov. 2015. [pages 16, 115]

[93] G. Lee, Y. Sung, and J. Seo, "Randomly-directional beamforming in millimeter-wave multiuser MISO downlink," *IEEE Trans. Wireless Commun.,* vol. 15, no. 2, pp. 1086-1100, Feb. 2016. [pages 16, 98]

[94] X. Zhu, Z. Wang, L. Dai, and Q. Wang, "Adaptive hybrid precoding for multiuser massive MIMO," *IEEE Commun. Lett.,* vol. 20, no. 4, pp. 776-779, April 2016. [page 16]

[95] J. Choi, "Analog beamforming for low-complexity multiuser detection in mm-Wave systems," *IEEE Trans. Veh. Technol.,* vol. 65, no. 8, pp. 6747-6752, Aug. 2016. [pages 16, 17, 108, 115, 116]

[96] J. Li, L. Xiao, X. Xu, and S. Zhou, "Robust and low complexity hybrid beamforming for uplink multiuser mmwave MIMO systems," *IEEE Commun. Lett.,* vol. 20, no. 6, pp. 1140-1143, June 2016. [pages 16, 17, 98, 108, 115, 116]

[97] Z. Gao, C. Hu, L. Dai, and Z. Wang, "Channel estimation for millimeter-wave massive MIMO with hybrid precoding over frequency-selective fading channels," *IEEE Commun. Lett.,* vol. 20, no. 6, pp. 1259-1262, June 2016. [page 96]

[98] Z. Wang, M. Li, X. Tian, and Q. Liu, "Iterative hybrid precoder and combiner design for mmwave multiuser MIMO systems," *IEEE Commun. Lett.,* vol. 21, no. 7, pp. 1581-1584, July 2017. [pages 16, 17, 98, 108, 109, 112, 115, 116]

Appendix A

Proofs for Chapter 2

A.1   Proof of Theorem 2.1: OTFS Input–Output Relation in Time–Frequency Domain

The received signal after Wigner transform $Y(t, f)$, from (2.4), can be written as in (A.1). It can be further expanded as in (A.2) and (A.3) using the transmitted signal $s(t)$ in (2.3) and some re-ordering of summations and integrations. Therefore, the sampled version of $Y(t, f)$, i.e., $Y[n, m]$, can be written as

$$Y[n, m] = \sum_{n'=0}^{N-1} \sum_{m'=0}^{M-1} X[n', m'] H_{n,m}[n', m'],$$

where $H_{n,m}[n', m']$ is given in (A.4). By applying the change of variable $t' - \tau - n'T \to t''$ in the inner integral and some simple algebraic calculations, we can write $H_{n,m}[n', m']$ as in (A.5) and (A.6), respectively. Finally, we obtain $H_{n,m}[n', m']$ as in (A.7), by replacing the square bracket in (A.6) with cross-ambiguity function in (2.1), which completes the proof.

$$Y(t, f) = \int_{t'} g_{\text{rx}}^*(t' - t) \left[\int_{\tau} \int_{\nu} h(\tau, \nu) s(t' - \tau) e^{j2\pi\nu(t'-\tau)} d\tau d\nu \right] e^{-j2\pi f(t'-t)} dt' \qquad \text{(A.1)}$$

$$= \int_{t'} g_{\text{rx}}^*(t' - t) \left[\int_{\tau} \int_{\nu} h(\tau, \nu) \left\{ \sum_{n'=0}^{N-1} \sum_{m'=0}^{M-1} X[n', m'] g_{\text{tx}}(t' - \tau - n'T) e^{j2\pi m'\Delta f(t'-\tau-n'T)} \right\} \right.$$
$$\left. e^{j2\pi\nu(t'-\tau)} d\tau d\nu \right] e^{-j2\pi f(t'-t)} dt'. \quad \text{(A.2)}$$

133

$$= \sum_{n'=0}^{N-1}\sum_{m'=0}^{M-1} X[n',m']\left[\int_\tau \int_\nu h(\tau,\nu)\left\{\int_{t'} g_{\text{rx}}^*(t'-t)g_{\text{tx}}(t'-\tau-n'T)e^{j2\pi m'\Delta f(t'-\tau-n'T)}\right.\right.$$
$$\left.\left. e^{j2\pi \nu(t'-\tau)}e^{-j2\pi f(t'-t)}dt'\right\}d\tau d\nu\right]. \quad \text{(A.3)}$$

$$H_{n,m}[n',m'] = \int_\tau \int_\nu h(\tau,\nu)\left[\int_{t'} g_{\text{rx}}^*(t'-nT)g_{\text{tx}}(t'-\tau-n'T)e^{j2\pi m'\Delta f(t'-\tau-n'T)}e^{j2\pi \nu(t'-\tau)}\right.$$
$$\left. e^{-j2\pi m\Delta f(t'-nT)}dt'\right]d\tau d\nu \quad \text{(A.4)}$$

$$= \int_\tau \int_\nu h(\tau,\nu)\left[\int_{t''} g_{\text{rx}}^*(t''-(n-n')T+\tau)g_{\text{tx}}(t'')e^{j2\pi m'\Delta f t''}e^{j2\pi \nu(t''+n'T)}\right.$$
$$\left. e^{-j2\pi m\Delta f(t''+(n-n')T+\tau)}dt''\right]d\tau d\nu \quad \text{(A.5)}$$

$$= \int_\tau \int_\nu h(\tau,\nu)\left[\int_{t''} g_{\text{rx}}^*(t''-(n-n')T+\tau)g_{\text{tx}}(t'')e^{-j2\pi((m-m')\Delta f-\nu)(t''-(n-n')T+\tau)}dt''\right]$$
$$e^{j2\pi(\nu+m'\Delta f)((n-n')T-\tau)}e^{j2\pi \nu n'T}d\tau d\nu \quad \text{(A.6)}$$

$$= \int_\tau \int_\nu h(\tau,\nu)A_{g_{\text{rx}},g_{\text{tx}}}((n-n')T-\tau,(m-m')\Delta f-\nu)e^{j2\pi(\nu+m'\Delta f)((n-n')T-\tau)}e^{j2\pi \nu n'T}d\tau d\nu. \quad \text{(A.7)}$$

$$y[k,l] = \frac{1}{NM}\sum_{n=0}^{N-1}\sum_{m=0}^{M-1} H_{n,m}[n,m]\left[\sum_{k'=0}^{N-1}\sum_{l'=0}^{M-1} x[k',l']e^{j2\pi\left(\frac{nk'}{N}-\frac{ml'}{M}\right)}\right]e^{-j2\pi\left(\frac{nk}{N}-\frac{ml}{M}\right)} \quad \text{(A.8)}$$

$$= \frac{1}{NM}\sum_{k'=0}^{N-1}\sum_{l'=0}^{M-1} x[k',l']\left[\sum_{n=0}^{N-1}\sum_{m=0}^{M-1} H_{n,m}[n,m]e^{-j2\pi nT\left(\frac{k-k'}{NT}\right)}e^{j2\pi m\Delta f\left(\frac{l-l'}{M\Delta f}\right)}\right] \quad \text{(A.9)}$$

$$= \frac{1}{NM}\sum_{k'=0}^{N-1}\sum_{l'=0}^{M-1} x[k',l']h_w[k-k',l-l']. \quad \text{(A.10)}$$

$$h_w(\nu,\tau) = \sum_{n=0}^{N-1}\sum_{m=0}^{M-1}\left[\int_{\tau'}\int_{\nu'} h(\tau',\nu')e^{j2\pi\nu'nT}e^{-j2\pi(\nu'+m\Delta f)\tau'}d\tau'd\nu'\right]e^{-j2\pi nT\nu}e^{j2\pi m\Delta f\tau} \quad \text{(A.11)}$$

$$= \int_{\tau'}\int_{\nu'} h(\tau',\nu')\left[\sum_{n=0}^{N-1}\sum_{m=0}^{M-1} e^{-j2\pi(\nu-\nu')nT}e^{j2\pi(\tau-\tau')m\Delta f}\right]e^{-j2\pi\tau'\nu'}d\tau'd\nu' \quad \text{(A.12)}$$

$$= \int_{\tau'}\int_{\nu'} h(\tau',\nu')w(\nu-\nu',\tau-\tau')e^{-j2\pi\tau'\nu'}d\tau'd\nu'. \quad \text{(A.13)}$$

$$y[k,l] = \frac{1}{\sqrt{NM}} \sum_{n=0}^{N-1} \sum_{m=0}^{M-1} \left[\sum_{m'=0}^{M-1} H_{n,m}[n,m']X[n,m'] + \sum_{m'=0}^{M-1} H_{n,m}[n-1,m']X[n-1,m'] \right]$$
$$e^{-j2\pi\left(\frac{nk}{N} - \frac{ml}{M}\right)}.$$

(A.14)

$$y_{\text{ici}}[k,l] = \frac{1}{NM} \sum_{n=0}^{N-1} \sum_{m=0}^{M-1} \sum_{m'=0}^{M-1} H_{n,m}[n,m'] \left[\sum_{k'=0}^{N-1} \sum_{l'=0}^{M-1} x[k',l'] e^{j2\pi\left(\frac{nk'}{N} - \frac{m'l'}{M}\right)} \right] e^{-j2\pi\left(\frac{nk}{N} - \frac{ml}{M}\right)}$$
$$= \frac{1}{NM} \sum_{k'=0}^{N-1} \sum_{l'=0}^{M-1} x[k',l'] \left[\sum_{n=0}^{N-1} \sum_{m=0}^{M-1} \sum_{m'=0}^{M-1} H_{n,m}[n,m'] e^{-j2\pi n\left(\frac{k-k'}{N}\right)} e^{j2\pi\left(\frac{ml-m'l'}{M}\right)} \right]$$
$$= \frac{1}{NM} \sum_{k'=0}^{N-1} \sum_{l'=0}^{M-1} x[k',l'] h_{k,l}^{\text{ici}}[k',l'].$$

(A.15)

$$h_{k,l}^{\text{ici}}[k',l'] = \sum_{n=0}^{N-1} \sum_{m=0}^{M-1} \sum_{m'=0}^{M-1} \left[\int_\tau \int_\nu h(\tau,\nu) A_{g_{\text{rx}},g_{\text{tx}}}(-\tau,(m-m')\Delta f - \nu) e^{-j2\pi(\nu+m'\Delta f)\tau} e^{j2\pi\nu nT} \right.$$
$$\left. d\tau d\nu \right] e^{-j2\pi n\left(\frac{k-k'}{N}\right)} e^{j2\pi\left(\frac{ml-m'l'}{M}\right)}$$

(A.16)

$$= \frac{1}{M} \sum_{n=0}^{N-1} \sum_{m=0}^{M-1} \sum_{m'=0}^{M-1} \left[\sum_{i=1}^{P} h_i \sum_{p=0}^{M-1-l_{\tau_i}} e^{-j2\pi((m-m')\Delta f - \nu_i)(p(T/M)+\tau_i)} e^{-j2\pi(\nu_i+m'\Delta f)\tau_i} e^{j2\pi\nu_i nT} \right]$$
$$e^{-j2\pi n\left(\frac{k-k'}{N}\right)} e^{j2\pi\left(\frac{ml-m'l'}{M}\right)}$$

(A.17)

$$= \sum_{i=1}^{P} h_i \left[\sum_{n=0}^{N-1} e^{-j2\pi n\left(\frac{k-k'-k_{\nu_i}-\kappa_{\nu_i}}{N}\right)} \right] \left[\frac{1}{M} \sum_{p=0}^{M-1-l_{\tau_i}} e^{j2\pi\frac{p}{M}\left(\frac{k_{\nu_i}+\kappa_{\nu_i}}{N}\right)} \sum_{m=0}^{M-1} e^{-j2\pi(p+l_{\tau_i}-l)\frac{m}{M}} \right.$$
$$\left. \sum_{m'=0}^{M-1} e^{j2\pi(p-l')\frac{m'}{M}} \right].$$

$$= \sum_{i=1}^{P} h_i \mathcal{G}^{\text{ici}}(\nu_i) \mathcal{F}^{\text{ici}}(\tau_i,\nu_i).$$

(A.18)

$$\mathcal{F}^{\text{ici}}(\tau_i,\nu_i) = M \sum_{p=0}^{M-1-l_{\tau_i}} e^{j2\pi\frac{p}{M}\left(\frac{k_{\nu_i}+\kappa_{\nu_i}}{N}\right)} \delta([p+l_{\tau_i}-l]_M) \delta([p-l']_M).$$

(A.19)

$$y_{\text{ici}}[k,l] = \frac{1}{N} \sum_{i=1}^{P} h_i \left[\sum_{l'=0}^{M-1} \sum_{p=0}^{M-1-l_{\tau_i}} e^{j2\pi\frac{p}{M}\left(\frac{k_{\nu_i}+\kappa_{\nu_i}}{N}\right)} \delta([p+l_{\tau_i}-l]_M) \delta([p-l']_M) \sum_{k'=0}^{N-1} \mathcal{G}^{\text{ici}}(\nu_i) x[k',l'] \right]$$

$$\approx \frac{1}{N} \sum_{i=1}^{P} h_i \left[\sum_{p=0}^{M-1-l_{\tau_i}} e^{j2\pi \frac{p}{M}\left(\frac{k_{\nu_i}+\kappa_{\nu_i}}{N}\right)} \delta([p+l_{\tau_i}-l]_M) \sum_{q=-N_i}^{N_i} \left(\frac{e^{j2\pi(-q-\kappa_{\nu_i})}-1}{e^{j\frac{2\pi}{N}(-q-\kappa_{\nu_i})}-1} \right) \right.$$

$$\left. x[[k-k_{\nu_i}+q]_N,p] \right]. \quad \text{(A.20)}$$

$$y_{\text{ici}}[k,l] \approx \begin{cases} \sum_{i=1}^{P} \sum_{q=-N_i}^{N_i} h_i \left[\frac{1}{N}\beta_i(q)\right] e^{j2\pi\left(\frac{l-l_{\tau_i}}{M}\right)\left(\frac{k_{\nu_i}+\kappa_{\nu_i}}{N}\right)} x\left[[k-k_{\nu_i}+q]_N,[l-l_{\tau_i}]_M\right] & l \geq l_{\tau_i}, \\[2mm] 0 & \text{otherwise.} \end{cases}$$

$$\text{(A.21)}$$

$$y_{\text{isi}}[k,l] = \frac{1}{NM} \sum_{n=0}^{N-1} \sum_{m=0}^{M-1} \sum_{m'=0}^{M-1} H_{n,m}[n-1,m'] \left[\sum_{k'=0}^{N-1} \sum_{l'=0}^{M-1} x[k',l'] e^{j2\pi\left(\frac{(n-1)k'}{N}-\frac{m'l'}{M}\right)} \right] e^{-j2\pi\left(\frac{nk}{N}-\frac{ml}{M}\right)}$$

$$= \frac{1}{NM} \sum_{k'=0}^{N-1} \sum_{l'=0}^{M-1} e^{-j2\pi\frac{k'}{N}} x[k',l'] \left[\sum_{n=0}^{N-1} \sum_{m=0}^{M-1} \sum_{m'=0}^{M-1} H_{n,m}[n-1,m'] e^{-j2\pi n\left(\frac{k-k'}{N}\right)} e^{j2\pi\left(\frac{ml-m'l'}{M}\right)} \right]$$

$$= \frac{1}{NM} \sum_{k'=0}^{N-1} \sum_{l'=0}^{M-1} e^{-j2\pi\frac{k'}{N}} x[k',l'] h^{\text{isi}}_{k,l}[k',l']. \quad \text{(A.22)}$$

$$h^{\text{isi}}_{k,l}[k',l'] = \sum_{i=1}^{P} h_i \left[\sum_{n=1}^{N-1} e^{-j2\pi n\left(\frac{k-k'-k_{\nu_i}-\kappa_{\nu_i}}{N}\right)} \right] \left[\frac{1}{M} \sum_{p=M-l_{\tau_i}}^{M-1} e^{j2\pi\left(\frac{p-M}{M}\right)\left(\frac{k_{\nu_i}+\kappa_{\nu_i}}{N}\right)} \right.$$

$$\left. \sum_{m=0}^{M-1} e^{-j2\pi(p+l_{\tau_i}-l+M)\frac{m}{M}} \sum_{m'=0}^{M-1} e^{j2\pi(p-l')\frac{m'}{M}} \right]$$

$$= \sum_{i=1}^{P} h_i \mathcal{G}^{\text{isi}}(\nu_i) \mathcal{F}^{\text{isi}}(\tau_i,\nu_i). \quad \text{(A.23)}$$

$$y_{\text{isi}}[k,l] = \frac{1}{N} \sum_{i=1}^{P} h_i \left[\sum_{l'=0}^{M-1} \sum_{p=M-l_{\tau_i}}^{M-1} e^{j2\pi\left(\frac{p-M}{M}\right)\left(\frac{k_{\nu_i}+\kappa_{\nu_i}}{N}\right)} \delta([p+l_{\tau_i}-l]_M)\delta([p-l']_M) \cdot \right.$$

$$\left. \sum_{k'=0}^{N-1} \mathcal{G}^{\text{isi}}(\nu_i) e^{-j2\pi\frac{k'}{N}} x[k',l'] \right] \quad \text{(A.24)}$$

$$= \frac{1}{N} \sum_{i=1}^{P} h_i \left[\sum_{p=M-l_{\tau_i}}^{M-1} e^{j2\pi\left(\frac{p-M}{M}\right)\left(\frac{k_{\nu_i}+\kappa_{\nu_i}}{N}\right)} \delta([p+l_{\tau_i}-l]_M) \sum_{k'=0}^{N-1} \mathcal{G}^{\text{isi}}(\nu_i) e^{-j2\pi\frac{k'}{N}} x[k',p] \right]$$

$$\approx \frac{1}{N} \sum_{i=1}^{P} h_i \left[\sum_{p=M-l_{\tau_i}}^{M-1} e^{j2\pi\left(\frac{p-M}{M}\right)\left(\frac{k\nu_i+\kappa\nu_i}{N}\right)} \delta([p+l_{\tau_i}-l]_M) \right.$$

$$\left\{ \sum_{q=-N_i}^{N_i} (\beta_i(q)-1) e^{-j2\pi\frac{[k-k_{\nu_i}+q]_N}{N}} x[[k-k_{\nu_i}+q]_N,p] - \sum_{\substack{k'=0, \\ k'\neq[k-k_{\nu_i}+q]_N, q\in[-N_i,N_i]}}^{N-1} e^{-j2\pi\frac{k'}{N}} x[k',p] \right\} \right] \quad (A.25)$$

$$\approx \frac{1}{N} \sum_{i=1}^{P} h_i \left[\sum_{p=M-l_{\tau_i}}^{M-1} e^{j2\pi\left(\frac{p-M}{M}\right)\left(\frac{k\nu_i+\kappa\nu_i}{N}\right)} \delta([p+l_{\tau_i}-l]_M) \sum_{q=-N_i}^{N_i} (\beta_i(q)-1) e^{-j2\pi\frac{[k-k_{\nu_i}+q]_N}{N}} \right.$$

$$\left. x[[k-k_{\nu_i}+q]_N,p] \right]. \quad (A.26)$$

$$y_{\text{isi}}[k,l] \approx \begin{cases} \sum_{i=1}^{P} \sum_{q=-N_i}^{N_i} h_i \left[\frac{1}{N}(\beta_i(q)-1)\right] e^{-j2\pi\frac{[k-k_{\nu_i}+q]_N}{N}} e^{j2\pi\left(\frac{l-l_{\tau_i}}{M}\right)\left(\frac{k\nu_i+\kappa\nu_i}{N}\right)} \\ \qquad\qquad\qquad x[[k-k_{\nu_i}+q]_N, [l-l_{\tau_i}]_M] \quad l < l_{\tau_i}, \\ \\ 0 \qquad\qquad\qquad\qquad\qquad\qquad\qquad\qquad\qquad \text{otherwise.} \end{cases} \quad (A.27)$$

A.2   Proof of Proposition 2.2:   OTFS Input–Output Relation in Delay–Doppler Domain for Ideal Pulses

The received signal $y[k,l]$ for the ideal pulses, from (2.11) and (2.13), can be written as

$$y[k,l] = \frac{1}{\sqrt{NM}} \sum_{n=0}^{N-1} \sum_{m=0}^{M-1} H_{n,m}[n,m] X[n,m] e^{-j2\pi\left(\frac{nk}{N}-\frac{ml}{M}\right)}.$$

By substituting the ISFFT equation from (2.2), $y[k,l]$ can be expanded as in from (A.8) to (A.10). Here, $h_w[k-k',l-l']$ can be seen as the value of $h_w(\nu,\tau)$ sampled at $\nu = \frac{k-k'}{NT}, \tau = \frac{l-l'}{M\Delta f}$. The value of $h_w(\nu,\tau)$ can be obtained as from (A.11) to (A.13), by substituting $H_{n,m}[n,m]$ from (2.10), which completes the proof.

A.3 Proof of Theorem 2.2: OTFS Input–Output Relation in Delay–Doppler Domain for Rectangular Pulses

We start with expanding $y[k, l]$ in (2.11) using the $Y[n, m]$ for rectangular pulses in (2.21) as in (A.14). We write $y[k, l]$ as

$$y[k, l] = y_{\text{ici}}[k, l] + y_{\text{isi}}[k, l],$$

where $y_{\text{ici}}[k, l]$ and $y_{\text{isi}}[k, l]$ contains the first term and the second term of the summation in square brackets of (A.14), respectively. We analyze these ICI and ISI terms as below.

Analysis of $y_{\text{ici}}[k, l]$: The value of $y_{\text{ici}}[k, l]$ can be written as in (A.15) using the ISFFT of $X[n, m]$ given in (2.2). Now, $h_{k,l}^{\text{ici}}[k', l']$ is expanded in (A.16) by using the $H_{n,m}[n, m']$ value in (2.10). This can be further written as in (A.17) from the channel assumption in (2.5) and the cross-ambiguity function in (2.22).

To write the expression in (A.17) to a simple form, let us separate the terms related to n, m, m', and p. The terms related to n are

$$\zeta_n = e^{-j2\pi n\left(\frac{k-k'}{N}\right)} e^{j2\pi \nu_i nT}$$
$$= e^{-j2\pi n\left(\frac{k-k'-k_{\nu_i}-\kappa_{\nu_i}}{N}\right)}.$$

Here, we used the delay and Doppler taps defined in (2.6). Similarly, the terms related to m and m' are

$$\zeta_m = e^{-j2\pi m\Delta f(p(T/M)+\tau_i)} e^{j2\pi l \frac{m}{M}} = e^{-j2\pi(p+l_{\tau_i}-l)\frac{m}{M}}.$$
$$\zeta_{m'} = e^{j2\pi m'\Delta f(p(T/M)+\tau_i)} e^{-j2\pi m'\Delta f\tau_i} e^{-j2\pi l'\frac{m'}{M}} = e^{j2\pi(p-l')\frac{m'}{M}}.$$

Finally, the terms related to p are

$$\zeta_p = e^{j2\pi \nu_i(p(T/M)+\tau_i)} e^{-j2\pi \nu_i \tau_i} = e^{j2\pi \frac{p}{M}\left(\frac{k_{\nu_i}+\kappa_{\nu_i}}{N}\right)}.$$

Therefore, from the above terms, the value of $h_{k,l}^{\text{ici}}[k', l']$ can be written as in (A.18), where $\mathcal{G}^{\text{ici}}(\nu_i)$

and $\mathcal{F}^{\mathrm{ici}}(\tau_i, \nu_i)$ denote the terms in the first and second square brackets. The value of $\mathcal{G}^{\mathrm{ici}}(\nu_i)$ is the same as the one studied in (2.18) for ideal pulses case. Similar to the analysis of (2.17), $\mathcal{F}^{\mathrm{ici}}(\tau_i, \nu_i)$ can be written as in (A.19). Hence, by substituting (A.18) and (A.19) in (A.16), $y_{\mathrm{ici}}[k, l]$ can be approximated as in (A.20). From (A.20), we can easily see that it is non-zero only if the following conditions satisfied

$$p = [l - l_{\tau_i}]_M \text{ and } 0 \le p \le M - 1 - l_{\tau_i}.$$

These conditions are satisfied only if $l \ge l_{\tau_i}$ and $p = l - l_{\tau_i}$. Finally, with the conditions on l and p, $y_{\mathrm{ici}}[k, l]$ can be obtained as in (A.21), where $\beta_i(q)$ is defined in (2.25).

Analysis of $y_{\mathrm{isi}}[k, l]$: Similar to $y_{\mathrm{ici}}[k, l]$ in (A.15), $y_{\mathrm{isi}}[k, l]$ can be expanded as in (A.22). By substituting the value of $H_{n,m}[n-1, m']$ from (2.10), cross-ambiguity function in (2.23), and similar analysis of separating terms for $h_{k,l}^{\mathrm{ici}}[k', l']$, the value of $h_{k,l}^{\mathrm{isi}}[k', l']$ can be obtained as in (A.23). Here, the summation n starts from 1 as the first symbol does not have previous symbol to experience ISI. Therefore, the value of $\mathcal{G}^{\mathrm{isi}}(\nu_i)$ is equal to $\mathcal{G}^{\mathrm{ici}}(\nu_i) - 1$. Using the value of $\mathcal{G}^{\mathrm{isi}}(\nu_i)$, $y_{\mathrm{isi}}[k, l]$ can be approximated as in (A.25). Further, the expression in (A.25) can be approximated as in (A.26) by neglecting the signals $x[k', p]$ for which $k' \ne [k - k_{\nu_i} + q]_N, q \in [-N_i, N_i]$, as their coefficients are very small $(1/N)$ for practical values of N (e.g., $N = 64, 128$).

Now, (A.26) is non-zero only if the following conditions are satisfied

$$p = [l - l_{\tau_i}]_M \text{ and } M - l_{\tau_i} \le p \le M - 1.$$

These conditions are satisfied only if $l < l_{\tau_i}$ and $p = l - l_{\tau_i} + M$. With these conditions, the value of $y_{\mathrm{isi}}[k, l]$ is written in (A.27).

Finally, by combining (A.21) and (A.27), the value of $y[k, l]$ in (A.14) can be obtained as in (2.24), which completes the proof.

Appendix B

Proofs for Chapter 3

B.1 Proof of Theorem 3.1

From (3.11), since $(\mathbf{F}_N \otimes \mathbf{I}_M)$ is a unitary matrix, the effective channel matrix can be written as

$$
\mathbf{H}_{\text{eff}}^{\text{rect}} = \sum_{i=1}^{P} h_i \underbrace{\left[(\mathbf{F}_N \otimes \mathbf{I}_M) \mathbf{\Pi}^{l_i} (\mathbf{F}_N^{\text{H}} \otimes \mathbf{I}_M) \right]}_{\mathbf{P}^{(i)}} \cdot
$$

$$
\underbrace{\left[(\mathbf{F}_N \otimes \mathbf{I}_M) \mathbf{\Delta}^{k_i} (\mathbf{F}_N^{\text{H}} \otimes \mathbf{I}_M) \right]}_{\mathbf{Q}^{(i)}} = \sum_{i=1}^{P} h_i \mathbf{P}^{(i)} \mathbf{Q}^{(i)} \tag{B.1}
$$

(a) Evaluation of $\mathbf{P}^{(i)}$ *–* Since $\mathbf{\Pi}$ is a permutation matrix, $\mathbf{\Pi}^{l_i}$ is also a permutation matrix with 1s in $(p, [p - l_i]_{MN})^{th}$ entries, for $0 \le p \le MN - 1$, and zeros elsewhere. Further, $\mathbf{\Pi}^{l_i}$ is a circulant matrix which can also be seen as block-circulant with the form (3.13), in which $\mathbf{A}_n = \mathbf{\Pi}_n^{l_i}$ for $n = 0, \ldots, N - 1$. Therefore, application of Lemma 3.1 shows that $\mathbf{P}^{(i)}$ has the block-diagonal form (3.16), with $N \times N$ diagonal blocks denoted by $\mathbf{P}_0^{(i)}, \ldots, \mathbf{P}_{N-1}^{(i)}$.

Since $l_i < M$, $\mathbf{\Pi}_2^{l_i}, \cdots, \mathbf{\Pi}_{N-1}^{l_i}$ are all-zero matrices ($\mathbf{0}$), and $\mathbf{\Pi}_0^{l_i}$ and $\mathbf{\Pi}_1^{l_i}$ has 1s in rows from l_i to $M - 1$ and 0 to $l_i - 1$, respectively and all zeros in the remaining rows. Therefore, applying (3.17) in Lemma 3.1, and considering that the vector $\mathbf{a}(u, v)$ has only one nonzero element (which

equals to 1), we obtain

$$
\mathbf{P}_n^{(i)}(u,v) = \begin{cases} 1 & \text{if } u \geq l_i \text{ and } v = u - l_i \\ e^{-j2\pi\frac{n}{N}} & \text{if } u < l_i \text{ and } v = [u - l_i]_M \\ 0 & \text{otherwise} \end{cases}
\tag{B.2}
$$

for $0 \leq n \leq N - 1$ and $0 \leq u, v \leq N - 1$. Here, we obtain the values 1 and $e^{-j2\pi\frac{n}{N}}$ by applying the DFT to vectors $\mathbf{a} = [1, 0, \cdots, 0]^T$ and its cyclic shifts by n, respectively.

Finally, the $(p, q)^{th}$ entry of $\mathbf{P}^{(i)}$ for $0 \leq p, q \leq MN - 1$ is

$$
\mathbf{P}^{(i)}(p,q) = \begin{cases} 1 & \text{if } m \geq l_i, q = [m - l_i]_M + nM \\ e^{-j2\pi\frac{n}{N}} & \text{if } m < l_i, q = [m - l_i]_M + nM \\ 0 & \text{otherwise} \end{cases}
\tag{B.3}
$$

where, $n = \lfloor \frac{p}{M} \rfloor$ and $m = p - nM$. The values in (B.3) are obtained from (B.2) with the substitutions $p = nM + u, q = nM + v$ and $u = m$.

(b) Evaluation of $\mathbf{Q}^{(i)}$ – Observing that the diagonal matrix $\mathbf{\Delta}^{k_i}$ can be viewed as a block-diagonal matrix, and using (3.15), we can easily see that $\mathbf{Q}^{(i)}$ is a block-circulant matrix of the form (3.13).

Since the $M \times M$ blocks $\mathbf{\Delta}_0^{k_i}, \cdots, \mathbf{\Delta}_{N-1}^{k_i}$ are diagonal, from (3.18) we have

$$
\mathbf{Q}_n^{(i)}(u,v) = 0, \text{ for } u \neq v, \ 0 \leq n \leq N - 1
\tag{B.4}
$$

and the diagonal entries of $\mathbf{Q}_0^{(i)}, \cdots, \mathbf{Q}_{N-1}^{(i)}$ are related to the elements of $\mathbf{\Delta}^{(i)}$ as

$$
\begin{aligned}
&\left[\mathbf{Q}_0^{(i)}(u,u), \cdots, \mathbf{Q}_{N-1}^{(i)}(u,u) \right]^T \\
&= \left(\frac{1}{\sqrt{N}} \right) \mathbf{F}_N \left[\mathbf{\Delta}_0^{k_i}(u,u), \cdots, \mathbf{\Delta}_{N-1}^{k_i}(u,u) \right]^T \\
&= \left(\frac{1}{\sqrt{N}} \right) \mathbf{F}_N \left[z^{k_i u}, \cdots, z^{k_i(M(N-1)+u)} \right]^T \\
&= z^{k_i u} [0, \cdots, \underbrace{1}_{(k_i+1)^{th} \text{ entry}}, 0, \cdots, 0]^T
\end{aligned}
\tag{B.5}
$$

Therefore, we can write $\mathbf{Q}_n^{(i)}$ as

$$
\mathbf{Q}_n^{(i)}(u,v) = \begin{cases} z^{k_i u} & \text{if } n = k_i \text{ and } u = v \\ \\ 0 & \text{otherwise} \end{cases} \tag{B.6}
$$

for $0 \le n \le N-1$ and $0 \le u,v \le N-1$. Further, the $(p,q)^{th}$ entry of $\mathbf{Q}^{(i)}$, for $0 \le p,q \le MN-1$, is equal to

$$
\mathbf{Q}^{(i)}(p,q) = \begin{cases} z^{k_i m'} & \text{if } p = m' + M[n' + k_i]_N \\ \\ 0 & \text{otherwise} \end{cases} \tag{B.7}
$$

where, $n' = \lfloor \frac{q}{M} \rfloor$ and $m' = q - n'M$.

Now, the $(p,q)^{th}$ entry of $\mathbf{T}^{(i)} = \mathbf{P}^{(i)}\mathbf{Q}^{(i)}$, for $0 \le p,q \le MN-1$, can be written as

$$
\mathbf{T}^{(i)}(p,q) = \sum_{e=0}^{MN-1} \mathbf{P}^{(i)}(p,e)\mathbf{Q}^{(i)}(e,q) \tag{B.8}
$$

From (B.3), (B.7), and (B.8), we can see that $\mathbf{T}^{(i)}(p,q)$ has nonzero value only for

$$
[m - l_i]_M + nM = m' + M[n' + k_i]_N, \tag{B.9}
$$

which implies $m' = [m - l_i]_M$ and $n' = [n - k_i]_N$, or $q = [m - l_i]_M + M[n - k_i]_N$. Moreover, the value at $\mathbf{T}^{(i)}(p,q)$ depends on m and it is equal to $e^{-j2\pi n/N} z^{k_i([m-l_i]_M)}$ and $z^{k_i([m-l_i]_M)}$ for $m < l_i$ and $m \ge l_i$, respectively.

Finally, from (B.1) and (3.20), we see that there exists only one nonzero element in each row of $\mathbf{T}^{(i)}$. Further, based on the assumption that in different paths at least one of the k_i or l_i is also different, exactly P nonzero elements exist in each row and column of $\mathbf{H}_{\text{eff}}^{\text{rect}}$.

Appendix C

Proofs for Chapter 5

C.1 Proof of Theorem 5.1

(If) – For $M \geq L$, the entries of the vectors $\mathbf{u}_{(i,j)}$, $0 \leq i,j \leq M-1$, become

$$
\mathbf{u}_{(i,j)} = \begin{cases} [h_{i-j}, 0, \cdots, 0] & \text{if } 0 \leq (i-j) \leq (L-1) \\ [0, h_{L+(i-j)}, \cdots, 0] & \text{if } -(L-1) \leq (i-j) < 0 \\ [0, \; 0, \; \cdots, 0] & \text{otherwise} \end{cases}
$$

Taking the FFT's of the above we have

$$
\mathbf{v}_{(i,j)} = \begin{cases} [h_{i-j}, h_{i-j}, \cdots, h_{i-j}] & \text{if } 0 \leq (i-j) \leq (L-1) \\ h_{L+(i-j)} \cdot [e^{-j2\pi \frac{0}{N}}, e^{-j2\pi \frac{1}{N}}, \cdots, e^{-j2\pi \frac{N-1}{N}}] & \\ & \text{if } -(L-1) \leq (i-j) < 0 \\ [0, 0, \cdots, 0] & \text{otherwise} \end{cases} \tag{C.1}
$$

According to Lemma 5.1 and (C.1), we obtain

$$
\breve{\mathbf{H}}_n =
\begin{bmatrix}
h_0 & 0 & \cdots & h_1 e^{-j2\pi\frac{n}{N}} \\
h_1 & h_0 & \cdots & h_2 e^{-j2\pi\frac{n}{N}} \\
\vdots & \ddots & \ddots & \vdots \\
0 & \cdots & h_1 & h_0
\end{bmatrix}
\tag{C.2}
$$

Hence, from (5.8) and (C.2), we can conclude that OTFS input-output relation is equivalent to N parallel CPSCs of length M over identical channels, except for an additional phase shift $e^{-j2\pi\frac{n}{N}}$. Moreover, there are only P non-zero entries in each row and column of $\breve{\mathbf{H}}_n$.

(Only if) – For $M < L$, we can easily see that $\mathbf{u}_{(i,j)}$ has at least two non-zero entries for some $0 \leq i,j \leq M-1$. For example, for $M = 2$, the value of $\breve{\mathbf{H}}_n$ becomes

$$
\breve{\mathbf{H}}_n =
\begin{bmatrix}
\mathbf{v}_{(0,0)}(n) & \mathbf{v}_{(1,0)}(n)e^{-j2\pi\frac{n}{N}} \\
\mathbf{v}_{(1,0)}(n) & \mathbf{v}_{(0,0)}(n)
\end{bmatrix}
$$

where, $\mathbf{v}_{(0,0)}$ and $\mathbf{v}_{(1,0)}$ are the FFT's of $\mathbf{u}_{(0,0)} = [h_0, h_2, \cdots, 0]$ and $\mathbf{u}_{(1,0)} = [h_1, h_3, \cdots, 0]$, respectively.

Therefore, due to FFT operation, the entries of $\breve{\mathbf{H}}_n$ differ in both amplitude and phase for each n, and lower gain channels effect the overall system performance (similar to OFDM).

Appendix D

Proofs for Chapter 6

D.1 Proof of Lemma 6.1

The spectral norm of $\mathbf{A}^H$ is defined as $\|\mathbf{A}^H\|_2 = \max_{\|\mathbf{x}\|=1} \|\mathbf{A}^H \mathbf{x}\| = \lambda_{max}$, where λ_{max} is the largest singular value of $\mathbf{A}^H$. Since $\mathbf{F}_N = \mathbf{P}\mathbf{A}^H$ and $\mathbf{P}^{-1} = \mathbf{P}^H$, we have, $\mathbf{A}\mathbf{A}^H = \mathbf{F}_N^H (\mathbf{P}^{-1})^H \mathbf{P}^{-1} \mathbf{F}_N = \mathbf{F}_N^H \mathbf{F}_N = R\, \mathbf{I}_N$ and $\lambda_{max} = \sqrt{R}$. Let us consider the value of $\|\mathbf{g}(\ell, i)\| = \|\mathbf{A}^H \mathbf{w}(\ell, i)\| = c_\ell \sqrt{R/K^\ell}$. Therefore, according to the spectral norm definition, $c_\ell \sqrt{R/K^\ell} \leq \sqrt{N}\lambda_{max} = \sqrt{NR}$. Hence we obtain $c_\ell \leq \sqrt{NK^\ell}$.

D.2 Proof of Proposition 6.1

Let $\mathbf{f}(\ell, i) = \mathbf{A}^H \mathbf{w}(\ell, i)$ represent the gain pattern of the ith beamforming vector at the ℓth level for $1 \leq i \leq K^\ell$. The vector $\mathbf{f}(\ell, p)$, for $2 \leq p \leq K^\ell$, is simply the right circular shifted version of $\mathbf{f}(\ell, 1)$ with a shift of $\frac{R(p-1)}{K^\ell}$. That is, for $2 \leq p \leq K^\ell$,

$$f_n(\ell, 1) = \begin{cases} f_{n+\frac{R(p-1)}{K^\ell}}(\ell, p) & \text{if } 1 \leq n \leq R - \frac{R(p-1)}{K^\ell} \\ f_{n+\frac{R(p-1)}{K^\ell}-R}(\ell, p) & \text{if } R - \frac{R(p-1)}{K^\ell} + 1 \leq n \leq R \end{cases} \tag{D.1}$$

where $f_n(\ell, i)$, for $1 \leq n \leq R$, denotes the nth element in the vector $\mathbf{f}(\ell, i)$.

For $1 \leq n \leq R - \frac{R(j-1)}{K^\ell}$, $2 \leq p \leq K^\ell$, we have

$$f_{n+\frac{R(p-1)}{K^\ell}}(\ell,p) = \sum_{r=0}^{N-1} e^{-jr\pi(-1+\frac{2n}{R})} e^{-jr2\pi\left(\frac{p-1}{K^\ell}\right)} w_s(\ell,p). \tag{D.2}$$

Similarly, for $R - \frac{R(p-1)}{K^\ell} + 1 \le n \le R$, $2 \le p \le K^\ell$, we have

$$f_{n+\frac{R(p-1)}{K^\ell}-R}(\ell,p) = \sum_{r=0}^{N-1} e^{-jr\pi(-1+\frac{2n}{R})} e^{jr2\pi} e^{-jr2\pi\left(\frac{p-1}{K^\ell}\right)} w_s(\ell,p).$$

Finally, we obtain $f_n(\ell,1) = \sum_{r=0}^{N-1} e^{-jr\pi(-1+\frac{2n}{R})} w_s(\ell,1)$. Therefore, the condition in (D.1) is satisfied for

$$w_s(\ell,p) = w_s(\ell,1) e^{jr2\pi\left(\frac{p-1}{K^\ell}\right)}. \tag{D.3}$$

Assuming $\mathbf{w}(\ell,1) \in \mathcal{S}_q(N)$, then the beamforming vector $\mathbf{w}(\ell,p)$ found from the above equation will be in $\mathcal{S}_q(N)$ if the phase shift $r\left(\frac{p-1}{K^\ell}\right)$ falls in the allowed q uniformly spaced angles in $[0, 2\pi)$. This condition is satisfied if K^ℓ divides q as r and p are integers.